NATIONAL AERONAUTICS AND SPACE ADMINISTRATION

Technical Report 32-1347

Power System Design for a Jupiter Solar Electric Propulsion Spacecraft

V. Truscello
Jet Propulsion Laboratory
R. E. Loucks
TRW Systems

JET PROPULSION LABORATORY
CALIFORNIA INSTITUTE OF TECHNOLOGY
PASADENA, CALIFORNIA

October 15, 1968

NATIONAL AERONAUTICS AND SPACE ADMINISTRATION

Technical Report 32-1347

Power System Design for a Jupiter Solar Electric Propulsion Spacecraft

V. Truscello
Jet Propulsion Laboratory
R. E. Loucks
TRW Systems

Approved by:

L. D Runkle

for P. Goldsmith, *Manager*
Spacecraft Power Section

JET PROPULSION LABORATORY
CALIFORNIA INSTITUTE OF TECHNOLOGY
PASADENA, CALIFORNIA

October 15, 1968

TECHNICAL REPORT 32-1347

Prepared Under Contract No. NAS 7-100
National Aeronautics & Space Administration

Foreword

This report was prepared using material compiled for a Jupiter Solar Electric Mission Study directed by the JPL Future Projects Office. The purpose of this report is to document the design of a photovoltaic electrical power system that will meet the requirements of a solar electric spacecraft mission to Jupiter.

Acknowledgment

The authors wish to acknowledge the valuable contributions of the following JPL personnel: R. A. Booth, R. J. Mankovitz, P. D. Reader, D. W. Ritchie, and B. K. Wada.

Contents

Contents (contd)

Tables

Contents (contd)

Figures

Contents (contd)

Figures (contd)

Abstract

The design of an electrical power system for a solar electric spacecraft mission to Jupiter is described. The design concept includes a large-area photovoltaic solar array for primary electrical power, a "hibernating" AgZn battery subsystem for energy storage, and power conditioning equipment for conversion and distribution of power to spacecraft loads.

The concept combines a programmed ion engine power consumption profile with a solar panel maximum power point tracker for ion engine control and load matching. This combination minimizes the problem of predicting the solar-panel output power available for ion engine consumption as a function of mission time. In addition, the study includes an evaluation of the effects of proton, electron, and micrometeoroid damage on the performance of the solar array.

Power System Design for a Jupiter Solar Electric Propulsion Spacecraft

I. Introduction

New developments in both electric propulsion technology and large-area lightweight solar arrays make a solar-powered ion-propelled spacecraft mission to Jupiter appear attractive. A study ("Jupiter Solar Electric Mission Study") was undertaken by the Jet Propulsion Laboratory under the direction of the Future Projects Office. The primary objective of the study was to define a solar-electric-powered ion-propelled spacecraft system capable of delivering Mariner-class payloads to the planet in 1975. The payload, defined in Tables 1 and 2, is capable of yielding significant scientific information about Jupiter and the interplanetary space near the planet.

The mission would be performed using an *Atlas/SLV-3C/Centaur* launch vehicle, which has a net injected payload capability of 2398 lb at a geocentric injection energy (C_3) of 1.30. The total injected weight of the proposed spacecraft system is 2362 lb. The mission would follow a direct trajectory to Jupiter with a trip time of approximately 900 days. Low-thrust propulsion is provided by ion engines during the first 470 days of the mission. After this powered flight phase, the spacecraft continues to the target planet on a ballistic trajectory. The trajectory would take the spacecraft within 160,000 km of the surface of Jupiter.

A distinct advantage of a solar electric spacecraft mission over an all-chemical system is the lower cost associated with using the spacecraft itself combined with a small chemical booster. Reference 1 presents a preliminary review of the payload capabilities and advantages of solar electric spacecraft for several classes of unmanned interplanetary probe and orbiter missions. The general conclusions of Ref. 1 are that, for a given booster system, the advantages of solar electric propulsion grow with increasing mission difficulty and, for many missions and booster combinations, the solar electric spacecraft can do a mission that cannot be done by the booster alone. In other cases, the solar electric spacecraft can reduce trip time or provide a power supply at the target or do both functions.

To arrive at a realistic spacecraft weight, it was necessary to give more resolute consideration to details in the design of each spacecraft engineering and science subsystem. The major considerations in the design of the power system are as follows:

(1) The development of a power source (solar array) having a high specific power, i.e., in excess of 20 W/lb.

(2) The storage and deployment of a large photovoltaic power source.

Table 1. System design parameters for preliminary Jupiter solar electric spacecraft (direct trajectory)

Assembly and subassembly	Currently estimated weight, lb	Weight summary, lb	Mass fraction, %
Propulsion subsystem		180	7.6
Thrusters (5)	55		
Gimbals and actuators	10		
Translator	15		
Power conditioners (11.1 kW at 9 lb/kW)	100		
Solar panel subsystem (14 kW at 20.7 W/lb)		676	28.6
Solar panels (1476 ft^2 at 9.5 W/ft^2) (foldup array)	676		
Propellant subsystem		870	36.9
Propellant	845		
Propellant tanks and hardware (3% propellant mass)	25		
Payload		636	26.9
Science subsystem	79		
Cruise science	30		
Encounter science (TV, IR spectrometer)	38		
Scan platform	8		
Planet sensors	3		
Engineering subsystems	557		
Telecommunications	133		
Guidance and control	145		
Spacecraft power subsystem (housekeeping)	80		
Structure assembly	121		
Thermal control subsystem	26		
Electrical cabling subsystem	35		
Pyrotechnic subsystem	13		
Independently mounted actuators	4		
Total injected weight required		2362	100.0
Net injected payload capability at $C_3 = 1.30$		2398	
Contingency		36	

(3) The uncertainty in the performance of the power source due to interplanetary and planetary environmental effects.

(4) The large output voltage variation (with time) of the solar array due to the mission temperature profile.

(5) The design of power conditioning equipment that can accommodate the large variation in input voltage.

(6) Load matching of ion engine demands to the power source capabilities when the power output of the source varies with time.

(7) Providing the necessary electrical power during solar occultation at Jupiter encounter.

The design concept presented attempts to solve or minimize the listed problems. The concept employs four lightweight foldup solar panels with a total combined array area of 1476 ft^2. The estimated output power of the array in earth space is 14 kW. In addition, the design includes a power conditioning subsystem for the propulsion subsystem, an auxiliary electrical power subsystem

Table 2. Design characteristics

Item	Characteristic
Launch vehicle	*Atlas/SLV-3C/Centaur*
Solar panel	
Degradation factors[a]	18%
Equilibrium temperature	61°C, 1 AU; −158°C, 5 AU
Voltage swing	40V, 1 AU; 84V, 5 AU
Power conditioning efficiency (thrusters)	93%
Spacecraft power requirements	250 W

[a]Solar flares and environmental uncertainties.

for the engineering and science loads, a programmed ion engine power consumption profile, and a maximum power point tracker and load-matching subsystem.

II. Functional Description of Baseline Power System

The first part of this section provides an overall functional description of the baseline configuration. It identifies the components comprising the system and outlines their overall characteristics. This description is followed by a mission-oriented section that identifies the major power management problems and operation of the power system during various portions of the mission.

A. Power System Description and Characteristics

The power system, shown in Fig. 1, is composed of four major subsystems. These subsystems and their functions are as follows:

(1) The photovoltaic power source subsystem converts solar energy into the necessary electrical power.

(2) The propulsion power conditioning subsystem converts the low-voltage, high-current dc output of the solar panels to the appropriate voltage and current levels required by the various propulsion subsystems.

(3) The auxiliary electrical power subsystem provides all the necessary housekeeping power. This includes power for guidance and thermal control, telecommunications, scientific instruments and the load-matching control electronics. The subsystem is composed of a battery package and associated battery charger, power conditioning equipment, and power source logic (PSL) circuit. The PSL receives the raw bus power from the solar panels and distributes this power to both the propulsion power conditioning subsystem and the spacecraft electrical subsystem. It controls the distribution of the on-board battery power to the spacecraft electrical power conditioning equipment prior to solar acquisition, and controls power from the block house for spacecraft electrical checkout prior to launch.

(4) Engine control set-point determination and load-matching subsystem supplies an input signal

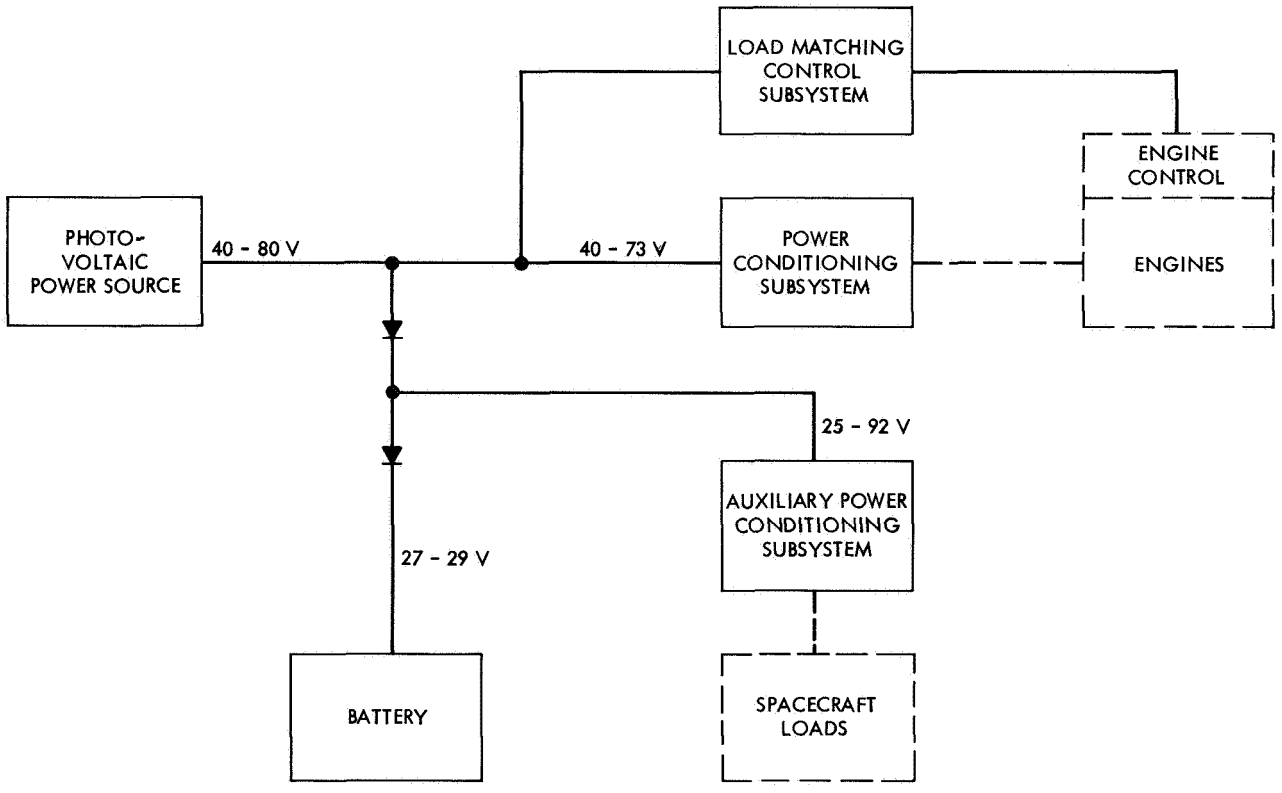

Fig. 1. Power system block diagram

(0–5V) to the engine control unit. This unit, in turn, adjusts the operating parameters of the ion engines in proportion to the magnitude of the signal such that the power demands of the engines correspond to either a programmed power consumption profile or the maximum capacity of the panel, whichever is lowest.

The photovoltaic power source consists of four panels that have been sized to produce a nominal 14 kWe at 1 AU with a 40-V output. Table 3 presents a summary of the power allocations. The propulsion subsystem power conditioner (PC) requires 11.1 kWe of unregulated power. The spacecraft power subsystem was allocated 0.4 kW, although later analysis showed that this was conservative and could be reduced to 0.3 kW. An 18% contingency factor (2.5 kW) has been allowed for panel degradation due to solar flares and for uncertainties associated with predicting the actual power plant nominal capability (see Section III-A-2 for details). Weight and volume allocations for the various power subsystems are given in Table 4.

B. Mission Description and Power System Function

1. Launch and acquisition phases. During the early portion of the mission, from launch until completion of sun acquisition, the spacecraft is powered by batteries. In this early phase of the mission, spacecraft power requirements are fairly constant, averaging about 180 W. A detailed load profile is given in Table 5. Assuming 75% power conversion efficiency, it is found that a total of 370 Wh (under worst case conditions) is required from the battery system.

A 600-Wh silver-zinc battery has been selected to meet this requirement. Under the failure mode condition (i.e., when both sun acquisition and separation reduction require twice the nominal time to perform), the battery

Table 3. Total power system requirements

Requirement	Power, kWe
Unregulated power to propulsion subsystem power conditioner (at 1 AU)	11.1
Unregulated power to spacecraft power subsystem (continuous)	0.4
Power plant contingency factor (18%) (at 1 AU)	2.5
Total	14.0

Table 4. Weight and volume of the power subsystems

Subsystem	Weight, lb	Volume, ft^3
Photo voltaic power source	676	273 (stowed condition)[a]
Propulsion power conditioning	100	7
Auxiliary electrical power	78.5	1.3
Engine control set point determination and load matching	1.5	0.02

[a]Deployed condition has an area of 1476 ft^2.

Table 5. Spacecraft load demands during launch and sun acquisition phases

Electrical loads	Flight Phase							
	Launch		Solar panel deployment		Separation rate reduction		Sun acquisition	
	Power, W	Time, min	Power, W	Time, min	Power, W	Time,[a] min	Power, W	Time,[a] min
Telecommunications	103	20	103	20	103	1	103	60
CC&S	16	20	16	20	16	1	16	60
Gyros	21	20	21	20	21	1	21	60
Cold gas attitude control	—	—	15	20	15	1	15	60
Deployment motors	—	—	60	20	—	—	—	—
Cold gas jet firings	—	—	—	—	40	1	30	1-1/3
Total power, W	140		215		195		185	
Total energy, Wh	47		72		3		156	

[a]Values given are for a failure mode (i.e., only ½ gas jet capacity); nominal time requirements are ½ those shown.

depth of discharge is 62%. Under normal conditions, it will be only 45%. The battery will supply this power at a load voltage between 27 and 29 V.

As noted previously, prior to initiation of solar acquisition, power is obtained solely from batteries. However, as the spacecraft is slowly rotated into position and the solar panels begin to acquire the sun, the panels begin to share the electrical load with the batteries. This phase can last from 30 min to 1 h. As the capability of the panels increases (i.e., as they become fully exposed to the sun's rays), the panels begin to accept a greater portion of the load until a point is reached at which they are supplying the full load. At this point (actually when the panel capability somewhat exceeds demand), the system voltage abruptly changes from that of the battery (27–29 V) to a larger but stable operating point. This voltage will be approximately 50 V after full sun acquisition is achieved. The sequence of events is depicted in Fig. 2.

During the sun acquisition phase, consideration must be given to a possible over-voltage condition resulting from the sudden exposure of cold panels to the sunlight. The temperature coefficient of each cell is about 2.3 mV/°C; the voltage increases as the temperature decreases. A worst-case analysis shows that the lowest temperature that the panels could reach prior to sun acquisition is about −80°C. (Note that the steady-state panel temperature after sun acquisition is +60°C.) Not every panel will decrease to −80°C; however, if it is conservatively assumed that this happens, the output voltage of the cell would increase by 0.32 V. Assuming 100 cells in series, the maximum voltage increase above

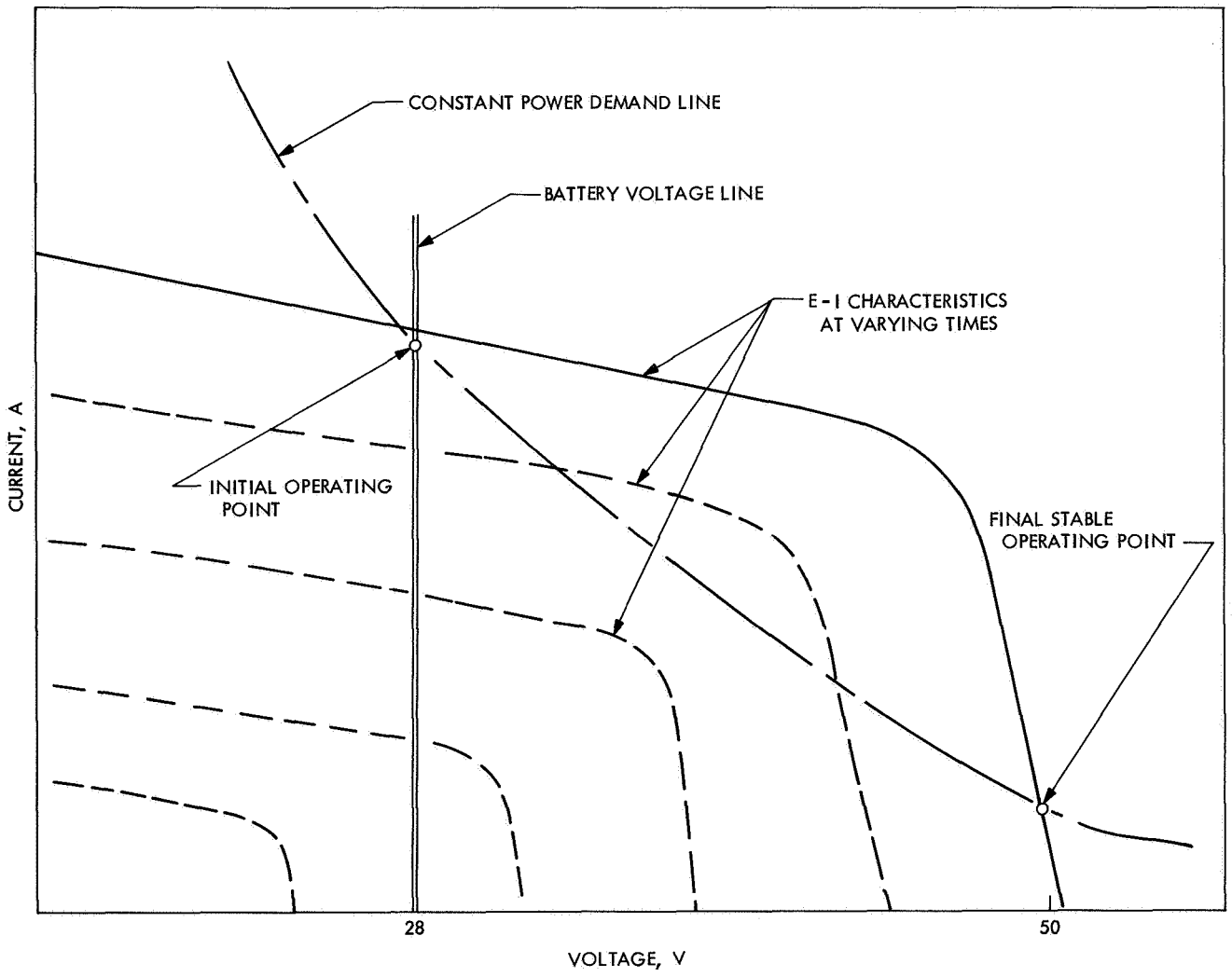

Fig. 2. Buildup of solar panel capability with time

nominal is not expected to exceed 32$\frac{1}{2}$ V. It is therefore concluded that no over-voltage condition will exist as a result of the temperature transient, since the power conditioning unit has been designed to handle such a variation in input voltage. (This design function will be discussed more fully in the following powered flight phase description.)

Following sun acquisition, the spacecraft is again rotated to acquire Canopus. This maneuver is expected to last approximately 1 h. During this period, the panels must supply approximately 250 W of power to the engineering loads. Since this demand is only about 2% of the panel capability at that time ($\sim$ 1 AU), the operating voltage will be nearly equal to the panel open circuit voltage, i.e., approximately 50 V.

2. ***Powered flight phase.*** During the next phase of the mission, the propulsion system is activated. Start-up is initiated by ground command, after which the propulsion system is slowly brought up to and maintained at a prescribed level of operation by an on-board control system.

When the solar panels are supplying the full demands of the engines, the operating voltage will decrease from 50 V to approximately 40 V. The power producing capability of the solar panels is not constant, but decreases with sun–probe distance due to lower illumination intensities. In addition, the peak power point voltage tends to increase because of lower panel operating temperatures. These variations are shown in Figs. 3 and 4.

Obviously, a method is required to regulate the power demands of the engines so that they closely match the capability of the solar panels. Specifically, the power demands of the engine (and auxiliary load demands) should always be equal to or less than the maximum capability of the solar panels.

This maintenance of power consumption is accomplished by means of a programmed engine power consumption profile that is stored in the central computer and sequencer (CC&S) on board the spacecraft. The profile is programmed at a level approximately 18% below the expected nominal capability of the panels. The CC&S periodically feeds an order signal to a feedback

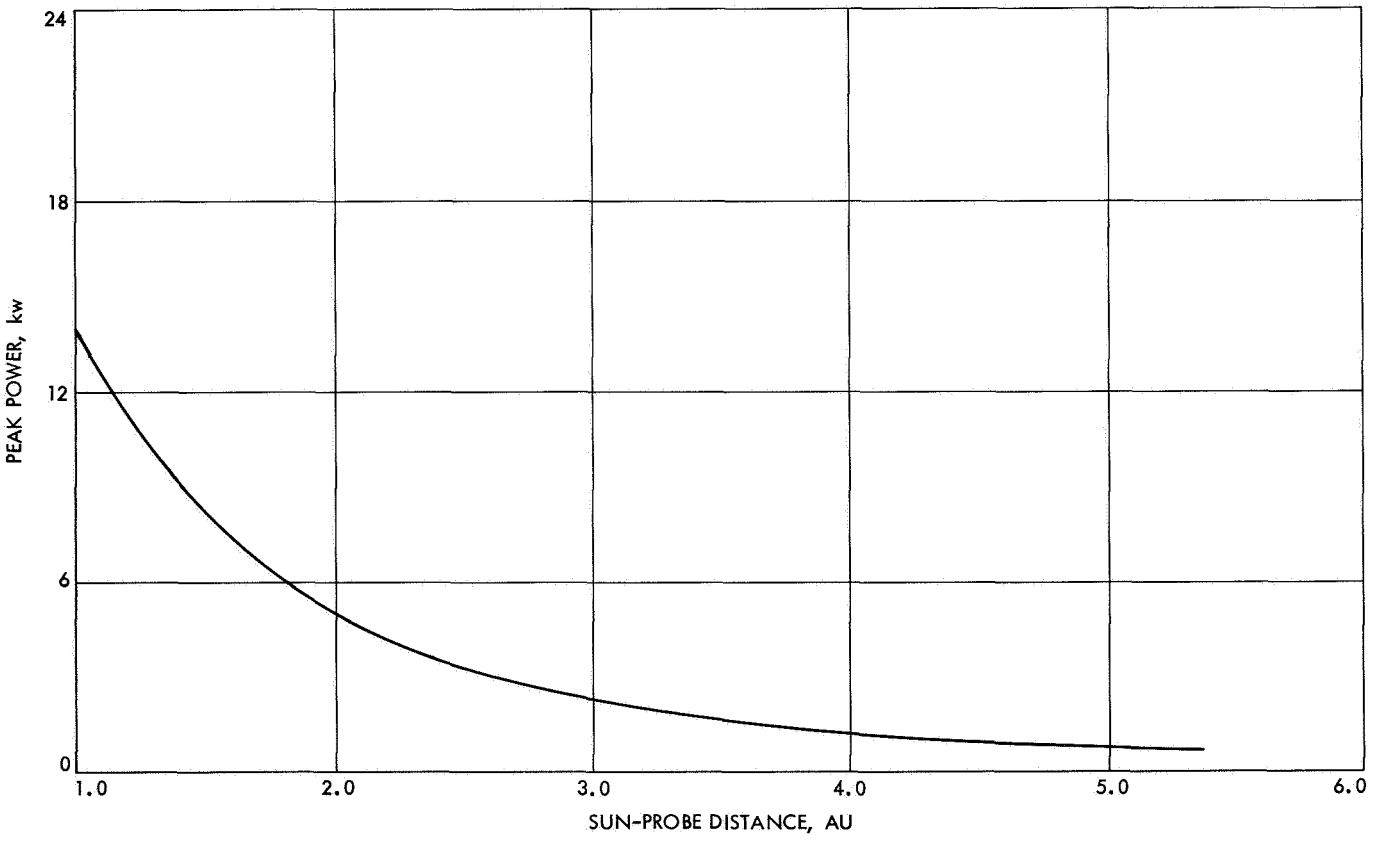

Fig. 3. Peak power from solar panel vs sun–probe distance

control system to sample the actual power level to the engines and compares this level with the stored programmed power. If the two are not equal, the engine demand is changed to compensate. The stored engine power consumption profile along with a stored thruster vector pointing program enables the spacecraft to follow a predetermined flight path.

The control system will continue to regulate the power demands of the engine to assure agreement with the stored consumption profile as long as the panel capability exceeds the programmed requirements. Under these conditions, the engines will continue to produce a continuously decreasing amount of thrust (closly matching the decreased panel capability) until engine cutoff occurs (at about 470 days), after which the mission continues in a ballistic trajectory toward the target (Jupiter).

Should the panels at any time during the nominal thrusting portion of the mission become unable to supply the power as demanded by the stored program due to excess cell degradation, the signals from the stored program are overridden by the action of a secondary control mechanism. This secondary system is essentially a maximum power point tracker, which regulates the engine load so that the engines are supplied with as much power as the panels can provide. Obviously, a reduction in engine power below the planned power consumption rate may jeopardize the completion of the mission. Fortunately, a certain amount of power reduction can be compensated for by increasing the thrusting time of the engines.

Continuous operation along the maximum power point of the panels is undesirable because of navigational

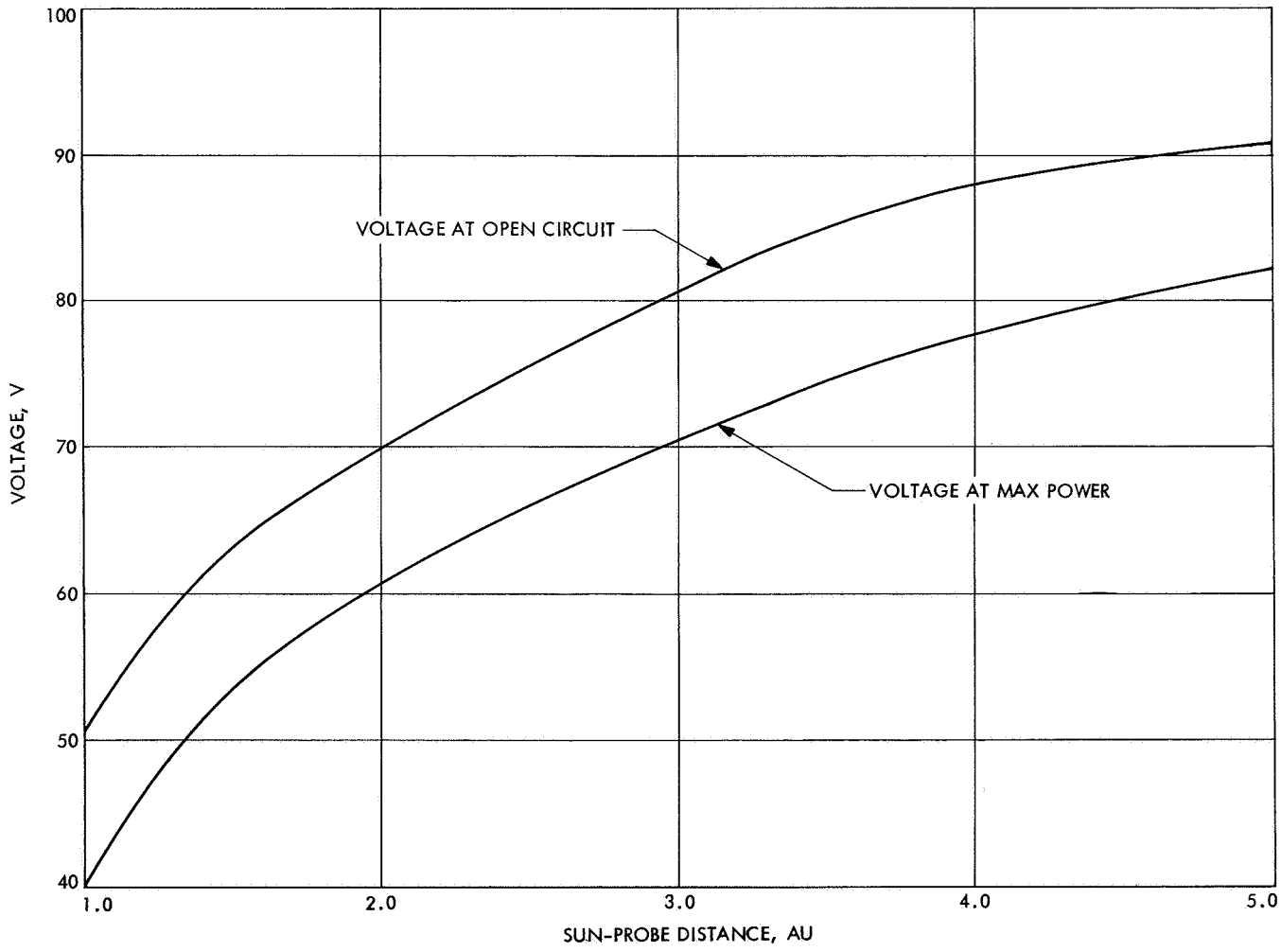

Fig. 4. Panel voltage vs sun–probe distance

problems. The trajectory of the spacecraft would follow a path dictated by the amount of power that, at any moment, happens to be available. Also, proper orientation of the thrusting forces of the engines cannot be determined unless the amount of power that will be available throughout the duration of the thrusting period is known. For this reason, once the system is operating at the peak power point of the panel, the profile of the available power must be closely monitored by ground stations in an attempt to predict its variation with time. Having (1) estimated a new power profile and (2) through an updated mission analysis determined that this profile indeed will allow completion of the mission, the CC&S located on board the spacecraft is reprogrammed by ground commands. In general this reprogramming will consist of:

(1) A new engine power consumption profile.

(2) An increase in the thrusting time of the engine.

(3) A change in the program thrusting vectors of the engines.

Control of the engine-demand requirements is then automatically transferred to the main control system (programmed power profile) and continues in this manner unless the panel capability again decreases below the programmed demands, in which case the entire correcting sequence is repeated.

During the powered flight phase of the mission, the solar panels supply not only the engines, but also the engineering and science spacecraft loads. These auxiliary power requirements are fairly continuous at 186 W. Peak demands of the attitude control system are of the order of 50 W. A detailed listing of the power consumption rates is given in Table 6.

It was previously mentioned that the electrical power generated by the photovoltaic power system will decrease with time due to the reduction in solar intensity as the spacecraft travels away from the sun. There are other effects that can reduce the power capability of the panels. In the region from 1 AU until engine cutoff ($\sim$ 3.3 AU), the solar cells are subjected to both the sporadic emissions of high-energy particles (solar flares) emanating from the sun, and possible collision with hypervelocity particles (meteoroids) residing in interplanetary space. These effects persist beyond engine cutoff; however, their importance at that time is secondary, because power requirements are then drastically reduced.

Table 6. Auxiliary power requirements during powered flight phase (470 days)

Steady state	Power, W
Telecommunications	103
CC&S	16
Cold gas A/C (standby)	15
Science	13.8
Thermal control	25
Thrust pointing control electronics	5.5
3-axis translator—gimbal engine control electronics	8
Total	186.3
Transient	**Power, W**
Pointing control stepper	10
2-axis translator	20
Engine gimbal control	20
Total peak load	50

It was found that the probability of incurring damage as a result of collisions with hypervelocity particles is insignificant when compared to the damage expected from proton irradiation of the solar cells. An evaluation of the damage that energetic protons can inflict upon the power system is discussed in detail in Section III-A-2-a of this report.

The effect of solar cell degradation due to proton flares was combined with the normal uncertainties associated with predicting the initial power of the solar array in such a manner as to allow predictions of probable deviations from nominal performance. The results of the analysis indicate that, throughout the powered flight, the solar cells would produce more than 82% of the estimated nominal power with a 95% probability at a confidence level greater than 95%.

3. Cruise phase. After approximately 470 days of powered flight, the engines are shut down and the system continues to the target in a ballistic trajectory. During this portion of the mission, the only requirement of the power system is to provide electrical power to the engineering and science loads. These requirements are shown in Table 7. As can be seen, the power requirements have increased above those in the powered flight in two areas: telecommunications and thermal control.

Subsequent to engine turnoff, the panels are capable of supplying 1950 W. Even if one considers an 18% contingency for environmental effects and a 75% power conversion efficiency, more than 1200 W of regulated power could be made available. Note that the magnitude

Table 7. Power requirements during cruise phase

Steady state	Power, W
Telecommunications	175
CC&S	16
Cold gas A/C (standby)	15
Science	13.8
Thermal control	50
Total	269.8
Transient effects (worst case)	**Power, W**
Pitch-axis jet firing	20
Yaw-axis jet firing	10
Roll-axis jet firing	20
Total peak load	50

of the contingency used in this phase is identical to that of the previous phase. This contingency is reasonable because no further decrease in the output power of the photovoltaics is expected between engine cutoff and encounter due solely to radiation damage. The primary reasons for this are: (1) a significant reduction in proton fluxes at distances greater than 3 AU, and (2) radiation hardening of the panels as a result of previous exposure.

Just prior to encounter (5.2 AU), the panel capability reduces to only 785 W because of reduced solar intensity. Again considering contingencies and power conversion losses, the available regulated power is 483 W. This power is sufficient to supply the power requirements of all the loads, which even under worst-case transient conditions require less than 320 W (Table 7).

The power conditioner for the auxiliary electronics has been designed to remain in regulation throughout a large variation in input voltage. It will accept input voltages as low as that of the battery system (~27 V) and as high as that produced by the photovoltaic system at 5.1 AU under open circuit conditions (~92 V). This unusual capability of handling large extremes in voltages makes the auxiliary power system quite stable irrespective of the variations in power requirements throughout the entire mission.

The auxiliary load power conditioner is a duty cycle switching regulator, which possesses specific characteristics that must be considered in the system design. If, at any time during the cruise portion of the mission, the power demands of the engineering and science loads exceed the maximum power capability of the panels due to either system transients or loss of sun orientation, the input voltage to the power conditioner (unregulated bus voltage) will decrease from the normal panel voltage to that of the battery system. The battery then is called upon to supply the required power demands. However, even after the transient disappears (or the sun is again fully acquired), the power system *may* remain locked at the battery voltage, and both the battery and solar panel would share the load.

Whether or not this sharing happens depends on the original operating point. Consider the panel characteristics shown in Fig. 5. Assume the system has been operating at its normal operating point and a transient in excess of the maximum power point appears. The regulating system reacts to a demand for more power by increasing the output current from the panels. Normally, if the transient power is less than the maximum power point of the panel, an increase in current moves the operating point up toward the peak power point until demand equals supply. However, in this case, the demand is greater than supply so that the current continues to increase beyond the maximum power point. The load voltage is, of course, continuously decreasing. Once the load voltage decreases to that of the battery, the battery will begin to supply current to the system. The current further increases (at fixed battery voltage) until the transient operating point is reached. Once the transient effect disappears, the current decreases until the normal operating point is reached (see Fig. 5).

Now consider the case of Fig. 6. Assume a transient forces the current to increase until the transient operating point is reached. Now if the transient disappears, the current decreases until it reaches the normal power line. However, in this case, the normal constant power line intersects the battery voltage line at a point above the characteristic curve of the panel. This intersection is a stable (but low voltage) operating point so that the system is locked at the battery voltage and both the battery and panel share the load.

This load sharing mode places a continuous drain on the battery and is, therefore, undesirable. A voltage boosting device has been added to the electrical circuit and is activated whenever such a load sharing condition is sensed. In essence, this boosting circuit introduces a voltage pulse that places the system back at the higher (stable) operating voltage of the panel. The battery system is thus deactivated and no longer supplies power to the load.

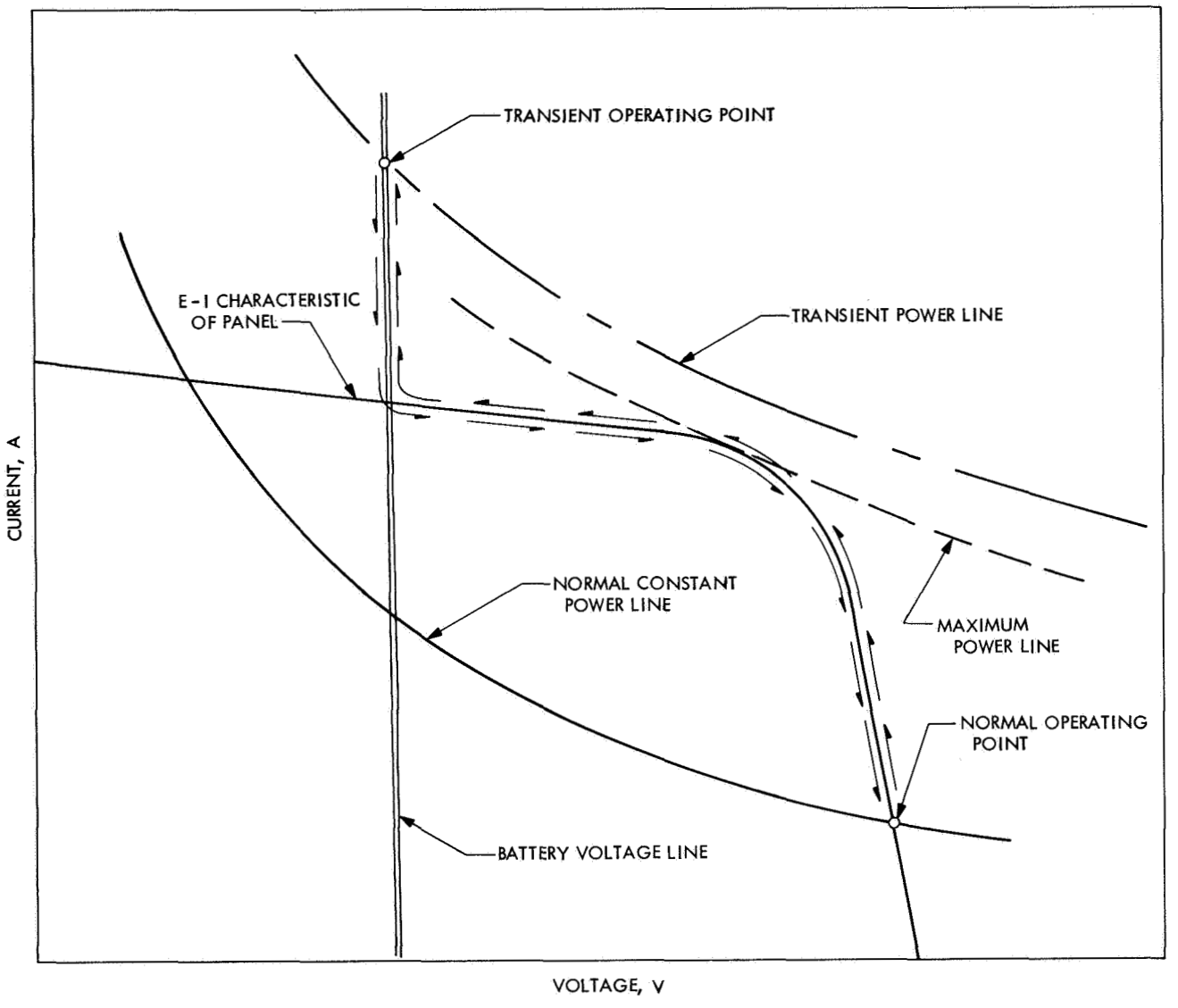

Fig. 5. Transient response of a power system that does not lock at battery voltage

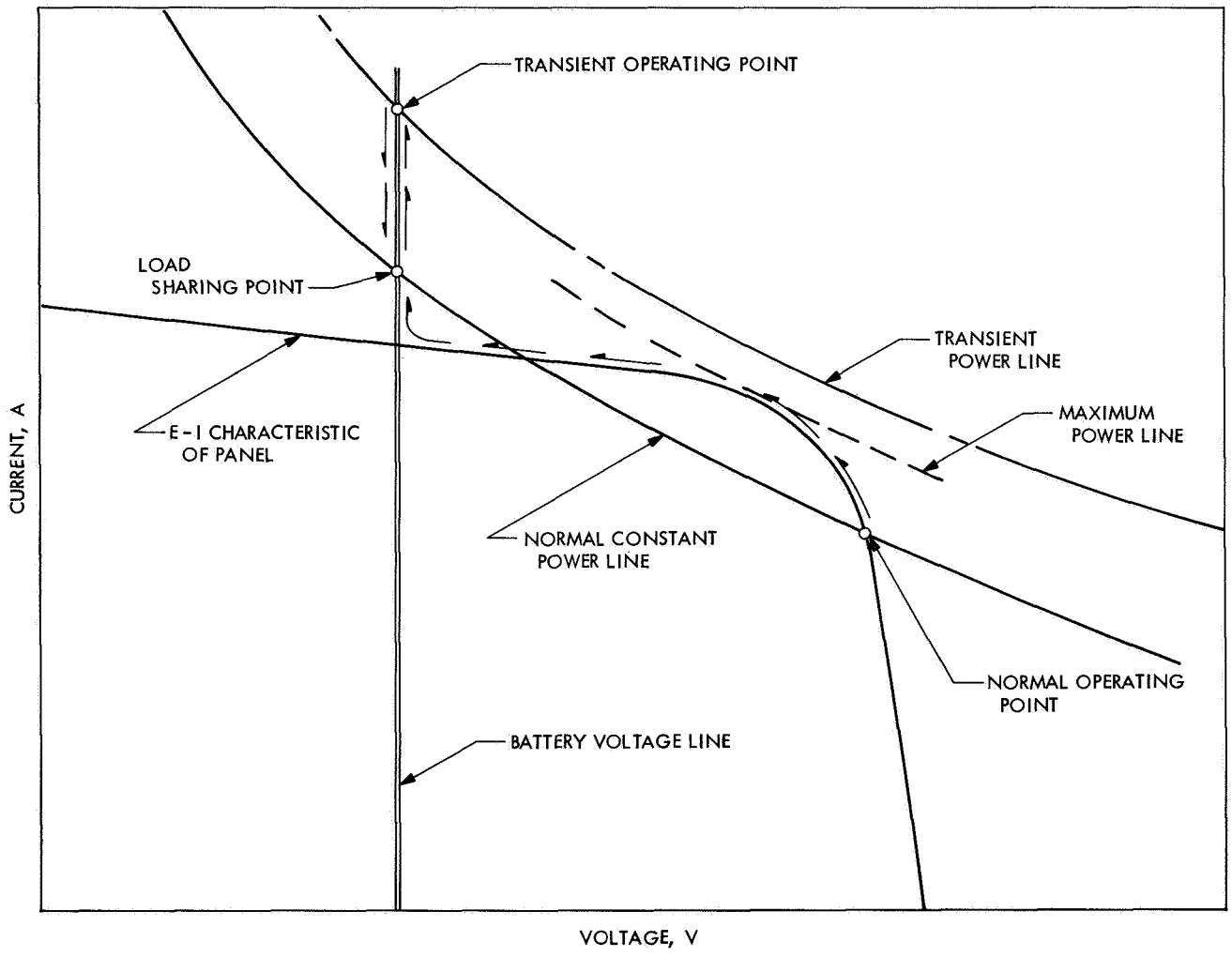

Fig. 6. Transient response of a system that can lock at battery voltage

It is interesting to note that the problem of locking onto the battery voltage is completely nonexistent during the powered phase of flight, since the panel voltage is controlled by the engine control system, which is designed to prevent operation on the low-voltage side of the peak power point.

At this point, one might question the ability of a battery to supply power to a load after 500–900 days of operation. First, in answer to this question, it should be pointed out that it is not probable that battery power will be required throughout the cruise phase of the mission. Second, as was previously shown, the panels are capable of supplying more than 200 W above the steady-state requirements, even at encounter (5.2 AU). The maximum transient load expected in this phase is of the order of only 50 W. The only condition that would demand battery power would result if a sufficiently large disturbance occurred which prevented continuous sun orientation of the panels. Although loss of solar acquisition is considered quite unlikely, a battery system capable of meeting such a contingency is discussed in a following section concerning solar occultation.

4. Encounter phase. The encounter phase of the mission can be divided into three distinct parts: (1) presolar occultation, (2) solar occultation, and (3) postsolar occultation. The specific power system problems peculiar to each of these phases is discussed below.

5. Presolar occultation. The most significant power system problem encountered during this phase is the increased radiation damage to the solar cells as a result of magnetically trapped radiation in the vicinity of Jupiter. This radiation damage begins during presolar occultation, but actually will continue throughout both the occultation and postoccultation phases.

A detailed evaluation of the magnitude of the damage that can be expected is presented in Section III-A-2-c. A significant electron flux begins at a point about 9 planet radii from Jupiter (8 h prior to solar occultation) and increases rapidly to a maximum value at 3 planet radii. The exact magnitude of this electron flux is not known. Estimates vary by more than 2 orders of magnitude.

Assuming a conservative approach (i.e., highest flux value), the power from the solar cells will have degraded by 43% at the conclusion of the presolar occultation phase due to previous proton damage and damage occurring within the Jovian electron field. The conclusion of the presolar occultation occurs about 1 h after encounter. With the use of the lower estimates for the electron flux field around Jupiter, the analysis indicates no additional damage to the solar panels beyond that previously produced by solar flares during the powered flight phase.

Based even on the conservative estimate of electron flux, it can be shown that the available electrical power is sufficient to conduct the mission. Table 8 presents a summary of the steady-state and transient load requirements during the presolar occultation phase. Assuming a 75% converter efficiency, the net power available to the spacecraft loads at the end of this phase is 340 W. The net power available is adequate to meet the steady-state requirements, but cannot handle the transient requirements. It should be pointed out, however, that the loads indicated are also worst-case values. Extremely conservative estimates of the duty cycle are selected to generate the watt-hour requirements.

Table 8. Power requirements during presolar occultation[a]

Steady state	Power, W	
Telecommunications (high mode for TWT)	175	
CC&S	16	
Cold gas A/C (standby)	15	
Science	33	
Thermal control	50	
Thrust pointing control (science pointing)	6	
Total	295	
Transient	**Power, W**	**Energy, Wh**
Gyros (on full time during last hour of this phase)	21	21
Science pointing platform motion (40% duty cycle)	10	32
Pitch-axis jets (5% duty cycle)	20	8
Yaw-axis jets (5% duty cycle)	10	4
Roll-axis jets (5% duty cycle)	20	8
Totals	81	73

[a]Length of time period is 8 h.

It was previously noted that the time period of the preoccultation would be 8 h. Only during the latter portion of this phase will the panels degrade sufficiently (due to the influence of the Jovian electron belt) to require the use of a battery to meet the transient demands. However, for conservatism, the transient requirements were all based on an 8-h duration. The battery system that can meet these requirements and subsequent demands imposed by the spacecraft system is discussed fully below.

6. Solar occultation. Loss of solar power is the critical problem during this phase. As the spacecraft flies by Jupiter, the planet will occult the sun for about 1 h. Power requirements, including transient effects, remain essentially the same as those for the presolar occultation phase. Approximately 315 Wh of electrical energy are necessary; a detailed summary is given in Table 9. The conditioned power requirements, considering a 75% converter efficiency, are 417 Wh.

The most efficient source of power from an energy density standpoint is chemical. Both high-density silver-zinc batteries and so-called remotely activated batteries are considered. The latter type batteries remain in a dry state and are activated by the introduction of potassium hydroxide shortly before use. However, their performance is inferior to that of a conventional silver-zinc battery system from a specific weight standpoint; for the same power, they generally weigh from 50 to 100% more.

Table 9. Power requirements during solar occultation[a]

Steady state	Power, W	
Telecommunications (high mode for TWT)	175	
CC&S	16	
Cold gas A/C (standby)	15	
Science (no TV)	25	
Thrust pointing control	6	
Thermal control	50	
Gyros	21	
Total	308	
Transient	**Power, W**	**Energy, Wh**
Science pointing	10	4
Platform motion (maximum duty cycle 40%)	20	1
Pitch-axis jets (5% duty cycle)	20	1
Yaw-axis jets (5% duty cycle)	10	0.5
Roll-axis jets (5% duty cycle)	20	1
Totals	80	7.5

[a]Length of time period is 1 h.

The conventional silver-zinc system has one major drawback. Wet storage lives of 2 to 3 years have not yet been fully demonstrated. There is some question as to whether full capacity or even a significant portion of its capacity can be extracted from a battery after long-term storage at normal spacecraft operation temperature (60°F), because the electrolyte reaction between the battery plates and separators causes long-term deterioration of the system. It is known, however, that low temperatures (less than 50°F) can substantially retard deterioration. In fact, if the cells are stored (wet) at temperatures of 0°F, lifetimes of 3–5 yr can be realized. However, only a very limited amount of power can be drawn from the battery at this low temperature. Return of the temperature to above 50°F is necessary to enable the battery to supply power for the occultation period.

The battery system selected for the Jupiter probe application consists of two packages, each capable of producing 600 Wh at 27–29 V. One battery package will be used during launch and remain on standby after the solar panels begin to produce power. Its temperature may be maintained at 50–80°F. This temperature range will minimize deterioration, yet is high enough to allow full-capacity operation. Such a battery should have a lifetime of at least 500–700 days. Experiments at JPL are presently being conducted to determine the actual wet standlife of AgZn batteries under varying conditions.

The second battery package will be maintained in storage at very low temperatures (approximately 0°F) for the first 700 days of the 900-day mission. Then it will be activated by raising its temperature to about 55°F with electrical heaters. This approach should guarantee the availability of electrical power during the critical solar occultation phase.

The results of the experiments presently being conducted at JPL will determine the optimum time for transition from one battery to the other. The use of a 600-Wh battery to meet the 410-Wh requirement allows a margin for either some battery capacity loss during storage, and/or somewhat higher periods of solar occultation.

7. Postsolar occultation. This phase is defined as that period from conclusion of solar occultation until all data obtained during the encounter maneuver have been transmitted back to earth. This time period may be as much as 36 days.

As with the presolar occultation phase, radiation damage to the solar cells due to trapped electrons in the vicinity of Jupiter is the critical problem. By the time this phase begins the panels have been radiation hardened (as a result of the two previous phases) to the point that any additional radiation experienced during this final phase will have little effect. It is expected that the panel power will decrease to about 47% of the undegraded value by the end of the postsolar occultation phase. This estimate assumes the use of the conservative electron flux values.

Based on a 75% converter efficiency and a 47% power decrease due to radiation damage, the panels are expected to be capable of supplying 312 W of regulated electrical power to the spacecraft loads. The power demands of the spacecraft are given in Table 10. The steady-state spacecraft loads are about 270 W. The transient loads, which include 71 W of continuous power for a half hour at the start of the phase, will be handled by either the extra capacity of the panels or, if necessary, the battery system.

The attitude control jets will have a very low duty cycle (about 0.3%) during the greater portion of the post-occultation phase. However, these low demands over a long period (approximately 36 days) could induce a sizable drain on a battery system, which has already been substantially depleted during the presolar and solar occultation phases. Fortunately, the panels can produce sufficient excess power over that required by the steady-state loads to maintain the battery at an adequate state of charge to supply the transient loads.

Table 10. Power requirements during postsolar occultation[a]

Steady state	Power, W	
Telecommunications (high mode for TWT)	175	
CC&S	16	
Cold gas A/C (standby)	15	
Science (no TV or IR)	14	
Thermal control	50	
Total	270	
Transient	**Power, W**	**Energy, Wh**
Gyros (during first ½ h of this phase only)	21	11
Pitch-axis jets (0.3% duty cycle)	20	52
Yaw-axis jets (0.3% duty cycle)	10	26
Roll-axis jets (0.3% duty cycle)	20	52
Totals	71	141

[a]Length of time period is 36 days.

III. Subsystem Description

This section presents a detailed component description of the four power subsystems.

A. Photovoltaic Power Source Subsystem

1. Design and performance characteristics. The photovoltaic array proposed for the Jupiter probe will deploy 1476 ft². The array consists of four identical solar panels, each containing nine subpanels. Each panel will be covered with approximately 75,600 N/P, nominal 1-ohm-cm base resistivity, silicon solar cells having dimensions of 0.788 × 0.788 in. The cells are 0.008-in. thick and are protected with a 0.003-in. thick, 0211 microsheet cover having a 0.410-micron cutoff filter. The cells are bonded to a 0.003-in. fiberglass mesh, which in turn is pretensioned and bonded in beryllium frame assemblies to form the cell mounting substrate and array structure. Figure 7 presents drawings of the lightweight construction of the array.

The four solar panel assemblies are stowed in a plane parallel to the thrust axis of the launch vehicle. A boost tie-down system preloads the stowed assemblies such that they will act as an integral structural unit during the launch phase of the mission. A structural shear-tie system is used between the subpanels on each of the four panel assemblies. The launch configuration is designed to stow within the shroud of the *Atlas/Centaur* boost vehicle.

Pyrotechnic devices on each panel assembly and cable cutters are used to release the structural tie-down system. A cable drive system is presently being considered for array deployment. The cable drive system is attached to the spacecraft and opens each of the four panel assemblies. As the cable, which is attached to the main center subpanels through a series of pulleys, is tensioned by the cable drive assembly, it deploys the panel assembly. The auxiliary subpanels, located on the fourth and fifth main subpanels, are deployed by a spring and damper system.

The design of the Jupiter mission solar array is a scaled version of the Large-Area-Array Technology Development Program being developed under JPL Contracts 951653 and 951934. The array being developed under this contract is a 5000 ft² assembly, which has, as a goal, a minimum power-to-weight ratio of 20 W/lb. A model of this array in the deployed configuration is shown in Fig. 8. The array is approximately 25 ft wide and 30 ft from tip to tip.

The array design includes a total of 100 solar cells that are connected in series to meet the nominal voltage requirements at earth space and a panel temperature of 55°C. To meet the power requirements of the spacecraft, it is assumed that solar cell packing densities of 90% can be achieved, resulting in 223 cells per ft². Based on this assumption, the array will deploy 1330 ft² of active cell area for a net raw-power capability of approximately

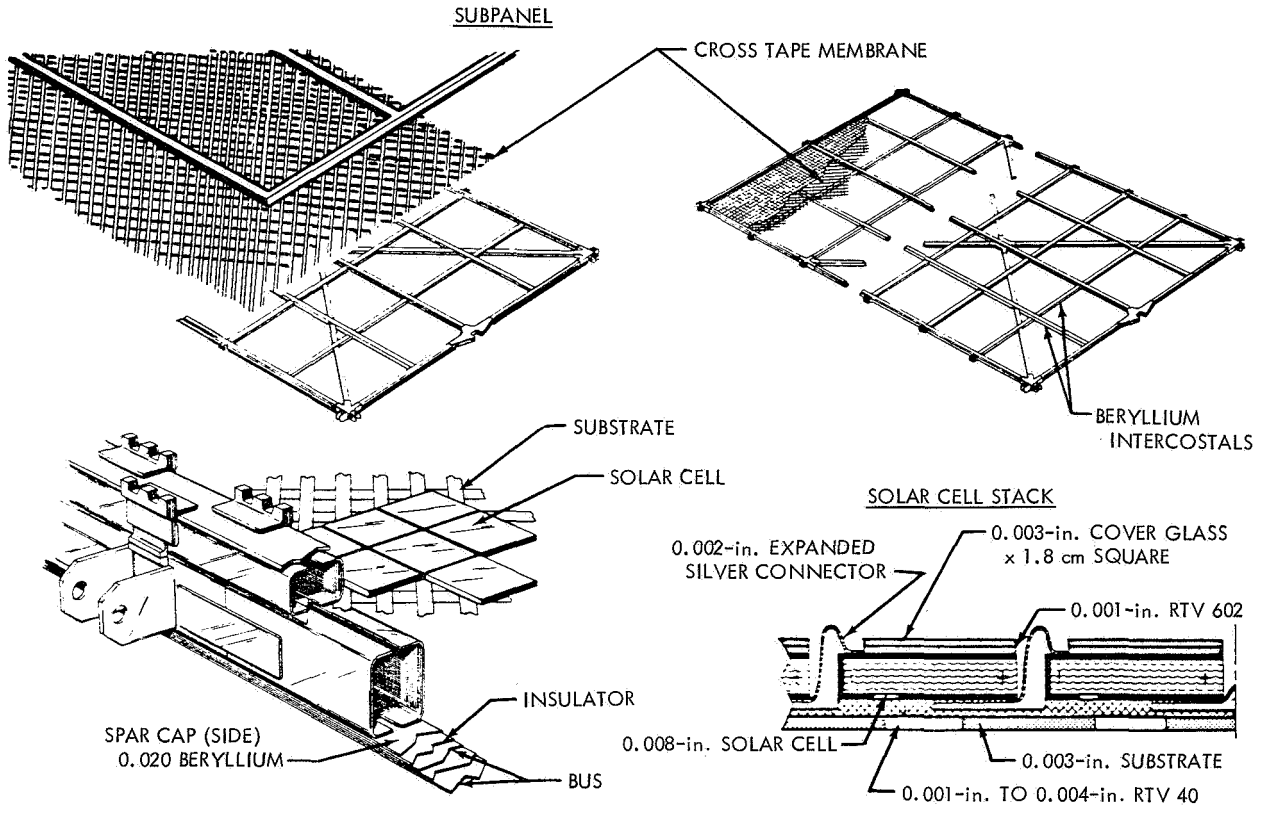

Fig. 7. Solar array construction

9.5 W/ft² for the total deployed area. The total raw-power capability of the array at 1 AU is expected to be 14.0 kWe.

The nine subpanels of each panel have a total rectangular deployed area of approximately 41 ft². The dimensions of the subpanels are approximately 9 ft 6 in. × 4 ft 5 in. Within these subpanel dimensions, approximately 8400 solar cells can be mounted. Each subpanel will contain 12 parallel sections of 7-cell modules with 100 cells connected in series. *Each* of these 12 sections is diode isolated to provide maximum redundancy (Fig. 9).

The current, voltage, and power capability of silicon solar cells are dependent on the temperature and intensity environment to which they are exposed. The design of the array in this study is based on a passive thermal control system; therefore, the operating characteristics of the array are mainly a function of the varying intensity.

For the intensity values used in this study, it was assumed that the intensity varies as the inverse square of the distance from the sun. The intensity expected during the Jupiter mission will vary from approximately 140 to 5 mW/cm². The passive thermal control system used on the array depends primarily on the properties of the solar cell/filter cover system and coatings applied to the dark side of the array. The design of the array provides for a 0.002-in. thickness coating of RTV 40 applied to the dark side of the panels. The emittance (ϵ) and solar absorptance (α) values for the cell/filter cover and RTV 40 result in an α/ϵ ratio of approximately 0.50 (where α/ϵ is defined as $\alpha/\epsilon_{\text{front side}} + \epsilon_{\text{back side}}$). The expected temperatures of the array based on the α/ϵ ratio are shown in Fig. 10 as a function of intensity. The thermal control system is designed for optimization in the deployed configuration.

The solar cell suggested for use in the array for the Jupiter mission, as previously mentioned, is subject to wide variations in temperature and intensity in the performance of this mission. The characteristics of this particular cell have been under investigation for approximately 2 yr. The performance of these cells has been determined empirically, and computer programs (Ref. 2) have been generated to predict performance characteristics over the heliocentric distances traversed during a Jupiter mission.

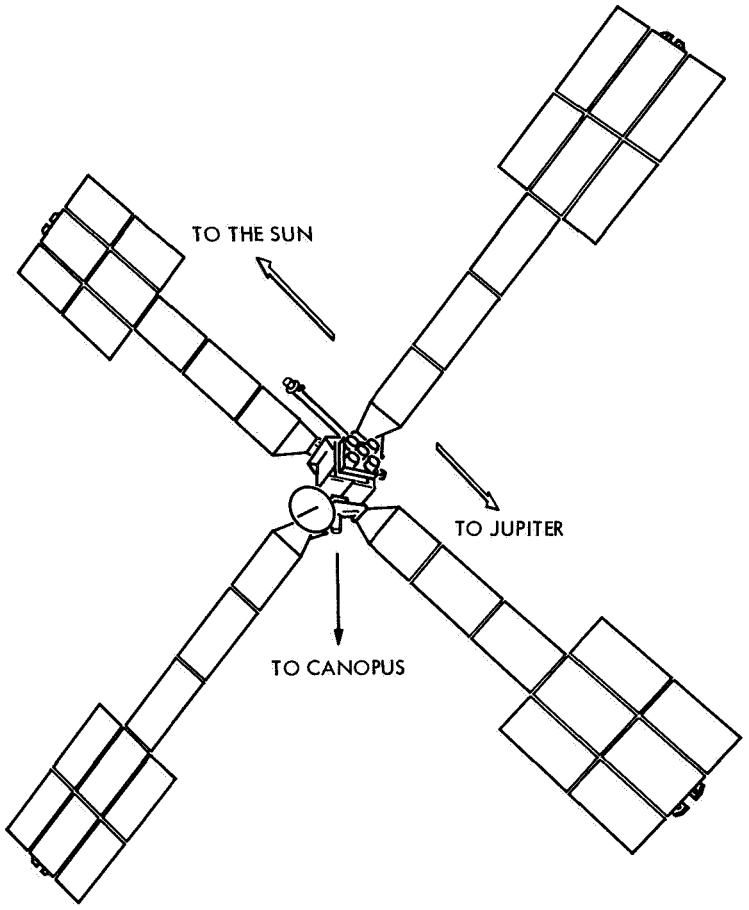

Fig. 8. Model of solar array (deployed condition)

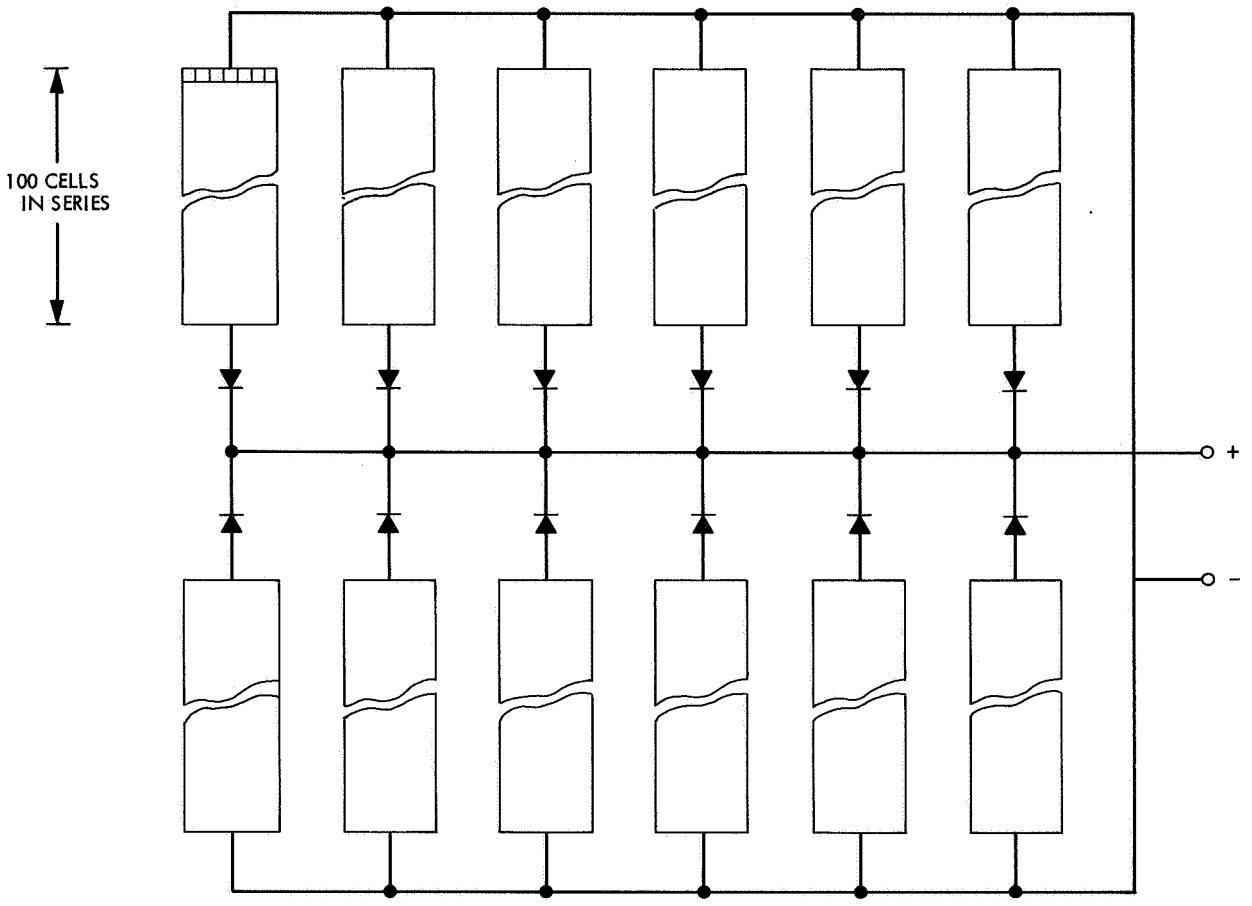

Fig. 9. Subpanel electrical block diagram

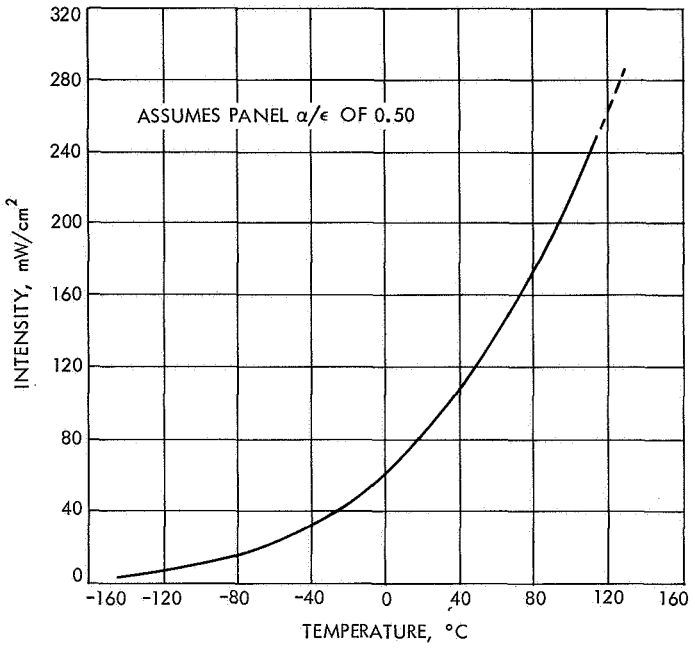

Fig. 10. Panel temperature vs intensity

Equations for voltage and current for changing light levels and cell temperatures are (Ref. 2):

$$I_2 = I_1 + I_{sc_1}\left(\frac{L_2}{L_1} - 1\right) + \alpha\,(T_2 - T_1)$$

$$V_2 = V_1 - \beta(T_2 - T_1) - \Delta I_{sc} R_s - K(T_2 - T_1)I_2$$

$$\Delta I_{sc} = I_2 - I_1$$

$$P_2 = I_2 V_2$$

where

I_1 = reference current coordinate

I_2 = extrapolated current coordinate

I_{sc} = short circuit current

I_{sc_1} = short circuit current of reference data

K = curve correction coefficient; $1.25 \times 10^{-3}\ \Omega/°C$

L_1 = reference incident solar intensity

L_2 = equivalent solar intensity to be investigated

P_2 = predicted power output

R_s = cell series resistance; 0.5 Ω nominal

T_1 = reference cell temperature

T_2 = cell temperature to be investigated

V_1 = reference voltage coordinate

V_2 = extrapolated voltage coordinate

α = short circuit current temperature coefficient

β = open circuit voltage temperature coefficient

A typical current-voltage curve of the selected cell for this array design is shown in Fig. 11. In performing the above transformation, it is necessary to treat α and β as variables with solar intensity and cell types. These variables are shown in Fig. 12.

The characteristics of the proposed 0.008-in. thick silicon cell have been measured and have compared favorably with computer generated data over ranges of 0.7 and 5.0 AU. The measured values of cell maximum power are shown in Figs. 13 and 14 as a function of temperature and intensity, respectively. With the use of the above data, the available power output of an array has been determined and is plotted in Fig. 15 as a function of sun–probe distance.

The total weight of the solar array system, including the tie-down and deployment system, is 676 lb. The weights of the individual components of the array are scaled from the Large-Area-Array Technology Development Program being conducted by the Boeing Company under JPL Contract 951653. The scaling of the array weight takes into account the additional complexity of the stowed configuration and the lower voltage anticipated in the design. The weight breakdown is given in Table 11.

Table 11. Component weight breakdown of selected solar array design

Components	Weight, lb/ft²
Cell stack, substrate, and thermal coating	0.182
Beryllium frame structure	0.173
Mechanisms, springs, dampers, and deployment	0.049
Electrical wiring, diodes, and connectors	0.051
Total	0.455

Based on the total array weight of 676 lb and the estimated 14-kWe raw power available at earth, the power-to-weight ratio of the photovoltaic power system is 20.7 W/lb. Confidence has been established in obtaining the above designated allowances of weight by actual fabrication of assemblies in lab models and a 16-ft² prototype panel assembled for the Boeing program.

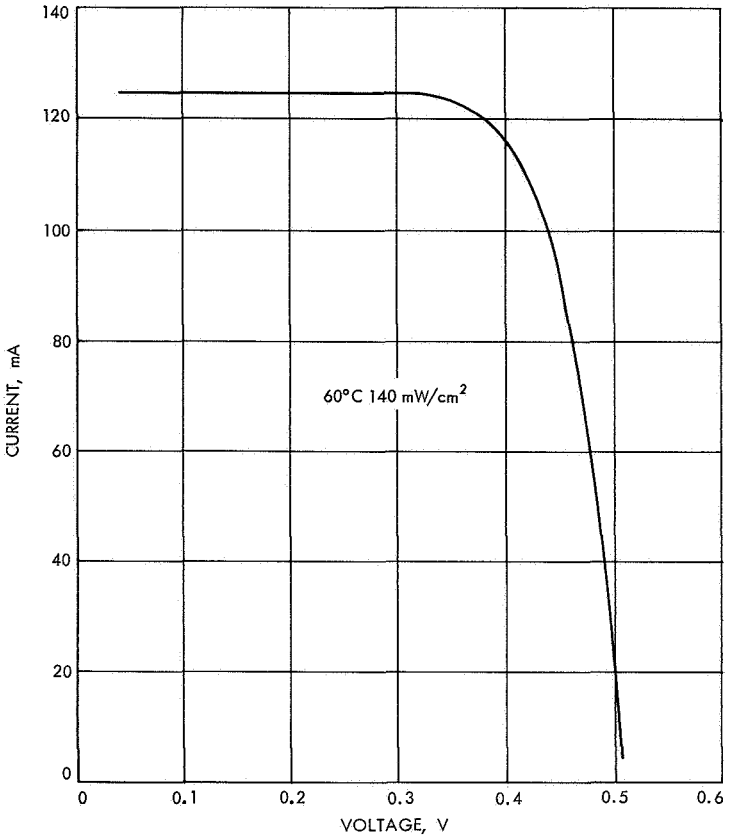

Fig. 11. Typical I-V curve of thin solar cell

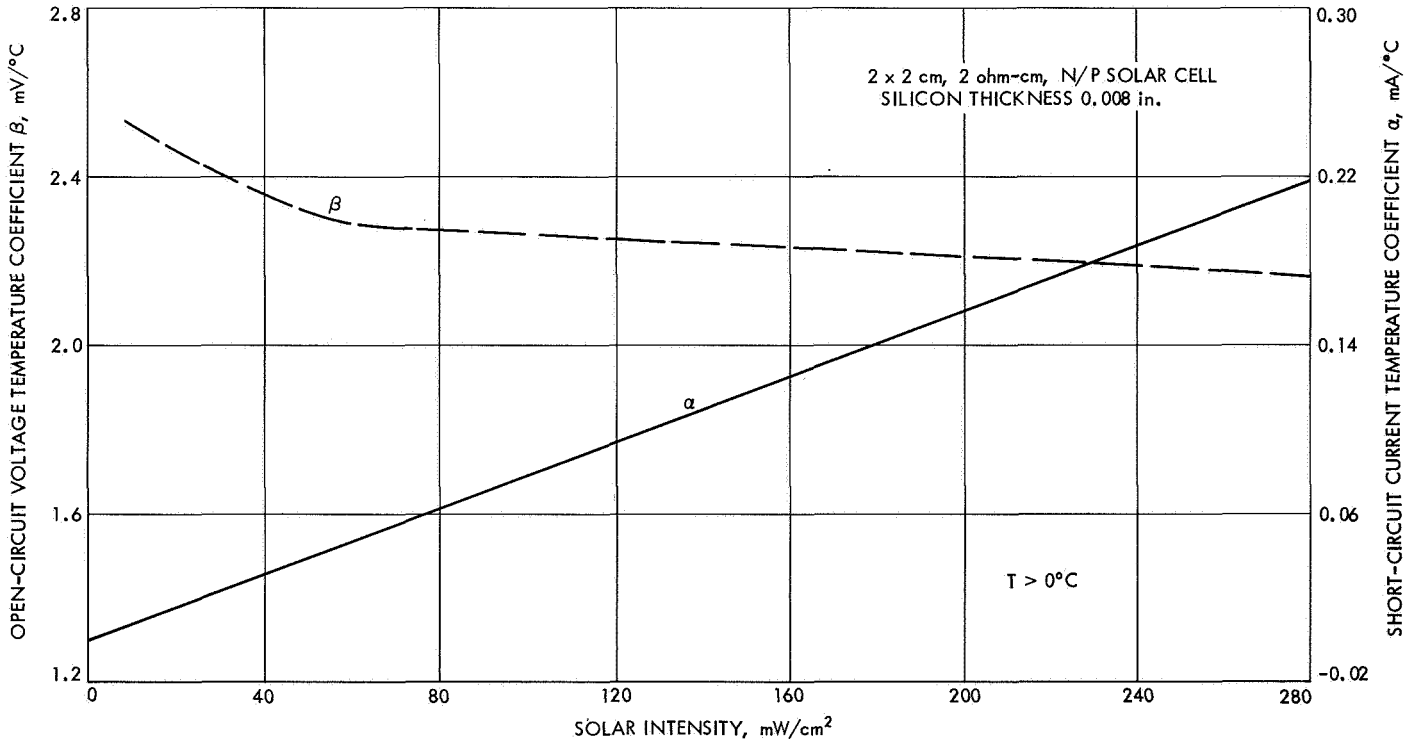

Fig. 12. Temperature coefficients vs intensity

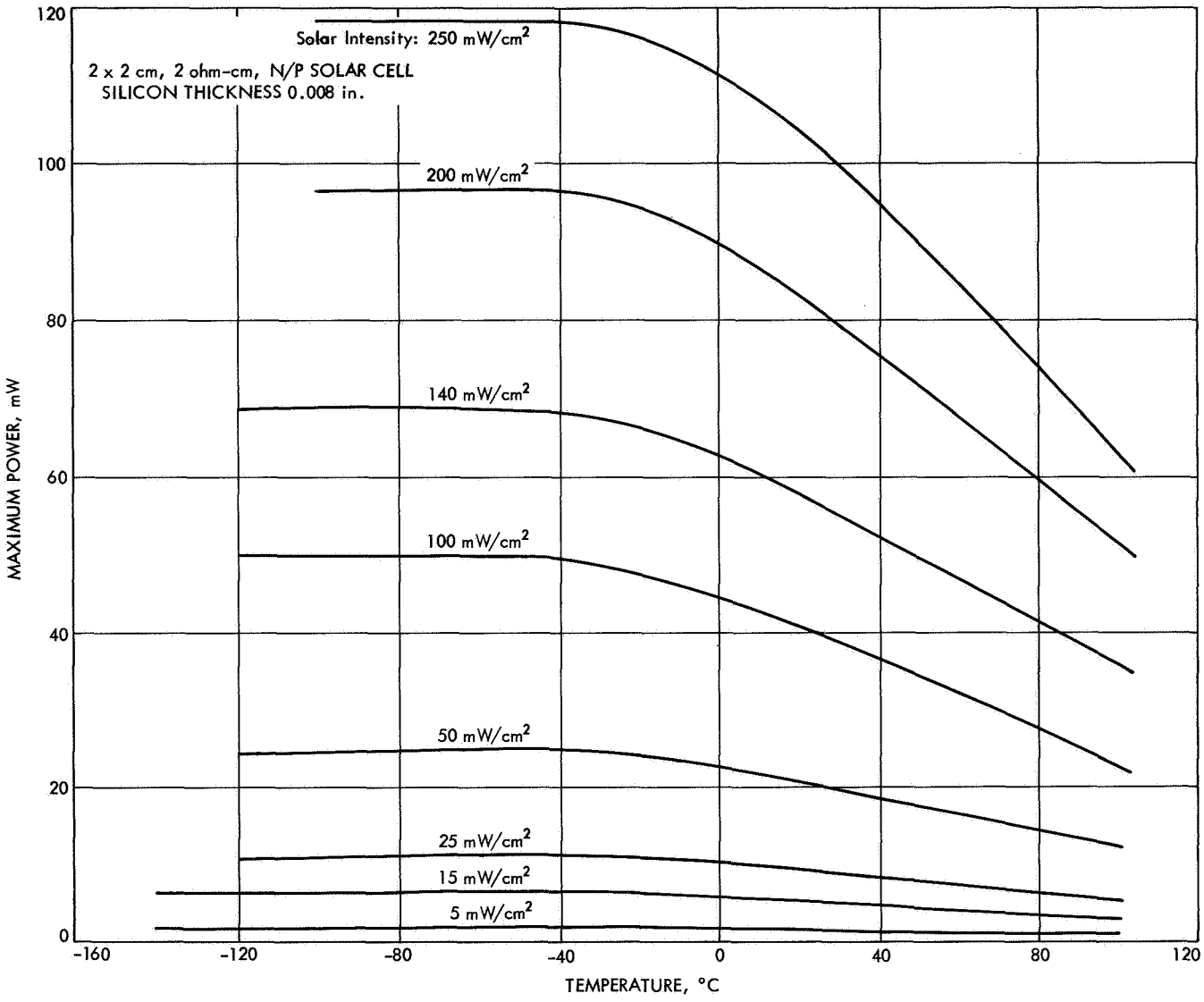

Fig. 13. Power as a function of temperature

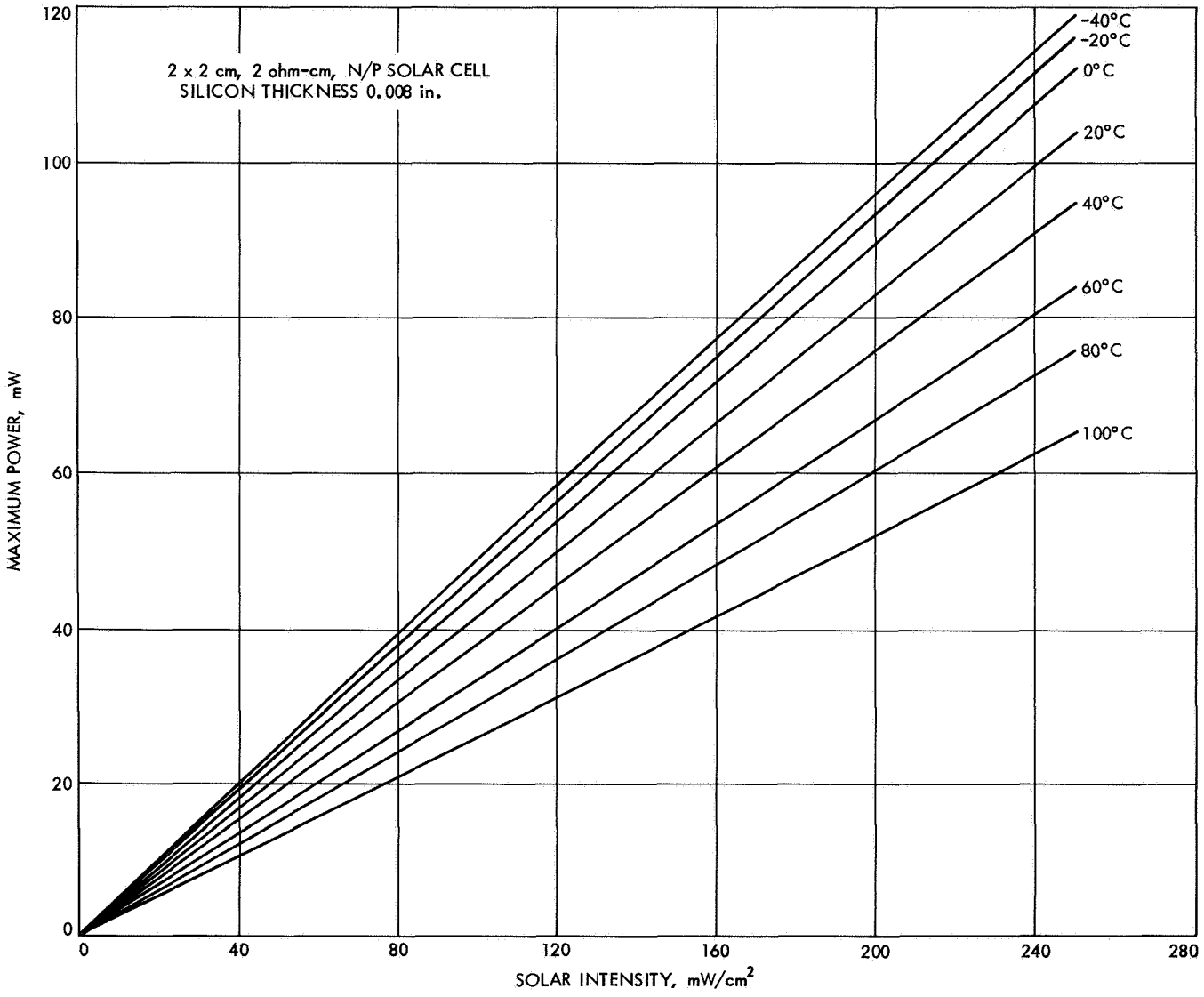

Fig. 14. Power as a function of intensity

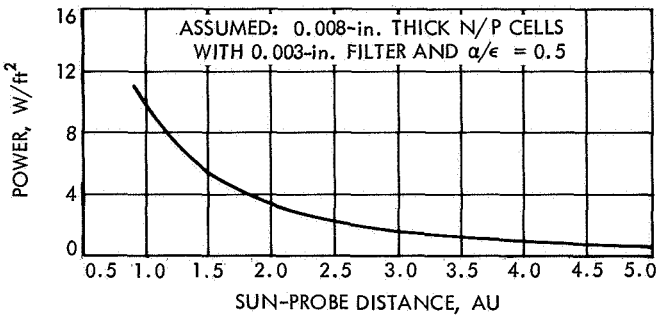

Fig. 15. Power output as a function of sun–probe distance

During the assembly of the 16-ft² prototype panel, calculations were performed to estimate the total weights of the various components in the completed panel. Figure 16 shows a graphic comparison of the actual weights to those calculated, reflecting good correlation with the analysis. The completed 16-ft² prototype panel exhibited a total weight of 6.87 lb and, based on electrical measurements, would be capable of approximately 23.5 W/lb if it were completely covered with cells. This value is greater than achievable in an actual system because there is no hardware on the assembly such as hinges, springs, dampers, and pyrotechnic and release devices.

Certain factors must be considered to establish minimum power output levels from the array in order to guarantee spacecraft power demands. These factors are

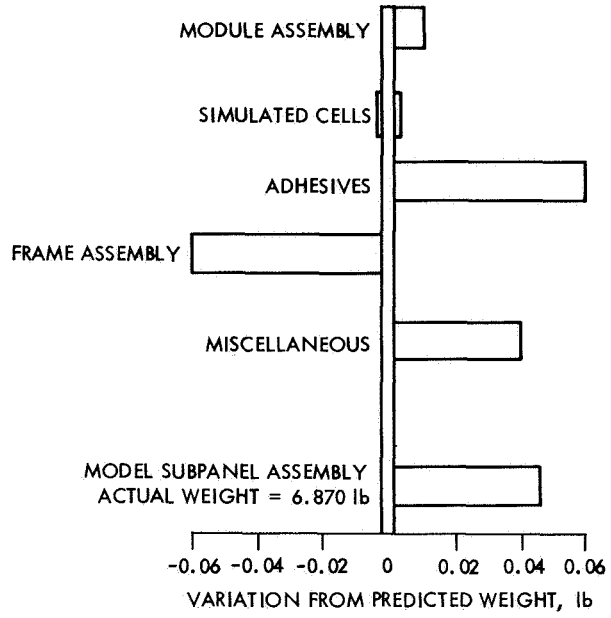

Fig. 16. Actual weight variation from predicted

related to power prediction capabilities and actual measurement tolerances involved in establishing base information. Figure 17 shows a graphic summation of these factors. The total uncertainty for prediction of power in space is ±8% and must be accounted for in the design of the photovoltaic power subsystem.

2. ***Environmental effects on performance.*** Throughout the duration of the mission, the photovoltaic power system will be subjected to the degradative effects of particulate radiation emanating from the sun and hypervelocity particles residing within interplanetary space. During encounter with the planet Jupiter, the power system will be further subjected to the irradiation effects of energetic electrons trapped in the magnetic field surrounding the planet.

In this section, the magnitudes of these various effects are predicted. It is found that the probability of incurring damage as a result of collisions with hypervelocity particles (meteoroids) is insignificant when compared to the damage expected as a result of proton irradiation of the solar cells.

In the period from launch to encounter, it is expected that the power system will degrade less than 18% due to the effects of solar flares. Predictions of the decrease in power during the encounter phase as a result of the electron field surrounding Jupiter give rise to some conjecture. The various flux models that are available for estimating the intensity of the electron field differ by more than two orders of magnitude. Assumption of the upper limit for the flux field results in predicting nearly a 50% decrease in power-plant generating capability. The use of the lower limit shows no damage to the solar cells beyond that which has already been received due to solar flares.

a. Solar flare irradiation. The proposed Jupiter probe contains a power plant, composed of solar cells, which is vulnerable to the sporadic emissions of high-energy particles (solar flares) emanating from the sun. The purpose of this section is to present a relatively unsophisticated treatment for predicting the power degradation that could be experienced during the proposed mission due to proton irradiation.

The procedural technique is briefly as follows. A probabilistic approach is used to convert available proton event data covering the years 1956 to 1963 into curves for accumulative probabilities of receiving a given flux (or less) as a function of total integrated flux. This conversion is done for various mission times of 6 mo, 1 yr,

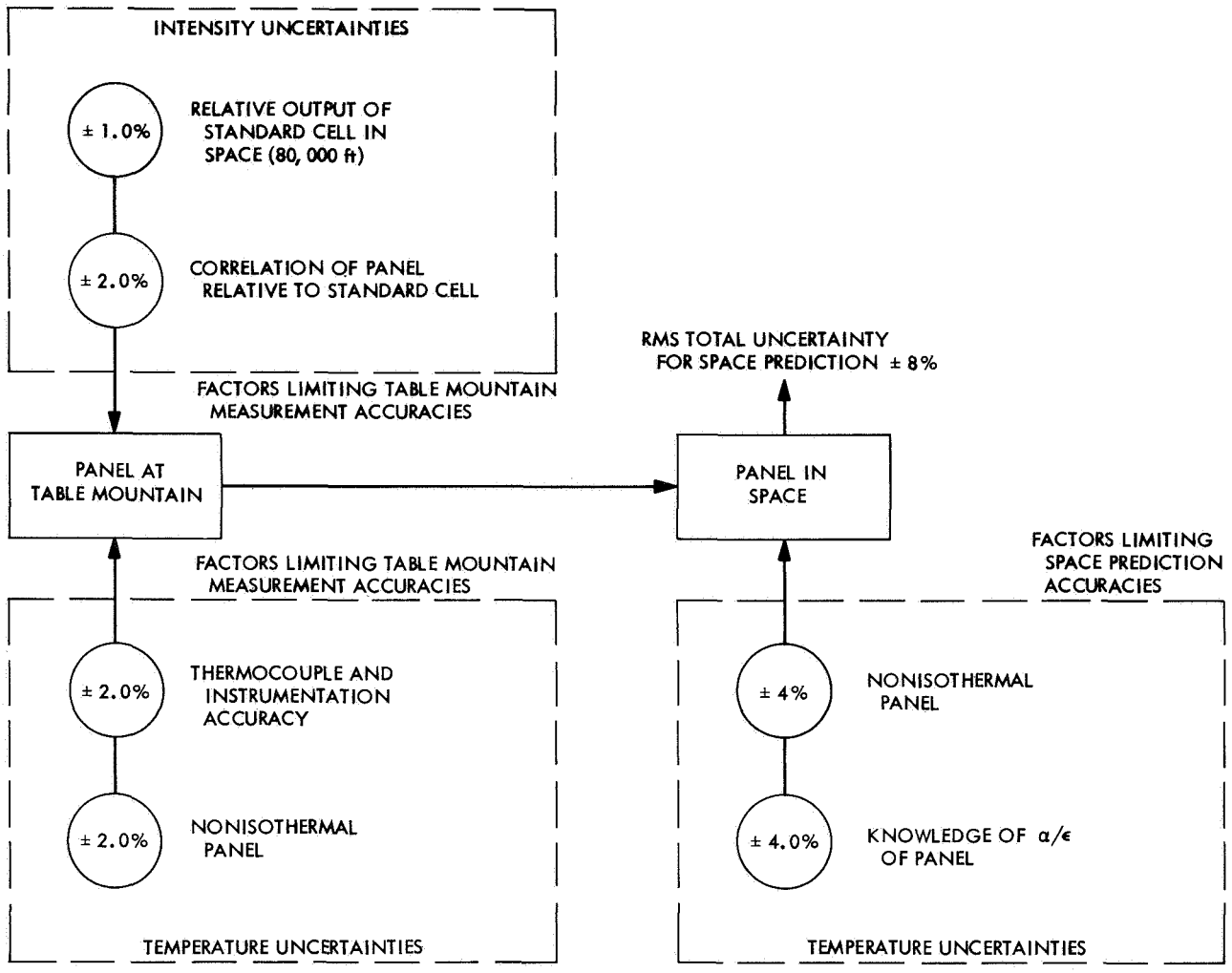

Fig. 17. Solar panel contingency factors

and 2 yr. A 95% confidence band is next established about the probable estimate. These curves can now be used to predict the total proton flux that can be expected for a given mission time. Since data on solar cell degradation as a function of integrated proton flux and energy spectrum are lacking, it is convenient, for analytical purposes, to convert the integrated proton flux into an equivalent 1-MeV electron flux for which degradation data do exist. This conversion is accomplished by utilizing the functional relationships of Rosenzweig (Ref. 3). After establishing the magnitude of the equivalent electron flux, empirical data relating solar cell power degradation and flux density and proton energy spectrum are then used to predict the amount of power loss.

The problem of predicting the actual panel output power during the mission is complicated by the fact that there is an uncertainty associated with predicting the initial power of the solar array. A mathematical approach is used to combine the uncertainties associated with predicting the initial power (by assuming that the variation of the power about an estimated mean is gaussian) with the effects of solar cell degradation. The results of this analysis indicate that the solar cells will degrade a maximum of 18% with a 95% probability at a confidence level greater than 95%. Also, 60% of this degradation occurs within the first month of the 900-day mission.

A trade-off analysis was also performed to show that the selected solar cell parameters (i.e., cell thickness, base resistivity, and proton shield thickness) are optimum on the basis of 1969 state of the art technology. Specifically, the use of a more radiation resistant design would not result in a lighter weight power system.

The power plant for the subject Jupiter probe consists of four 350-ft² solar panel arrays. Each panel contains N/P 1-ohm-cm base resistivity solar cells protected with a 0.003-in. thick window covering of 0211 Corning microsheet. The cells, which are 0.008-in. thick, are bonded to a 0.003-in. fiberglass mesh backing with a 0.002-in. RTG silicon adhesive. The effective cell area covered by the fiberglass backing is 38%. Both the cover glass and cell subtrate are assumed to provide an effective uniform density of 19 mg/cm² for proton shielding calculations. Such a shield will effectively preclude proton energies of lower than 3 MeV from reaching the sensitive area of the solar cells.

A probabilistic approach is used in determining the total integrated flux of protons reaching the solar panels. The intensities of the flares, which have been measured at the earth, have been found to vary with time and correlate well with the activity of the sun as measured by the sunspot number. High sunspot numbers coincide with periods of high proton flare activity. The activity at the sun is quite cyclic, going through periods of low and high activity. The period of these cycles as observed over the past 215 yr varies between 7.5 and 16 yr and averages about 11.2 yr. If it were possible to predict with reasonable confidence the portion of the solar cycle that the mission would be operating within (and if the flux distribution and energy spectrum over that cycle were known exactly), then accurate estimates of the integrated proton flux could be made. However, this is not the case.

Since the mission is presently planned for a 1976 launch and the period of the sun cycle varies by as much as 4 yr about a mean, it is not possible to state *a priori* exactly where the mission would occur within the cycle (i.e., whether in a period of low or high activity). Moreover, data showing the variation of proton intensity within the cycle are available only for part of the last complete cycle covering the years 1954 to 1964. This lack of complete data makes accurate estimates of proton fluxes difficult; therefore, a bit of conservatism is warranted.

The numerical computations* for determining the probability of a spacecraft receiving a given integrated flux during the specified time assumed an equal probability of the mission occurring anywhere within the given sun cycle for which proton data exist. About 68 proton events were measured during the periods from 1956 to 1963. During the first two years of the cycle (1954–1956), good techniques for measurement of the solar fluxes were unavailable. During the last year of the cycle (1963–1964), no activity was encountered, although measurements were attempted. For conservatism, the periods of no measurable activity were not included in the evaluation. Thus, the probability numbers were based solely on the 68 proton events that occurred between 1956 and 1963, and were assumed to be representative of the total flux that can be encountered in subsequent cycles.

From the data and the assumption of equal probability within any portion of the cycle, curves of probability of receiving an integrated flux greater than N as a function of the flux N for a given mission time were constructed.

Typical curves for a 6-mo mission are given in Fig. 18. Three points should be noted.

(1) The data are based on the flux intensity near earth (1.0 AU). In the actual mission, the spacecraft moves continuously away from the sun and toward Jupiter so that the variation of proton intensity with sun–probe distance must be considered. The corrections to the basic data to account for this effect are discussed later.

(2) The second point to observe is that the integrated flux shown in Fig. 18 include only proton energies in excess of 10 MeV. A considerable number of protons exist between 10 and 3 MeV (the assumed cut-off energy due to cell self-shielding), and they are taken into account by considering the energy spectral distribution of the protons. The spectral distribution used in the calculations of this report is given in Fig. 19.

(3) The final point concerns the confidence that can be placed on the estimated probability curve in view of the limited data available in determining the estimate. The 95% confidence limits have been determined and are shown in Fig. 18. Thus, if one wanted the probability of receiving a flux of 10^{10} protons/cm² or greater with 95% confidence, he would determine, from Fig. 19, a value of 30%.

A proton flux having been established with the use of Fig. 18, next to be determined is the effect of the flux on 8-mil silicon solar cells, the type being considered for use in the Jupiter probe application. No data are available directly relating 8-mil solar cell degradation with integrated proton flux. However, some empirical data do exist showing the effects of 1-MeV electron irradiation on thin silicon solar cells (Ref. 4). To obtain

*By E. Divita, "Definition of the Solar Flare Proton Radiation Environment in Interplanetary Space for the Jupiter Solar Electric Spacecraft Study," JPL internal document, Oct. 1967.

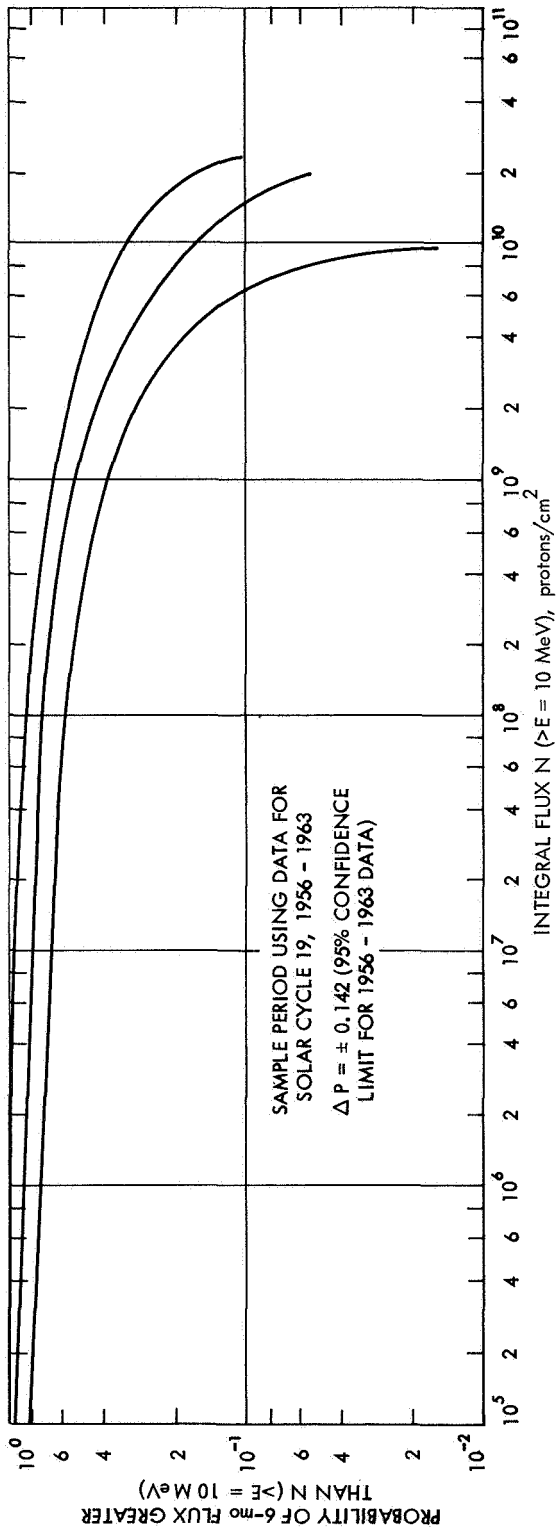

Fig. 18. Probability of flux occurrence

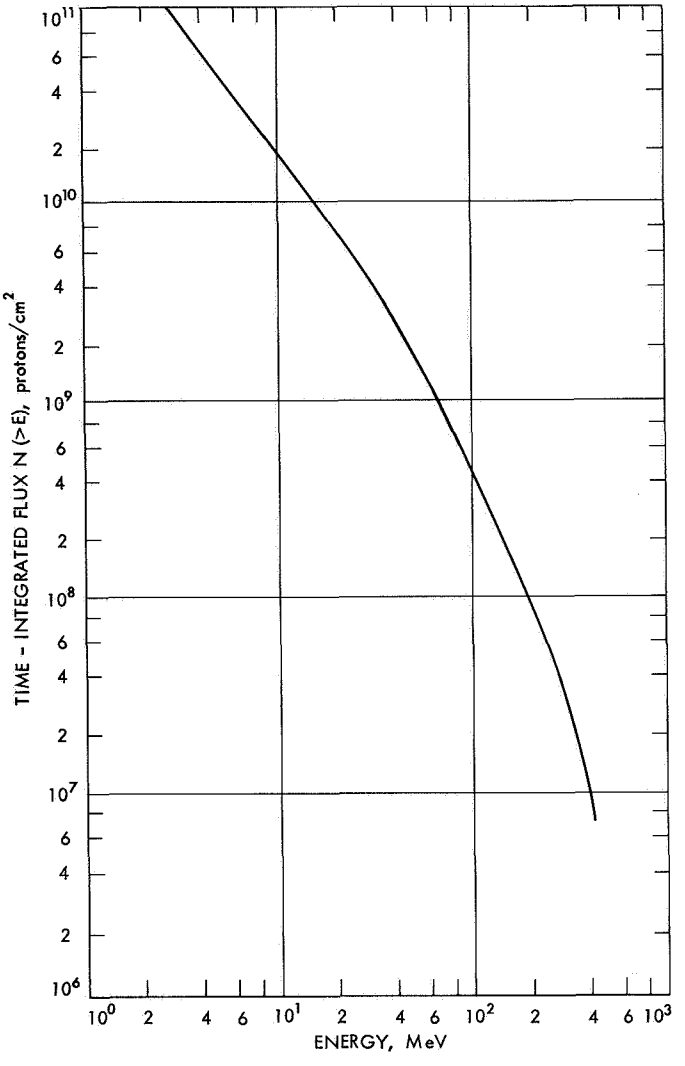

Fig. 19. Model solar flare energy spectrum

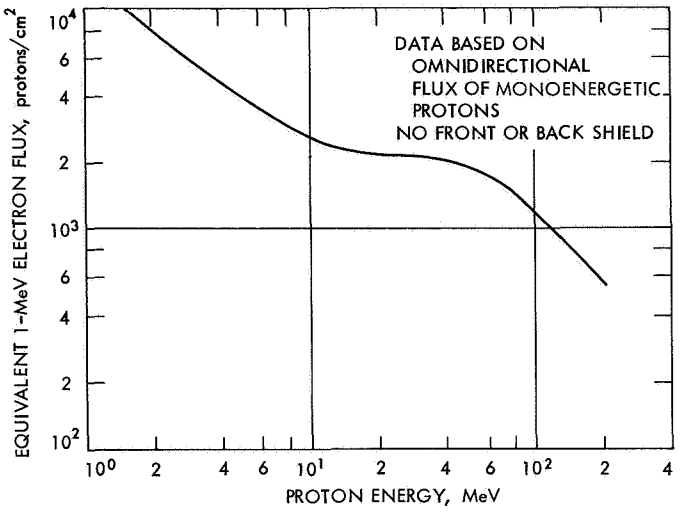

Fig. 20. Relation between proton energy and electron flux density

the amount of radiation damage caused by protons, the correlation of Rosenzweig (Ref. 3) is used.

Figure 20 shows the relation between proton energy and the equivalent 1-MeV electron flux density that will result in the same cell damage for 16-mil thick cells. For lack of better data, this relationship was assumed to hold for 8-mil thick cells. A significant observation from Fig. 20 is that the lower the energy of the protons the greater the damage. In addition, it should be remembered (refer to energy spectrum of protons in Fig. 19) that the greatest number of protons are at the lower energies. Thus, if the cutoff energy of the proton could be increased above the 3-MeV point by increasing shield thickness, a significant reduction in degradation could be achieved. Such an evaluation is discussed in the final section on trade-off analyses.

The curve of Fig. 20 is not exactly as defined by Rosenzweig. His correlation is based on an omnidirectional flux of monoenergetic protons striking a target with no front shield and infinite back shield; thus, only one-half of the protons could strike the target. Experiments conducted by Berman and Anspaugh of JPL* indicate that the curve of Rosenzweig should be reduced by a factor of 2 to correlate their data and other available experimental data. Based on their suggestion, Rosenzweig's correlation has been interpreted as the equivalent 1-MeV electron flux based on an omnidirectional flux of monoenergetic protons striking a target with no front shield and no back shield. This interpretation then corrects for the factor-of-2 discrepancy.

With the use of the probability data as given by Divita (curve for 6-mo mission in Fig. 18) and the correlation between proton flux and equivalent electron flux, curves of 1-MeV electron flux vs time are constructed for a family of probability values. These curves are given in Fig. 21 for the 95% confidence limits. Data to construct these curves exist only for 6-mo, 1-yr, and 2-yr missions. The curves, which have been extrapolated to predict the flux at smaller than a 6-mo time period, represent the probability (with 95% confidence) that the electron flux will not exceed the value shown at a specified time.

*P. Berman, "Comments on Memo on Effect of High-Energy Proton Radiation on P/N Solar Cells," JPL internal memo, Sept. 1966, and "Proton Irradiation Experiments—Harvard," JPL internal memo, July 1966.

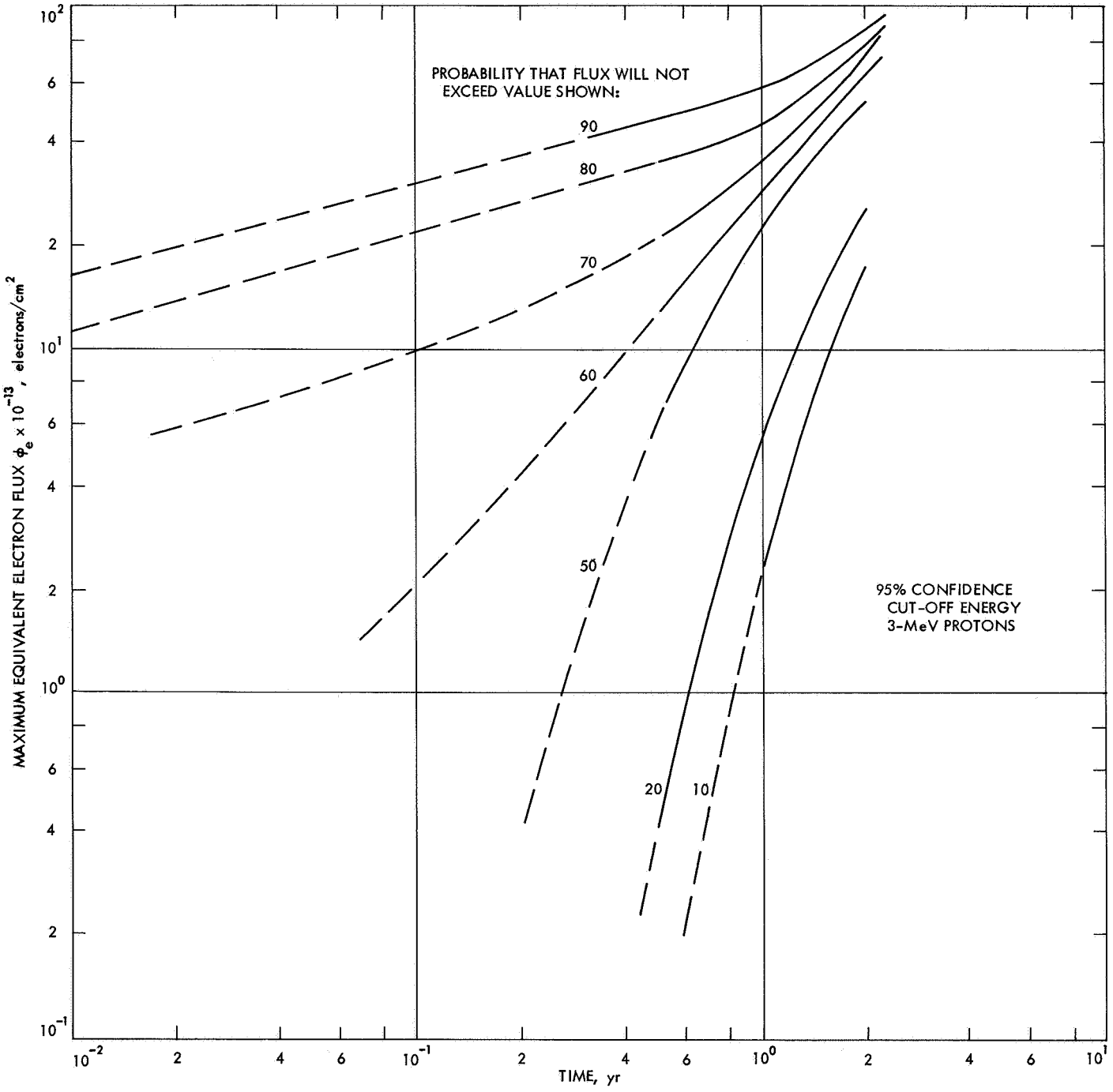

Fig. 21. Electron flux vs time at 1 AU

The curves of Fig. 21 are quite general and can be used to predict electron fluxes at 1 AU for any panel design that has a shield thickness to cut off protons at 3 MeV at both the front and back sides. For a case where the proton cutoff energy is different from 3 MeV, the curves of Fig. 22 may be used. Note that, if the proton cutoff energy can be increased to 4 MeV, the flux can be reduced by a factor of 2.

The curves of Fig. 21 can now be applied to the specific trajectory considered for the Jupiter mission. This trajectory (sun–probe distance vs time) is given in Fig. 23. If it is assumed that the proton flux intensity varies as

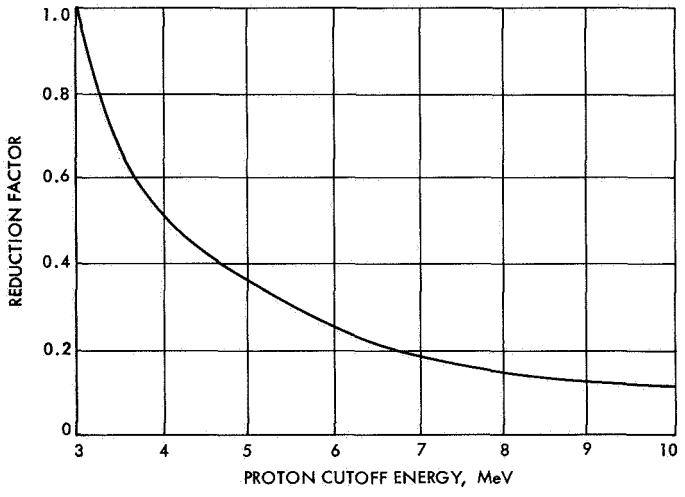

Fig. 22. Proton flux reduction factor vs cutoff energy

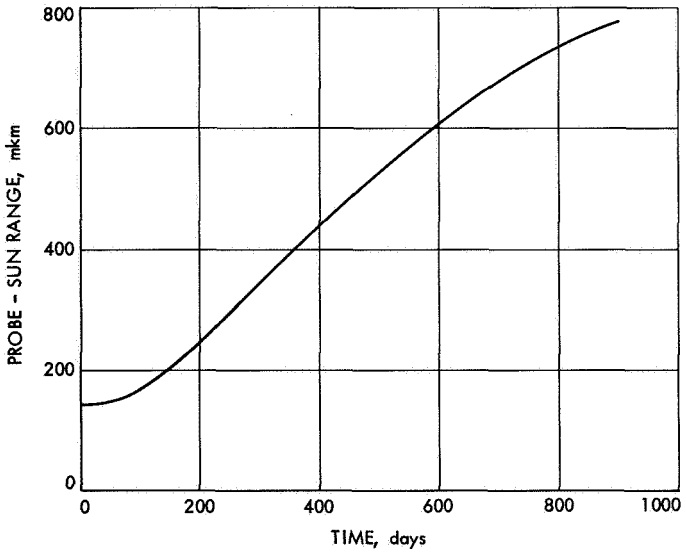

Fig. 23. Spacecraft trajectory

the inverse square of the sun–probe distance, the curves of Fig. 24 can be developed. In a 470-day time period (roughly the period during which power is required from the panels to operate the ion engines) the total integrated equivalent 1-MeV electron flux will be no greater than 5.2×10^{14} electrons/cm^2 with a probability of 90% (95% confidence). An empirical relationship relating total integrated electron flux and solar cell power reduction is given in Fig. 25 (Ref. 4). At an equivalent 1-MeV electron flux of 5.2×10^{14} electrons/cm^2 (90% probability in 470 days), the cell degradation is 14%. To summarize, it can be stated that there is a 90% probability with 95% confidence that the power will degrade less than 14% during the 470-day portion of the mission for which electrical power is required to the ion engines.

The problem of predicting the variation in output power during the mission is complicated somewhat when the uncertainties in the initial power are considered. Because of the uncertainties resulting from measurement limitations, it is possible that the initial output power of the panels may vary as much as $\pm 8\%$ about the estimated value (Fig. 17). If it is assumed that it is equally as likely to produce a panel that is 8% low in power as it is to produce one which is 8% high, the problem of predicting the output power at some time during the mission is treated in the following manner.

Assuming the variation of the initial power about an estimated mean is gaussian and the 3-σ limits (99.87%) of the gaussian are $\pm 8\%$ of the mean value, the problem is restated as follows. Assuming a panel whose initial power is given by a gaussian distribution about some mean power P_0, find the probability that, after some time t, the power will not reduce to a value below π. This problem is expressed by the integral*:

$$P_1(\pi, t) = \int_{z=-\infty}^{\infty} P_2\,[P(z)]\; P_3\,[\phi, t]\; dz$$

where

$P_2[P(z)]$ is the probability that initial power lies between z and $(z + dz)$

$P_3\,[\phi, t]$ is the probability that a flux ϕ will not reduce initial power $P(z)$ to less than π

$P(z)$ is the value of initial power at point z

$P(z = 0)$ is P_0, the mean value of initial power

*P. Wesseling, "On the Confidence Limits of Statistical Inferences Made From Solar Flare Observations," JPL internal document, Nov. 1967.

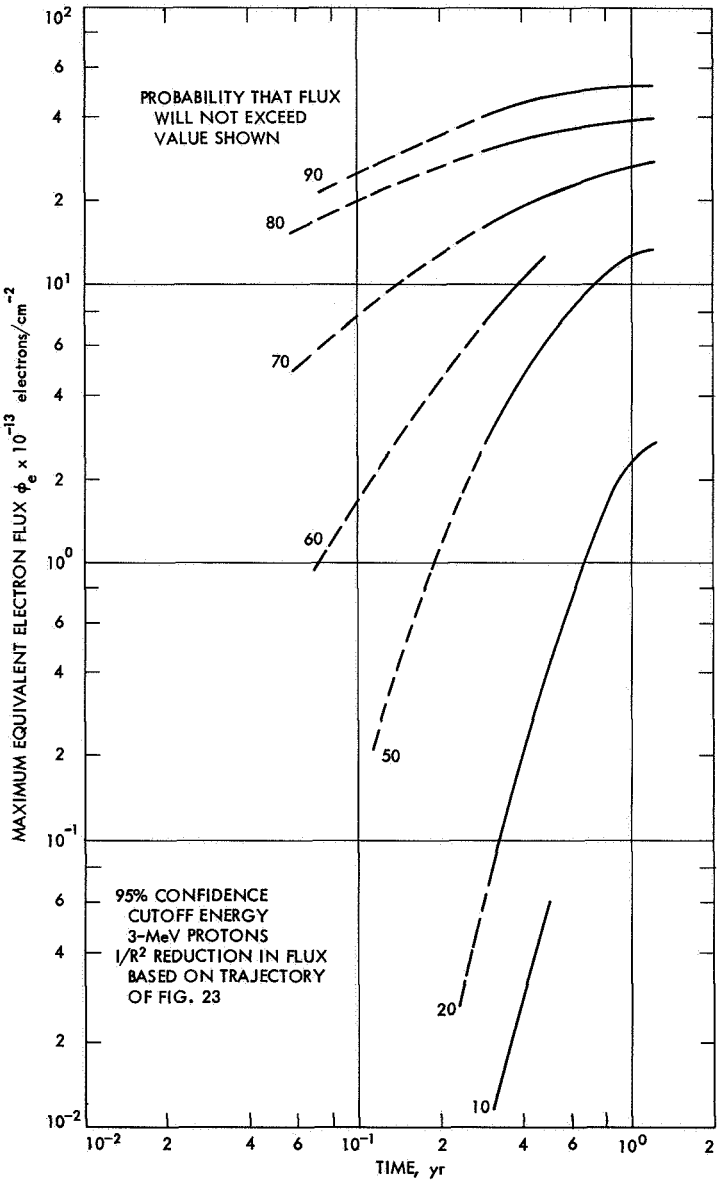

Fig. 24. Maximum equivalent electron flux vs time at 1 AU

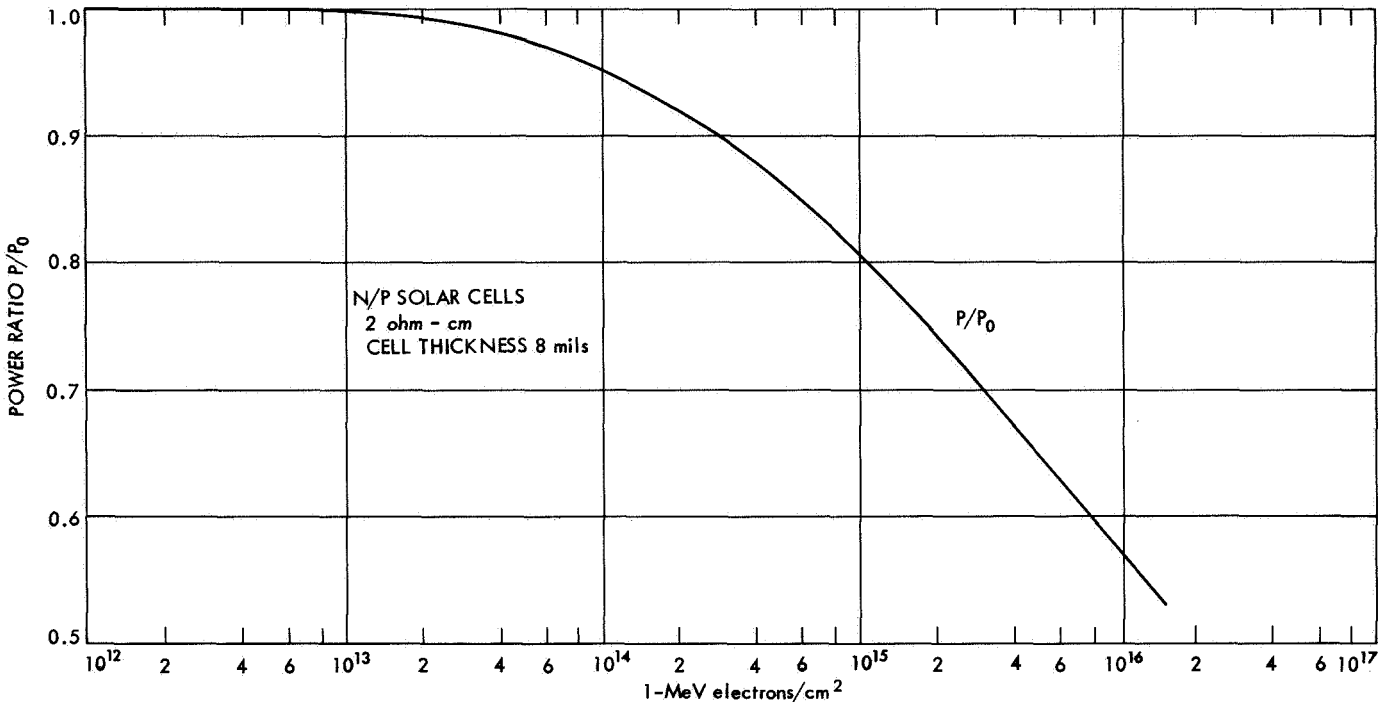

Fig. 25. Cell power vs integrated solar flare flux

Values for P_2 $[P(z)]$ can be obtained from standard gaussian tables. The probability P_3 $[\phi, t]$ is obtained by combining the data from Figs. 21 and 25.

The results of this analysis are presented in Figs. 26 and 27, which plot the probability of the power exceeding the value shown in the indicated mission time. As the assurance of meeting a given power increases, the magnitude of the power assured decreases. Thus, there is a 95% probability that the power, after 1 yr, will exceed 82% of the mean estimate of P_0, but only an 80% probability that it will exceed 87% of P_0 in the same time interval. The confidence limits on the values of probability given in Figs. 26 and 27 are all greater than 95% (the actual value was not computed). This condition arises from the fact that, in computing the probability $P_1(\pi, t)$, values for the probability $P_3[\phi, t]$ were all selected at the 95% confidence limit. It can be shown that, under these conditions, the confidence limits on the integral $P_1(\pi, t)$ will exceed the 95% level.

Two interesting observations can be made from the data. First, at the start of the mission ($t = 0$), the initial power does not begin at the mean value of P_0, but is somewhat below this value. The amount by which it is below the mean depends on the value of probability allotted to its occurrence. There is a greater probability of the guaranteed power being below the mean than there is of its being at or above the mean. This probability follows from the fact that the curves in Fig. 27 must be interpreted as giving the probability that the power will not be less than a given value. It should be remembered that a major assumption of the analysis was that the initial power uncertainty was gaussian about some mean value of P_0. Although the assumption of the gaussian distribution implies that there exists an equal probability for the power to lie on either side of the mean, when one interprets the curves as giving the probability that the power will not be less than a given value, the lower value from the gaussian must be chosen.

A second observation is that the decrease in power as a function of time is quite rapid over the first three months and remains essentially unchanged after six months. Two-thirds of the decrease in power from the mean occurs within the first month.

It is now pertinent to discuss the basic conclusion of the radiation study. As part of the mission analysis evaluation for the Jupiter study program, the photovoltaic power plant was sized to provide an 18% allowance for proton degradation and measurement contingencies. Based on the data of Fig. 27, there is a 95% probability (with greater than 95% confidence) that the power will not decrease below 82% of the mean estimate of P_0, (i.e., less than an 18% power reduction) any time during

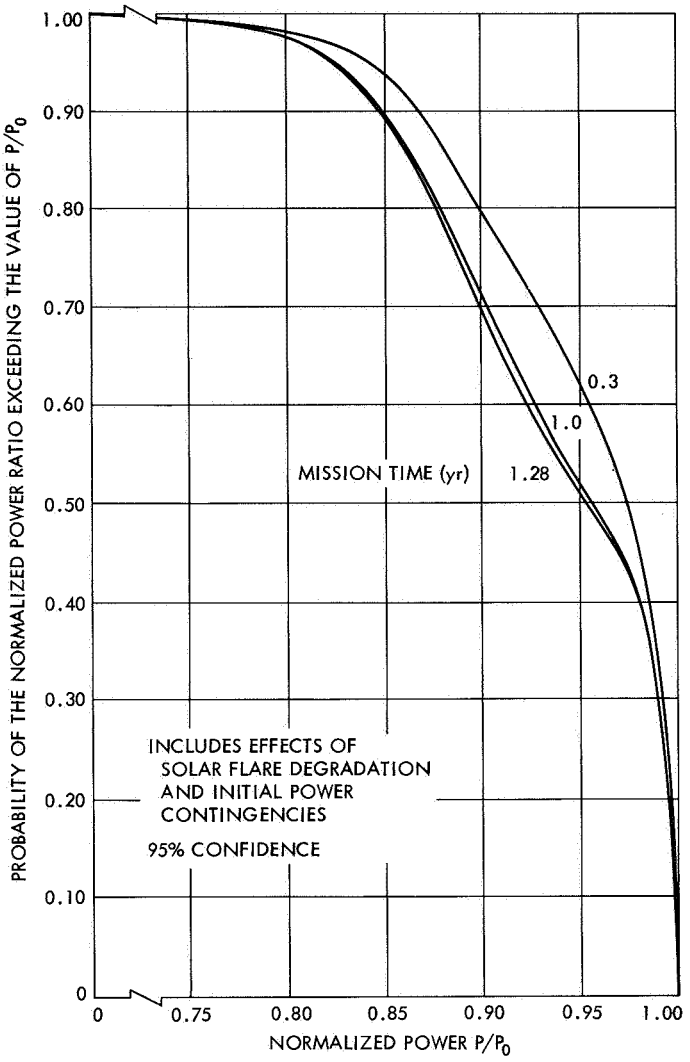

Fig. 26. Probability vs power

the mission. Thus, it is concluded that the power allowance provides for a high probability of mission success.

The particular solar cell design that has been selected for the Jupiter mission is considered optimum on the basis of 1969 state of the art technology. The use of a more radiation resistant design would not result in a lower weight power plant. To show that this assumption is valid, a trade-off analysis is given below. The performance of a cell is based on four factors:

(1) Type of cell (N/P or P/N).

(2) The base resistivity.

(3) Thickness of the cell.

(4) Thickness of radiation shield.

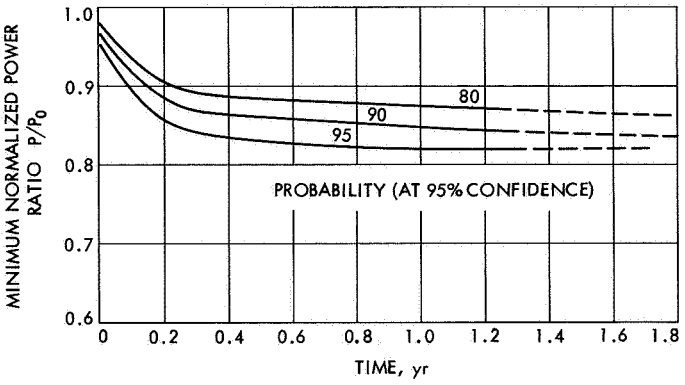

Fig. 27. Normalized power vs time

The present design is based on the N/P type of cell. From experience those cells have been found to degrade considerably less than the previously used P/N cells. The base resistivity of a cell can have a significant effect on its performance: the higher the resistivity, the lower the relative output of the cell. However, it has been found that high-resistivity base cells are less susceptible to radiation damage. Figure 28 (Ref. 4) indicates the variations of cell power vs the amount of irradiation. For a given cell thickness, the 10-ohm-cm cell is considerably more stable; however, the initial power is lower. Not until the electron flux exceeds 5×10^{15} electrons/cm^2 does the higher resistivity cell show superior performance. Since the maximum flux expected during the Jupiter mission is below 1×10^{15} electrons/cm^2, the lower resistivity base material is preferred. A nominal 1-ohm-cm cell has been selected for the Jupiter mission study.

The conversion efficiency of a cell increases as its thickness increases; however, there is also a linear increase in weight as a result. Although the power of the thicker cells is initially larger, at a flux in excess of 5×10^{14} electrons/cm^2, there is no difference in power between a 6-mil cell and a 12-mil cell. This equal flux-power level indicates that the thicker cells are more susceptible to radiation damage. Since the weight of the resultant panel is lower for the thinner cells, a thin cell design is preferable. An 8-mil cell thickness was selected for the Jupiter mission study as representing the thinnest cell that is presently within the 1969 state of the art technology.

A considerable reduction in cell degradation can be achieved by increasing the thickness of the top-cover glass and substrate backing, thus decreasing the number of low-energy protons reaching the sensitive area of the cell. The lower the proton energy, the greater damage it can produce. However, an increase in shield thickness

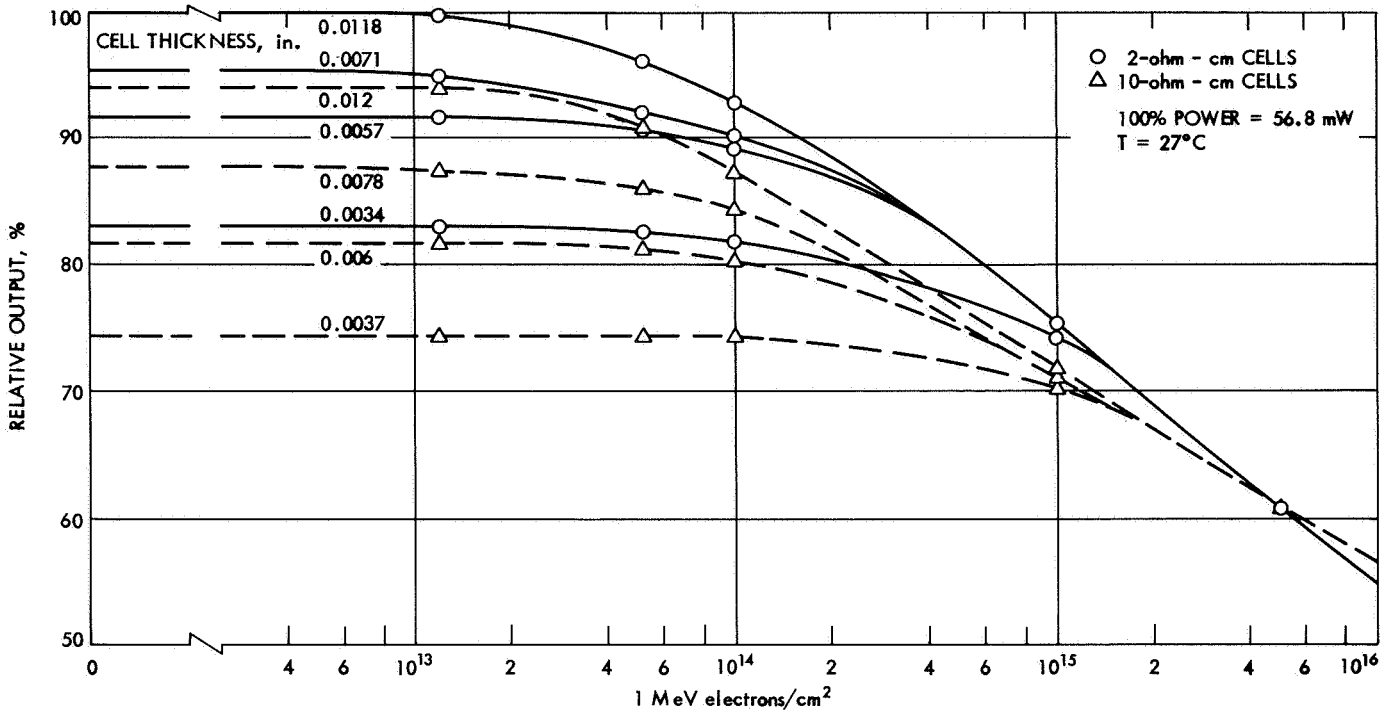

Fig. 28. Maximum power vs irradiation (reprinted from Ref. 4 by permission of J. Martin and ASME)

will result in an increase in panel weight. To determine the optimum shield thickness, a trade-off analysis was performed.

The solar array component weight breakdown in Table 11 assumes 8-mil cells with a 3-mil cover glass and a substrate composed of 2 mils of RTV adhesive and 3 mils of a fiberglass mesh covering approximately 38% of the cell area. The variation in the above weights is determined as a function of an increase in cover glass and substrate thickness, as given in Table 12. It was assumed that a 10% increase in cell stack weight resulted in a 10% increase in both the structure and mechanisms. The values for the specific power of the panel are based on a value of 9.5 W/ft^2.

Table 12. Weight variation as a function of cover glass and substrate thickness

Glass and substrate, thickness, in.	Weight, lb/ft^2	Specific power, W/lb
0.003	0.455	20.8
0.004	0.526	18.0
0.005	0.581	16.3
0.007	0.705	13.5
0.010	1.011	9.4

The above data can now be used to perform a trade-off analysis for selecting the optimum thickness of glass and substrate. Table 13 presents the results of this study. In the first column, the thickness of the cover glass and substrate is given. The second column gives the effective cutoff energy of the protons for the given shield thickness. The range of protons is obtained from the data shown in Fig. 29 (Ref. 5). In the third column, the amount of cell power degradation that can be expected during a 470-day mission is given. The data in this column are based on receiving a 1-MeV electron equivalent flux of 5.2×10^{14} electrons/cm^2 during the mission with a 3-mil shield at both front and back. The decrease in the amount of degradation with increase in shield thickness is obtained by the use of Figs. 22 and 25. The fourth column presents the power requirements of the solar panel to assure a 12,000-W capability. As the shield thickness increases, the amount of degradation due to solar protons also decreases, thus requiring a smaller initial power source. However, the disadvantage of the thicker shields is shown in the fifth column. As shield thickness increases, the specific power (W/lb) of the panel decreases. The net weight effect of an increase in shield thickness is shown in the last column and given as a curve in Fig. 30.

It is concluded that the smallest shield thickness results in the optimum panel performance based on a

Table 13. Selection of optimum cover glass and substrate thickness

Glass and substrate thickness, in.	Cutoff energy of protons, MeV	Power degradation, %	Initial power requirements, W	Specific power, W/lb	Weight, lb
0.003	3.0	14.0	14,000	20.8	670
0.004	3.55	11.1	13,550	18.0	750
0.005	4.05	9.6	13,350	16.3	820
0.007	5.0	7.8	13,050	13.5	965
0.010	6.2	6.0	12,800	9.4	1360

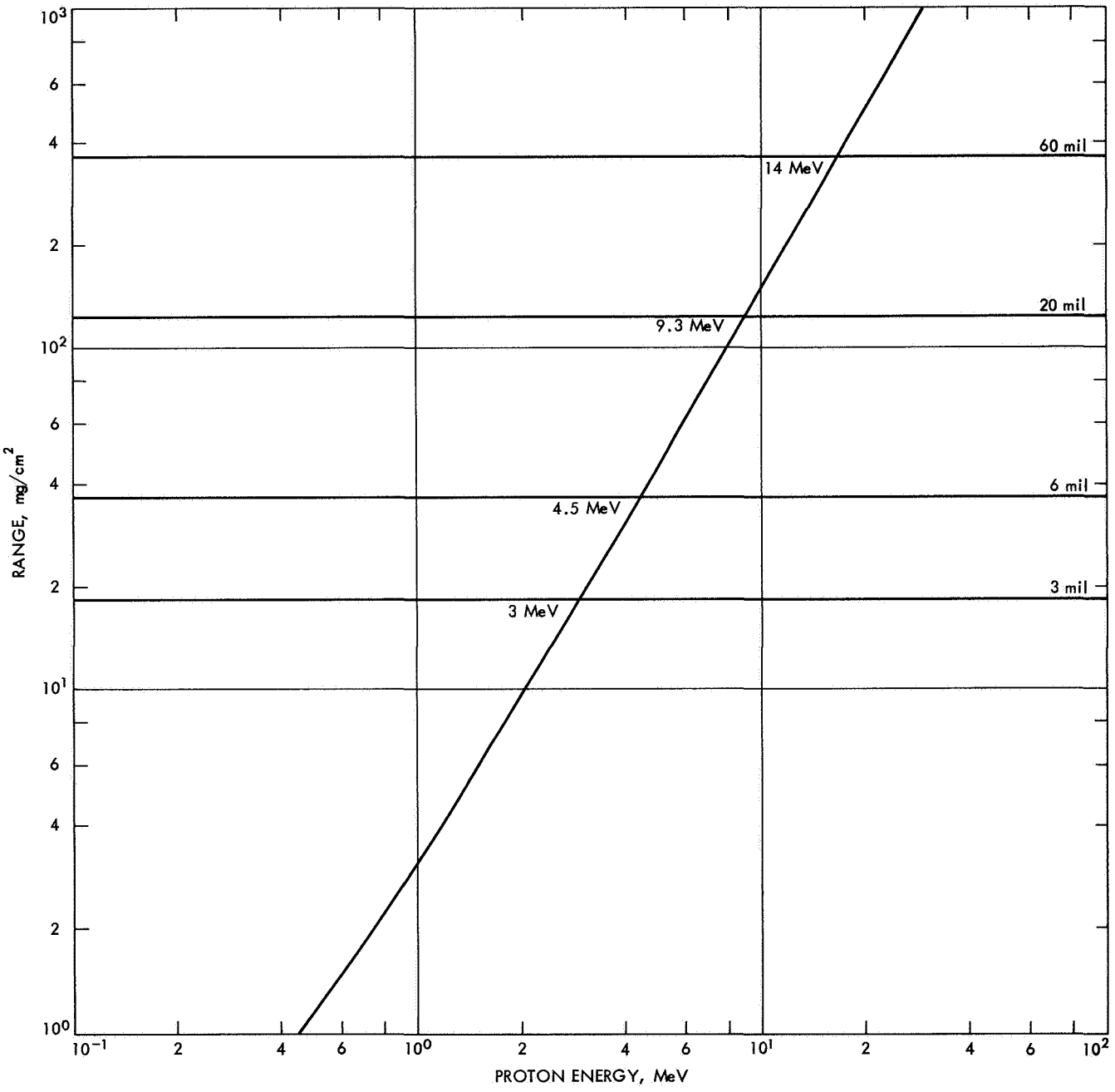

Fig. 29. Range vs proton energy (reprinted from Ref. 5 by permission of V. Linnenbom and NRL)

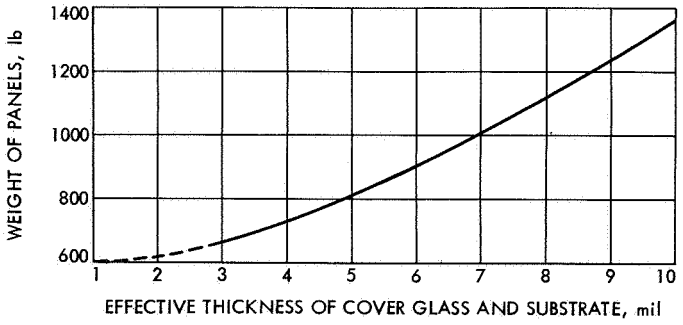

Fig. 30. Weight of solar panels vs proton shield thickness

minimum weight criterion. It has also been determined that, even if one assumes no weight increase in structure and mechanism with increase in cell weight, the same conclusions can be reached. The variation of weight with thickness is, however, considerably reduced.

b. Micrometeoroid damage. In this section, estimates of the effects of the micrometeoroid environment upon the solar array are made. The largest single unknown in the prediction of solar panel degradation is the exact nature of the micrometeoroid environment. Of the many models hypothesized in the literature, a conservative estimate* is chosen for this evaluation. A summary of the environment is given in Table 14.

The approach to the problem is to use the best available data to predict the degradation of the solar array, since knowledge of the micrometeoroid environment and penetration phenomena at high velocities is limited. In the interspace environment (1–1.5 AU), the best estimate is made by use of the data obtained on the *Mariner IV* flight. The *Mariner* program revealed that most of the panel degradation was caused by particulate radiation and that only about 3% of the total degradation received during a 200-day period was caused by other considerations (namely, ultraviolet radiation, micrometeoroid effects, temperature, and vacuum). For this study, a conservative estimate of 1% linear degradation over a 200-day period by micrometeoroids has been made.

In the asteroid region (1.5–5.2 AU), since the asteroids are in a heliocentric orbit, the solar array is not hit directly by asteroids because the panels are oriented toward the sun. The range velocity of the spacecraft into the asteroid flux, however, can cause impact of the solar array by asteroids. As shown on Fig. 31, an approximate velocity of the spacecraft relative to the asteroid of 10 km/s can be considered as a conservative estimate for most of the flight.

The basic assumption made to evaluate solar cell degradation is that the power loss is proportional to the

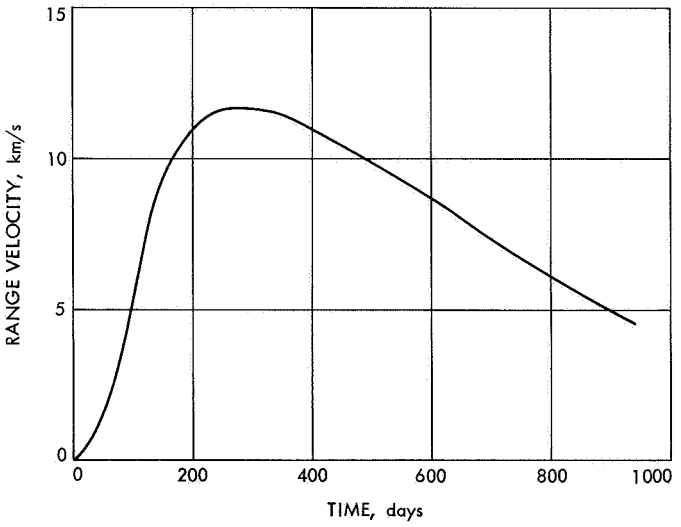

Fig. 31. Spacecraft velocity within the asteroid belt vs time

*"Jupiter Flyby Application," JPL internal document, May 1966.

Table 14. Micrometeorite environment

Zone	Direction	Distance, AU	Particle	Density, g/cc	Velocity, km/s	Flux, particles/m^2-s, mass, g
Earth dust cloud	Earth orbiter	1.0	Cometary	0.4	0–15	$10^{-17}M^{-1.7}$
Interspace	Omnidirectional	1.0–1.5	Cometary	0.4	40	$10^{-13.3}M^{-1.0}$
Asteroid belt	Heliocentric	1.5–5.2	Meteoritic	3.4	10–20	$10^{-10}M^{-0.77}$
Jupiter dust	Jupiter orbit	5.2	Cometary	0.4	10–60	$10^{-15}M^{-1.7}$ to $10^{-4}M^{-1.7}$

loss in area caused by asteroid impact. The probability that an asteroid would hit an electrical lead and cause an open circuit is also treated. However, impacts that would cause a short circuit of the cell appear to be negligible.

For a spherical asteroid, the mass-projected area relation is

$$m = 2.5\,A^{3/2}$$

which results in

$$\phi = 0.5 \times 10^{-10}\,A^{-1.15}$$

where ϕ is the flux in particles/m^2-s, and A is the projected area of an asteroid in cm^2. The ratio of degraded area to original area caused by asteroids greater than 1×10^{-12} g (the smallest particle believed to be capable of remaining in a captive orbit about the sun) during the flight through the asteroid belt is evaluated by the following integral:

$$\left(\int_{A_1}^{\infty} -A\,\frac{d\phi}{dA}\,dA\right)\tau = 0.00004$$

where A_1 is the projected area corresponding to 1×10^{-12} g, and τ is the total time of exposure to the micrometeoroid flux (about 700 days of the 900-day mission). It is readily apparent that the total area affected by the micrometeoroid is rather negligible. Although during the 700-day mission more than 10^9 impacts are made, the size of the particles making these impacts is extremely small.

The only other mode by which damage is considered possible is an impact producing an open circuit in a cell. For this result to happen, the electrical lead of a cell must be severed. To evaluate this problem, it is necessary to consider the following points.

(1) Impact of a meteoroid can occur only on the back surface of the solar array, since the panels are moving into the asteroid flux. Thus, the substrate and thickness of the cell act as a shield against impact by the very small particles. Since the small particles predominate, this shielding effectively prevents damage from most of the particles.

(2) Only a very small portion of the total panel area (less than 0.2%) is vulnerable to open-circuit damage.

The minimum asteroid mass sufficient to penetrate the cell and cause an open circuit was calculated to be 4.6×10^{-9} g from Refs. 6–8:

$$P = (d)k(0.6)K_0^{2/3} \ln\left(1 + K_0^{2/3}\,B/4\right)$$

where

P = penetration depth

d = diameter of the particle

k = factor of 1.5 used to convert semi-infinite media penetration to plate penetration

$K_0 = \dfrac{\rho_P}{t}$

$B = \dfrac{\rho_t V^2}{H_t}$

ρ_P = projectile density

ρ_t = target density

V = velocity of projectile relative to target

H_t = Brinell hardness of target

This relationship, which was derived from experiments using other target materials, is assumed to be valid for silicon. The experiments do include velocities in the range of interest, namely 10 km/s.

It has been estimated that approximately 10^6 collisions between panels and particles of mass greater than 4.6×10^{-9} g will occur during the time the spacecraft resides within the asteroid belt ($\sim$ 700 days). If only 0.2% of the area is vulnerable to open-circuit damage and the particles are evenly distributed across all cells (i.e., the asteroid is equally likely to hit any portion of the panel), less than 2000 cells will be affected. Since the panels will consist of more than 300,000 cells, an estimate of 1% power degradation caused by asteroids with mass greater than 4.6×10^{-9} g during a 700-day period is obtained.

In summary, the overall panel degradation as a result of micrometeoroid damage occurring between earth (1 AU) and Jupiter (5.2 AU) is estimated conservatively to be less than 2%. The estimated time history of occurrence is given in Fig. 32.

c. Jovian electron field. Preliminary estimates of the magnitude of the magnetically trapped electron radiation belt surrounding the planet Jupiter have been made in

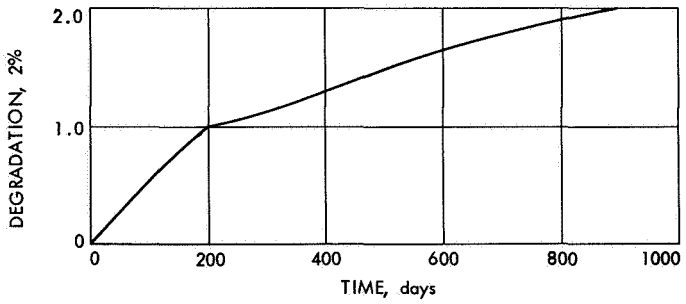

Fig. 32. Power degradation due to micrometeoroids

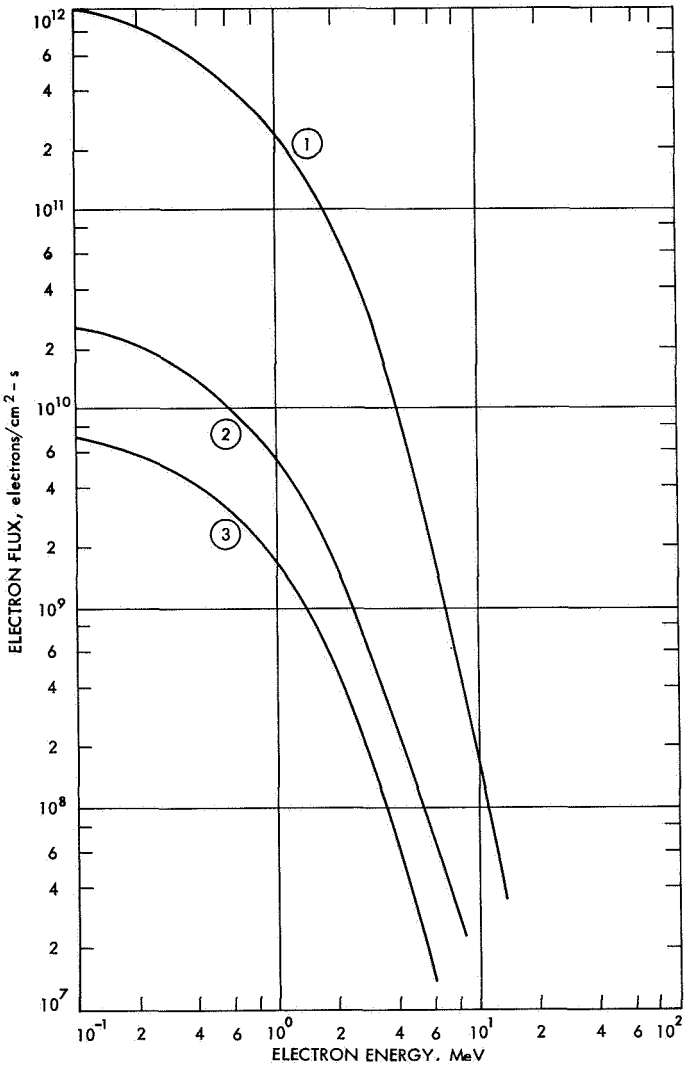

Fig. 33. Jovian radiation belt electron flux

detail*. Several models with absolute values varying by more than 2 orders of magnitude are presented in Fig. 33. The curves of Fig. 33 represent the spectral

*"Jupiter Flyby Application," JPL internal document, May 1966.

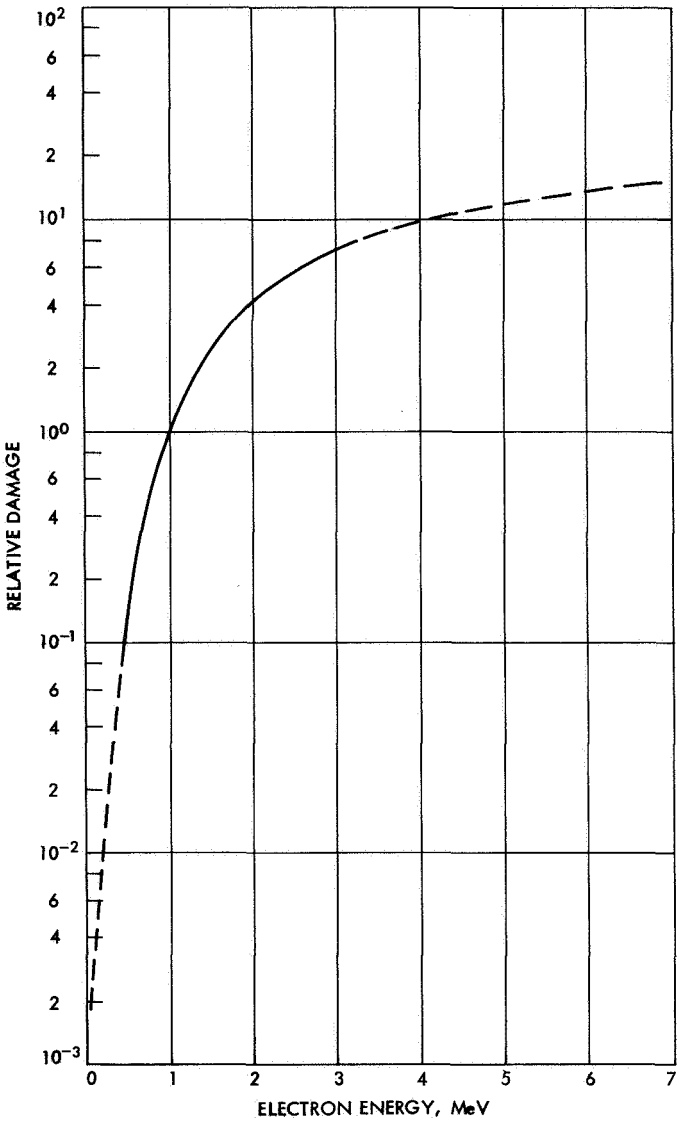

Fig. 34. Effect of electron energy on damage rate

energy distribution of the electron flux. The magnitude of flux as given in curve No. 2 is considered the most reasonable; curve No. 1 is considered an upper limit.

In the previous section discussing the radiation effects of proton flares on solar cells, a relationship between power degradation and equivalent electron flux was presented. It was necessary, therefore, to convert the data in Fig. 33 to equivalent 1 MeV electrons. The data of Ref. 3 were used for this purpose. It had been found that the relative damage caused by electrons varied considerably with the electron energy (Fig. 34). With the use of a computer program, the spectral distribution of Fig. 33 data was weighted by the relative damage rate

of electrons, and an effective total electron flux was determined. For the worst case (curve No. 1 of Fig. 33), the magnitude of the flux was found to be 0.99×10^{12} equivalent 1 MeV electrons/cm²-s. The values for curves Nos. 2 and 3 were found to be 0.24×10^{11} and 0.48×10^{10} 1 MeV electrons/cm²-s.

Having established the magnitude of the effective 1-MeV flux, it is next necessary to determine the variation of this flux with distance. The previous data suggest that the position of the maximum flux in Jupiter's electron belt is at 3 planet radii. Examination of the variation of electron flux with distance at the earth's outer belt (note that there are two electron belts at earth) reveals a reasonable correlation (Ref. 9) to the magnetic field strength (Fig. 35). It is found that the flux on either side of the peak varies closely with the square of the magnetic field (inversely toward the earth and directly away from the earth).

It has been assumed that a similar correlation exists for the electron field about Jupiter. For conservatism, the flux is assumed to be constant for radii less than 3 and varies as the square of the magnetic field at locations greater than 3 radii. The trajectory of the spacecraft is such that the spacecraft never gets closer than 2.4 radii.

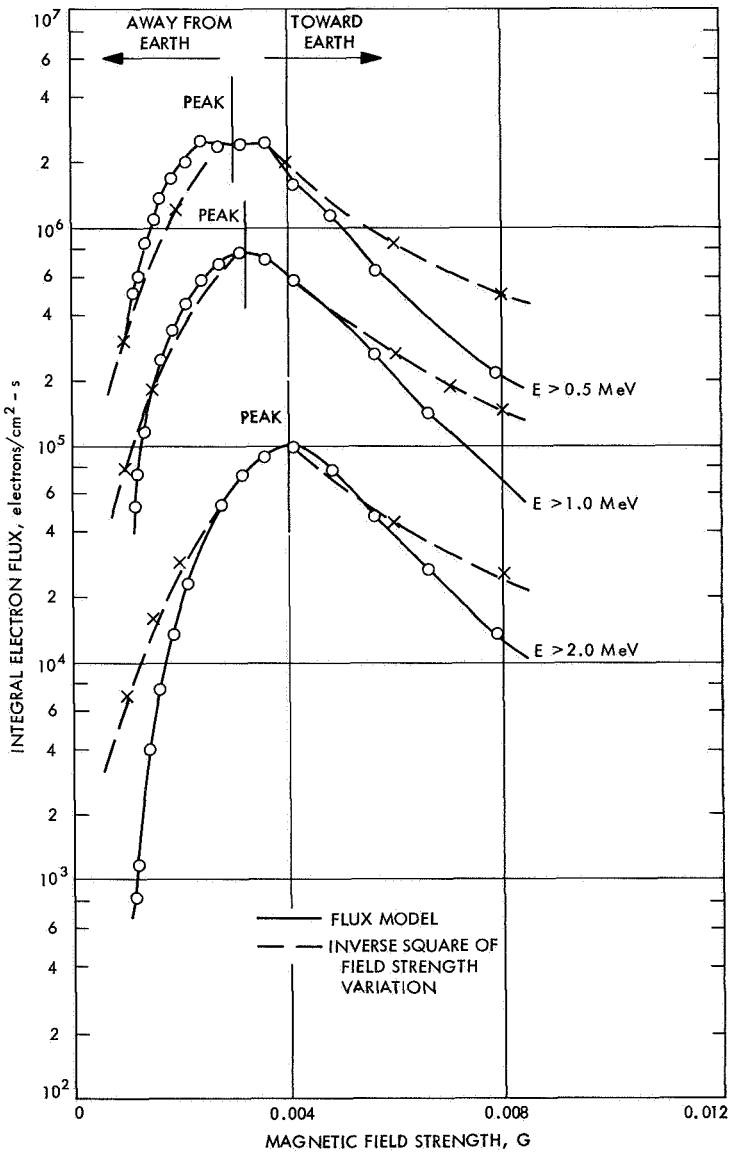

Fig. 35. Electron flux vs magnetic field strength

Data* for the variation of magnetic strength with radius are shown in Fig. 36. At about 9 planet radii, the magnetic field is only 5% of the value at 3 planet radii, the assumed maximum flux point. Therefore, on the basis of the relationship of flux to the square of the magnetic field, it is apparent that the electron flux at this point is nearly 3 orders of magnitude below the value at the peak point.

The total electron flux received by the solar panels as the spacecraft encounters Jupiter can be determined by integrating the flux rate with respect to time. This determination was accomplished numerically by the use of a digital computer program. Input to the computer included:

(1) The magnitude of the effective 1-MeV flux at 3 Jupiter planet radii.

(2) The functional relationship for the variation of flux with magnetic field strength.

(3) The variation of magnetic field with distance.

(4) The variation of distance with time.

In this analysis, three values for the magnitude of the effective 1-MeV flux at 3 Jupiter radii were utilized. The values ranged from 0.99×10^{12} down to 0.48×10^{10} electrons/cm²-s. The variation of distance with time (i.e., the encounter trajectory) is given in Fig. 37.

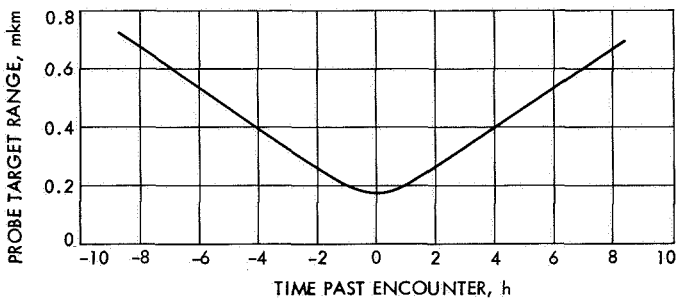

Fig. 37. Jupiter encounter trajectory

The results of this integration are given for the worst-case flux in Fig. 38, which shows the variation of the integrated flux with time. It should be recalled that previous irradiation as a result of solar flares amounted to an integrated flux of 5×10^{14} equivalent 1 MeV electrons/cm². Thus, no significant additional damage will occur to the panel until the integrated flux exceeds this value. According to Fig. 38, this event does not occur until about 2½ h prior to encounter. Beyond this time, the flux continues to increase rapidly (by an order of magnitude) and then levels off after 2½ h past encounter. The maximum integrated flux at completion of the encounter phase is 1.45×10^{16} equivalent 1 MeV electrons/cm². Reference to Fig. 25 indicates that this flux will produce a total solar panel power degradation of 47%.

The above, of course, is all based on the assumption that the flux rate is 0.99×10^{12} electrons/cm²-s (the maximum expected). The lower values of flux corresponding to 0.24×10^{11} and 0.48×10^{10} electrons/cm²-s result in integrated fluxes, which are 1–2 orders of magnitude lower. Such a flux will not cause significant damage beyond that produced previously by the solar flare flux.

B. Auxiliary Electrical Power Subsystem

The auxiliary electrical power subsystem is composed of a power source logic circuit for selection of energy source (e.g., solar panels, batteries, or external power), two secondary batteries for energy storage, a battery

*"Jupiter Flyby Application," JPL internal document, May 1966.

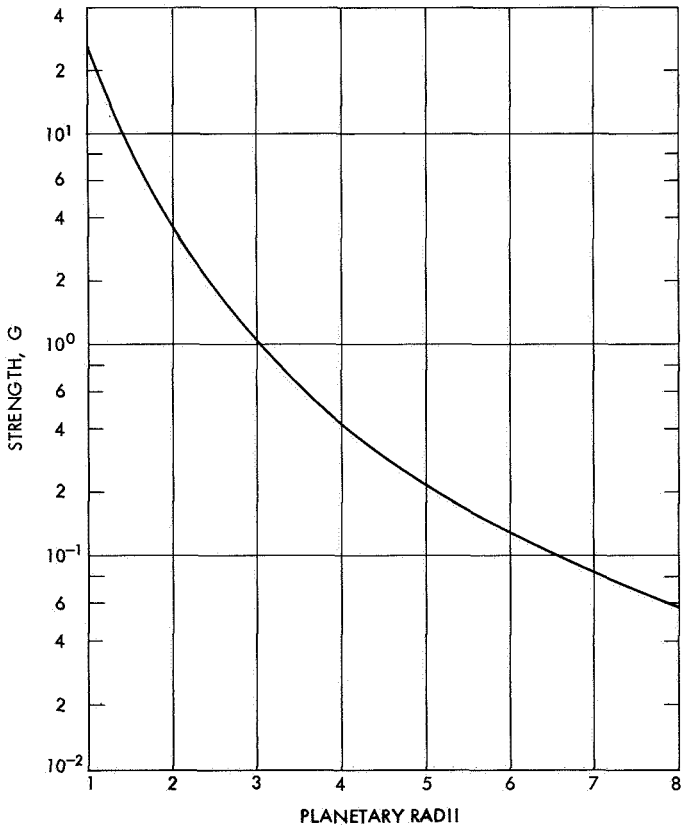

Fig. 36. Estimate of the Jupiter magnetic flux

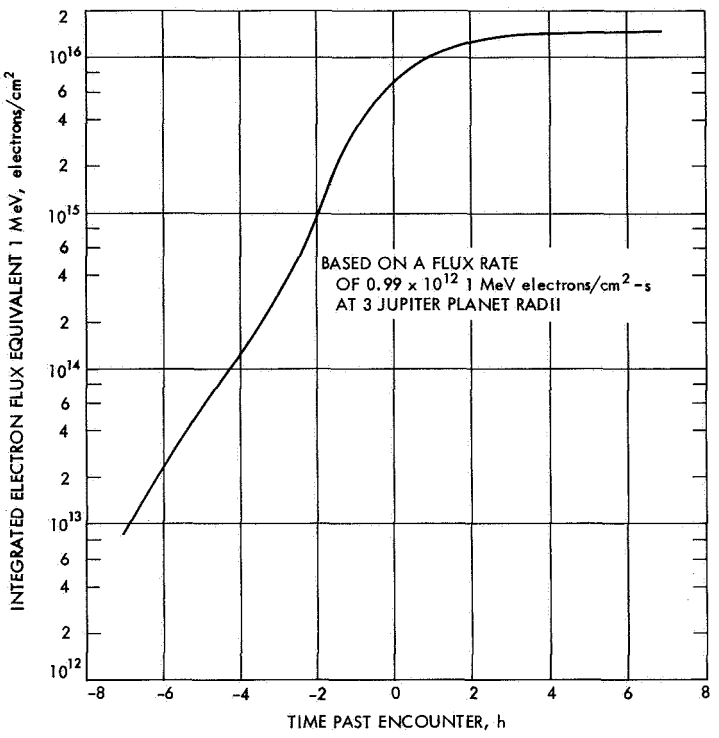

Fig. 38. Integrated electron flux vs time through Jovian electron belt

charger, a battery booster circuit for share mode, redundant buck-boost regulators, redundant 2.4-kHz inverters for science and engineering loads, 400-Hz inverters for attitude control and science, and a power distribution and logic system. A functional block diagram for the overall electrical power subsystem, including the engine power conditioning and load matching equipment, is shown in Fig. 39. A weight and volume breakdown is given in Table 15.

Table 15. Weight and volume breakdown of auxiliary power subsystem

Item	Weight, lb	Volume, in³
Main battery (including chassis)	20.0	460
Auxiliary battery (including chassis)	20.0	460
Battery charger/booster	2.3	65
Main booster regulator	6.2	123
Standby booster regulator	6.2	123
Power source logic	10.0	512
Power distribution and switching	4.0	127
Main 2.4-kHz inverter	3.0	93
Standby 2.4-kHz inverter	3.0	93
Single- and three-phase 400-Hz inverter	3.8	120
Total	78.5	2176

The auxiliary electrical power subsystem, based on the *Mariner* Mars 1969 design, is designed to supply 250 W of continuous power to operate the spacecraft engineering and science loads. In addition, the subsystem provides switching and control functions for management and distribution of power to spacecraft loads. The overall subsystem regulating and conversion efficiency will be 75%.

As shown in the functional block diagram (Fig. 39), power is derived from either four photovoltaic solar panels or rechargeable (secondary) batteries. Power from the battery and/or solar panels is converted and distributed in the following forms:

(1) 2.4-kHz single-phase square-wave power for the engineering and science subsystems.

(2) 400-Hz three-phase quasi-square wave power for the attitude control subsystem.

(3) 400-Hz single-phase square-wave power for the engineering and science subsystems.

(4) Unregulated dc power to the communication subsystem for the RF power amplifier converter.

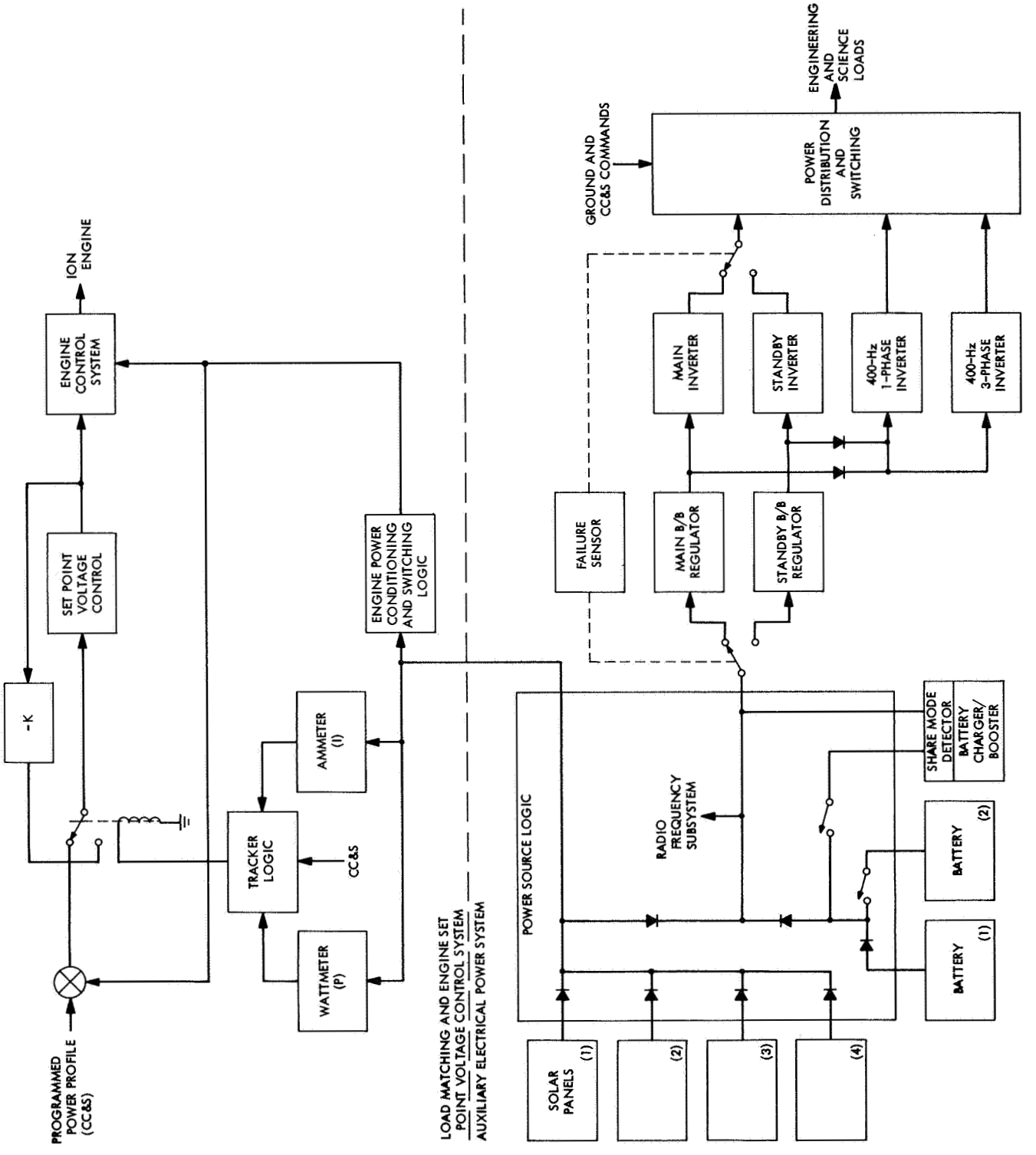

Fig. 39. Functional block diagram of auxiliary power subsystem

Aside from supplying this power, the auxiliary power subsystem provides a central timing function for the entire spacecraft by utilizing a precision crystal oscillator in the 2.4-kHz inverters. Each module of the auxiliary electrical power system is briefly described below.

1. Power source logic. The power source logic (PSL) provides the circuits for selecting the energy source: solar panels, batteries, or external power. In addition, it contains the umbilical connector, motor driven transfer switch, telemetry transducers, and isolation diodes.

2. Energy storage system. During periods when the spacecraft is not sun oriented, spacecraft power is obtained from the energy storage system. The energy storage system will consist of two 18-cell, sealed silver-zinc alkaline batteries. The normal capacity of each battery will be 22 A-h (600 Wh). Maximum charge and discharge currents are 1 and 15 A, respectively. Voltage regulation will be from 25.8 V, when the battery is discharged under load, to 35.2 V at the end of the 1-A charge.

The battery operation approach is to use the first (main) battery during launch, acquisition, and up to 450–500 days thereafter. The main battery was sized to accommodate a 62% depth of discharge under worst-case conditions (45% under normal conditions). The battery will be kept fully charged during periods of nonoperation.

The second (auxiliary) battery will be temperature controlled at 0°F during the flight and activated after 500–700 days. At this time, the battery will be heated to an operating temperature of 75°F.

The mode of operation of the energy storage system is determined by the auxiliary battery control (ABC) circuit. The three modes of operation, shown in Fig. 40, are: main battery mode, auxiliary battery mode, and high-current mode. In the main battery mode, only the main battery is connected to the unregulated bus, and is the normal configuration. In the auxiliary battery mode, the main battery is connected to the unregulated bus through a series diode while the auxiliary battery is directly connected. In the high-current mode, both the main and auxiliary batteries are connected to the unregulated bus without the series diode.

The battery modes are changed by ground commands, except that the ABC automatically switches to auxiliary battery mode from main battery mode in case of main battery failure. This automatic function can be disabled by ground command.

3. Battery charger booster module. The battery charger booster module contains three separate circuits that provide three distinct functions. A functional block diagram of this module is shown in Fig. 41.

a. Battery charge regulator. The battery charger is a constant voltage, current limited, series-dissipative type

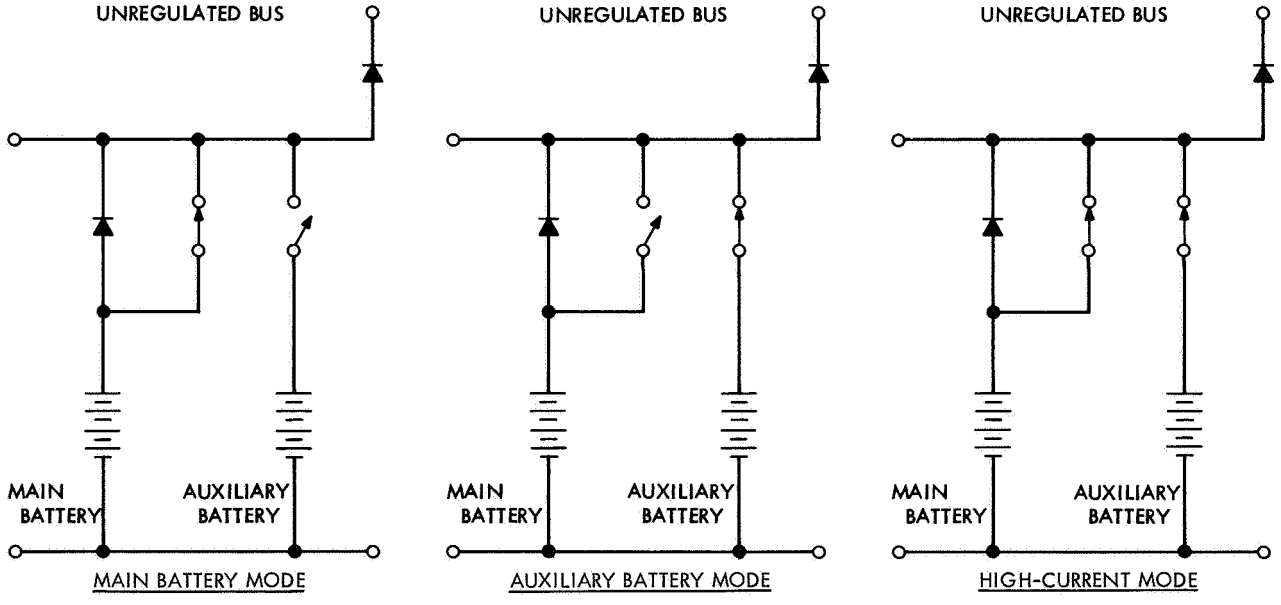

Fig. 40. Auxiliary battery control operational modes

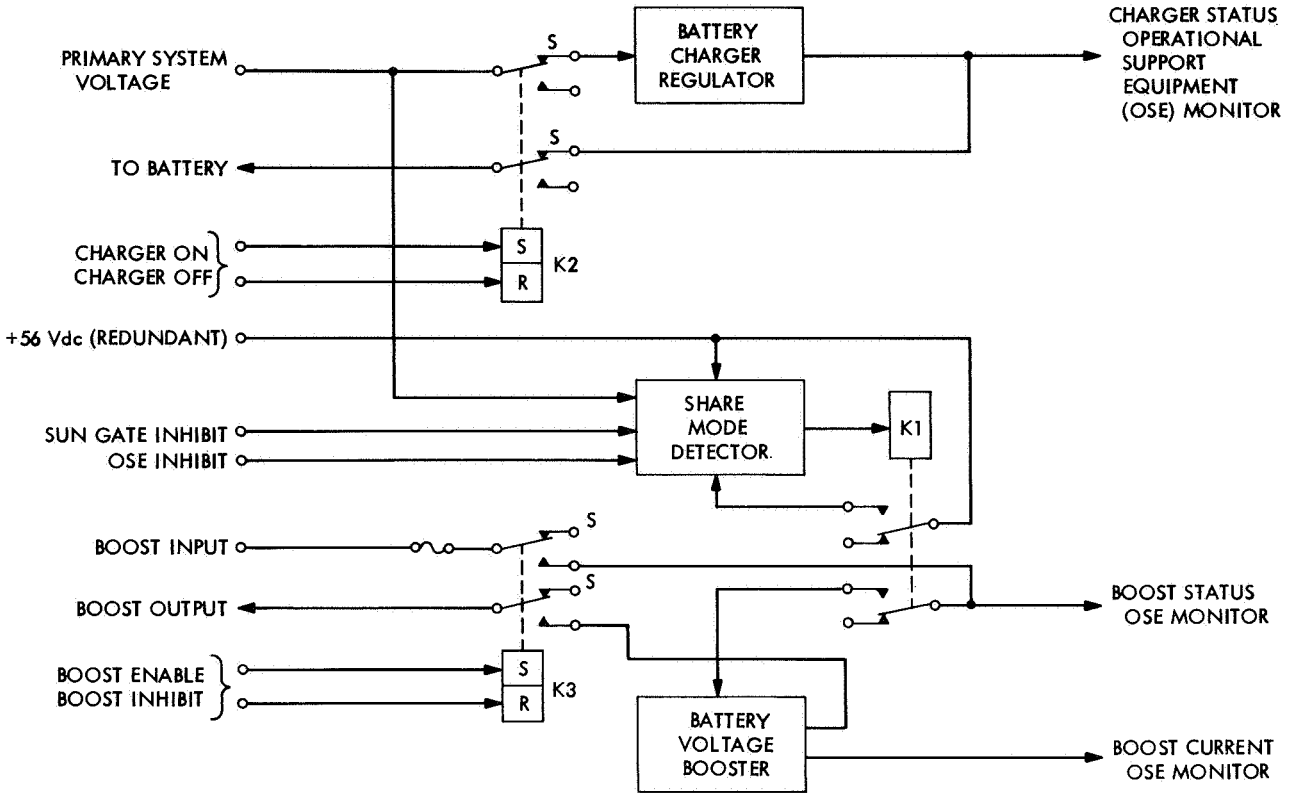

Fig. 41. Battery charger booster module

regulator that provides current to charge the battery when the solar panels are oriented to the sun. The maximum charge current to the battery will be less than 1A, and will be a function of the dc power bus and battery terminal potentials.

b. Battery voltage booster. In the event of a solar panel/battery share condition, and if the solar panels are capable of supporting the load at a voltage above the maximum power point voltage, a boost mode circuit is provided that will instantaneously provide sufficient power in the form of voltage pulses to allow the required operating voltage transition. In this condition with the battery undesirably contributing power to support the spacecraft load, a share mode detector will cause a relay to connect battery power to the boost converter circuit. This circuit will provide 44-V dc pulses at discrete intervals to the dc power bus to force the array-operating point out of the share mode with the battery.

c. Share mode detector. The share mode detector circuit will sense the potential of the dc power unregulated bus and will provide a signal to control a relay that automatically connects or disconnects input power to the boost converter circuit. The share mode detector logic is a function of dc power bus potential and sun orientation (signal from attitude control sun gate).

4. Buck/boost regulator. The voltage-regulating elements of the auxiliary power subsystem consist of two buck/boost (B/B) regulators. The main B/B regulator is designed to provide regulated power for all spacecraft loads other than the radio transmitter and perhaps heaters. An identical standby B/B regulator serves as a backup to the main B/B regulator and will supply the same spacecraft loads. Switchover will be controlled by on-board detection (failure sensing-circuit shown in Fig. 42) of the voltage at the output of the main B/B regulator. The failure sensing circuit can also determine off-frequency conditions on the 2.4-kHz inverter. Once executed, the switchover is irrevocable during the mission.

The regulators accept power from the unregulated bus at voltages ranging from 25 Vdc, the lowest battery voltage, to 92 Vdc, the highest solar panel voltage. The output voltage is regulated at 56 Vdc $\pm 1\%$.

The B/B regulator provides the regulated dc output power by sensing the output voltage and adjusting the duty cycle (on-to-off time) of the inverter within the B/B

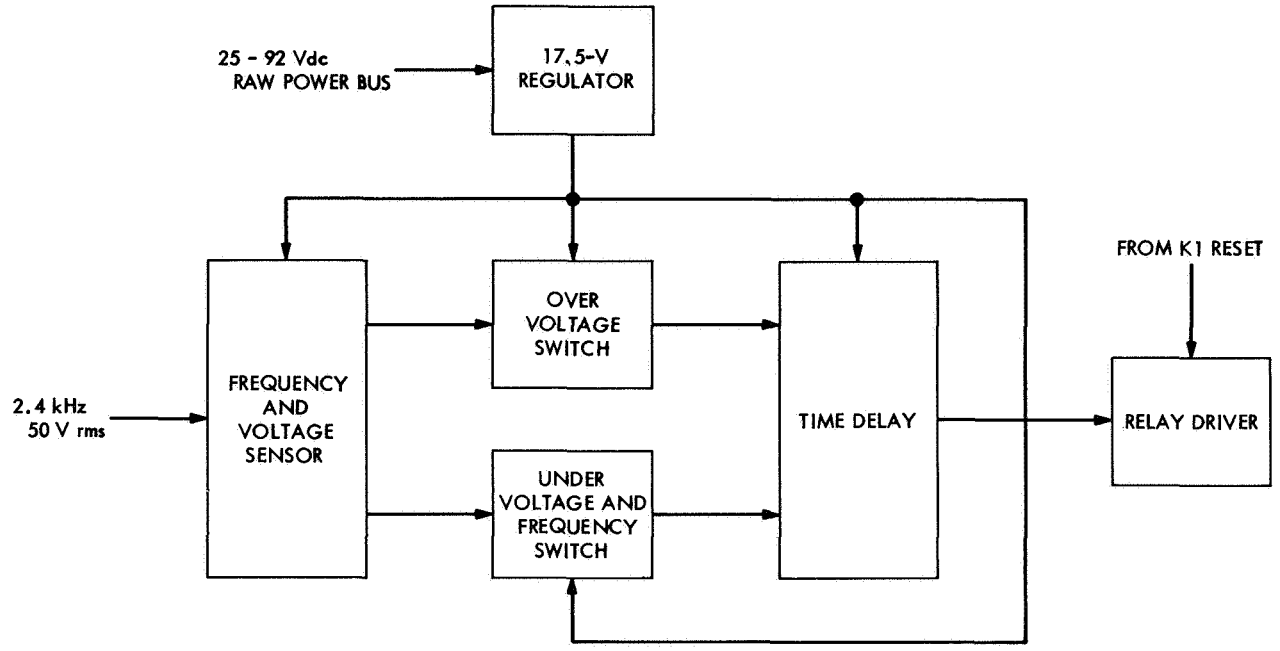

Fig. 42. Failure sensor circuit

regulator to maintain the desired output limit. Since the regulated output voltage is greater than the minimum value of input voltage, a step-up transformer is used for "boost." A flux oscillator is also used to provide a constant frequency to the inverter.

The regulating scheme must not only boost when the input voltage is lower than 56 Vdc, but attenuate (buck) the output for values greater than 56 Vdc. A switched regulation method vs a dissipative one has been selected, since it offers much greater efficiency and less thermal dissipation over its operating range. The expected efficiency is 80% or greater.

A generalized B/B regulator block diagram is shown in Fig. 43. Using a step-up transformer with a turns ratio (1:N) of 1:2.225 yields a regulated 56-Vdc output voltage for E_{in} = 25 V (duty factor τ = 100%) up to E_{in} = 92 V

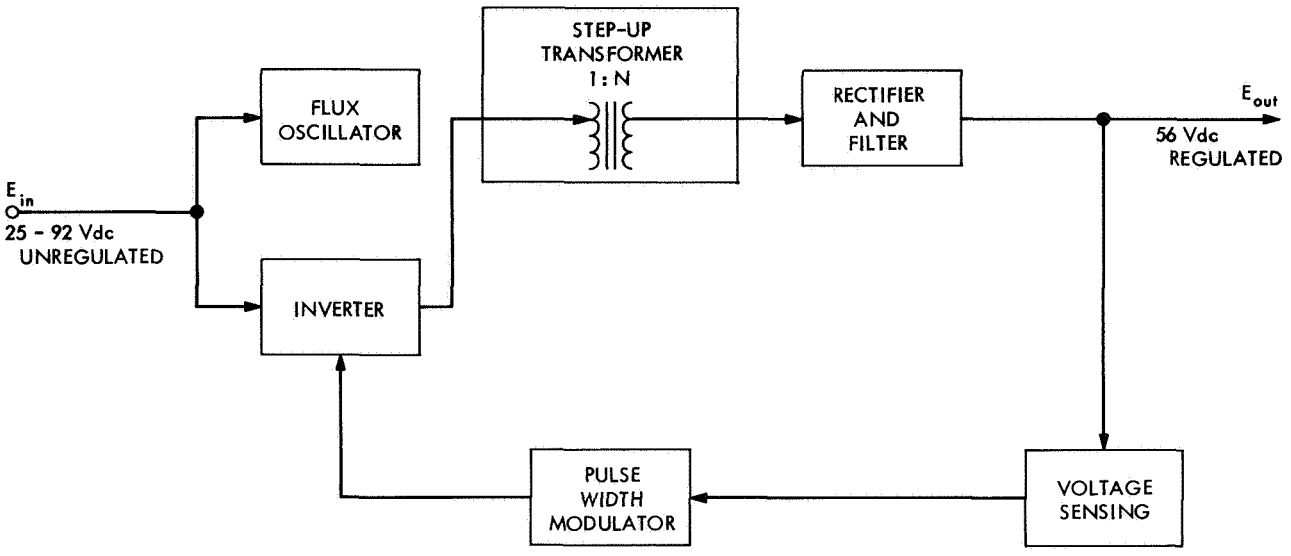

Fig. 43. Generalized block diagram of buck/boost regulator

(duty factor $\tau = 27.5\%$). The formula for calculating the duty factor is as follows:

$$\tau(\%) = \frac{E_{out}}{N \cdot E_{in}}$$

The flux oscillator is a two-core voltage feedback type with a fixed frequency driving an inverter, the bases of both are controlled by the pulse-width modulator (sensing the output).

5. 2.4-kHz inverters. The main power for spacecraft loads is a 56-V (rms) 2400-Hz square-wave supply generated from a dc-to-ac inverter (Fig. 44). Users take this ac power and, by using transformer-rectifier circuits, obtain the required dc voltage for their equipment. This method of distributing power provides for a greater design flexibility, since users can change voltage requirements late in the program without affecting the power system or requiring changes in the spacecraft cabling. In addition, it eliminates the movement of high voltages around the spacecraft in cables.

Under normal conditions, the main inverter will convert regulated 56 Vdc from the main B/B regulator to 56 V rms at 2.4 kHz with a conversion efficiency of 92%. This power will be distributed to engineering and science loads. In the event of a failure to the main power chain (i.e., main B/B regulator plus main inverter), the 2.4-kHz standby inverter will automatically switch into operation as part of the standby power chain (i.e., standby B/B regulator plus standby inverter).

6. Inverter frequency synchronization. A precision crystal oscillator circuit provides a synchronizing or a frequency-stable driving voltage for all power subsystem inverters. Accuracy of this frequency is ±0.01 percent, and is determined by a 307.2-kHz crystal clock, counted down to provide both 2400-Hz single-phase and 400-Hz single-phase signals and three-phase signals. A precision crystal clock is located in both main and standby inverters. The main inverter will free run at 2800 kHz ±5%.

7. Single-phase and three-phase 400-Hz inverters. Figure 45 shows a functional block diagram of the single-phase and three-phase 400-Hz inverter module. The function of this module is to convert the regulated 56-Vdc B/B regulator output into single-phase and three-phase 400-Hz square-wave power outputs that are synchronous with the 2.4-kHz square wave. The inverters are actually power amplifiers driven from the 2.4-kHz power synchronizer with an accuracy of 0.01%. The term power amplifier implies that the inverters have no free-running capability.

8. Redundant frequency source. The main and standby inverters are designed to operate at 2.4 kHz ±0.01%. In the event of a failure, the system will switch to the standby inverter with identical output characteristics. The standby inverter will free run at 2.4 kHz ±5% in the event of its internal clock failure.

9. Failure sensor. Figure 42 shows a functional block diagram of the failure sensor. The failure sensor will detect out-of-tolerance voltage or frequency on the main

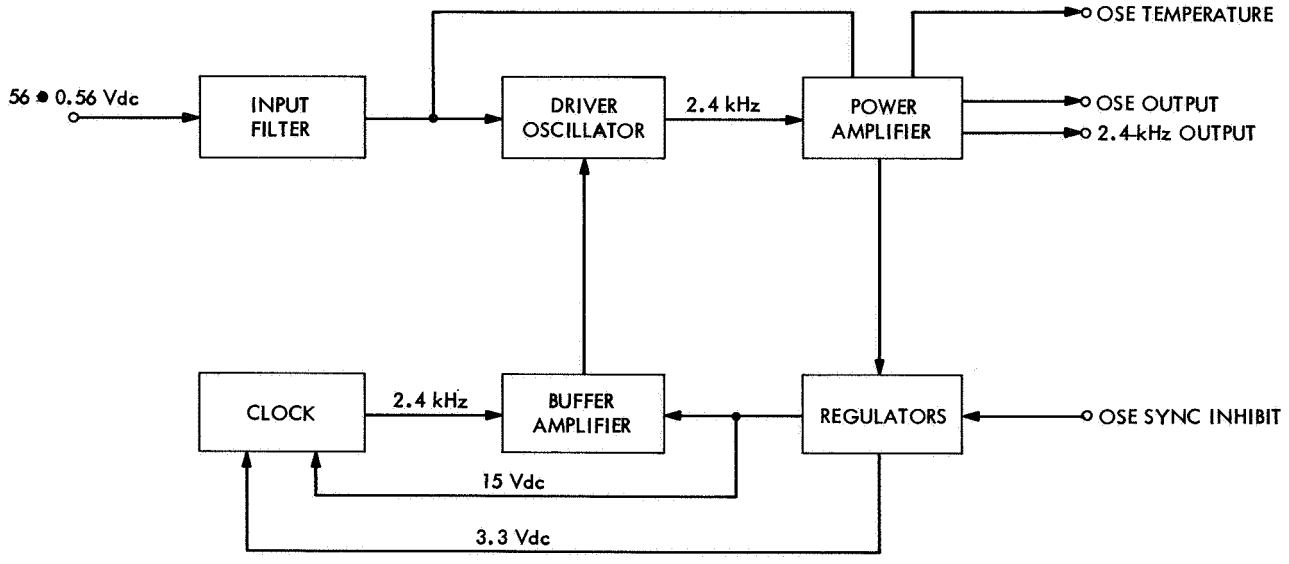

Fig. 44. 2.4-kHz inverter

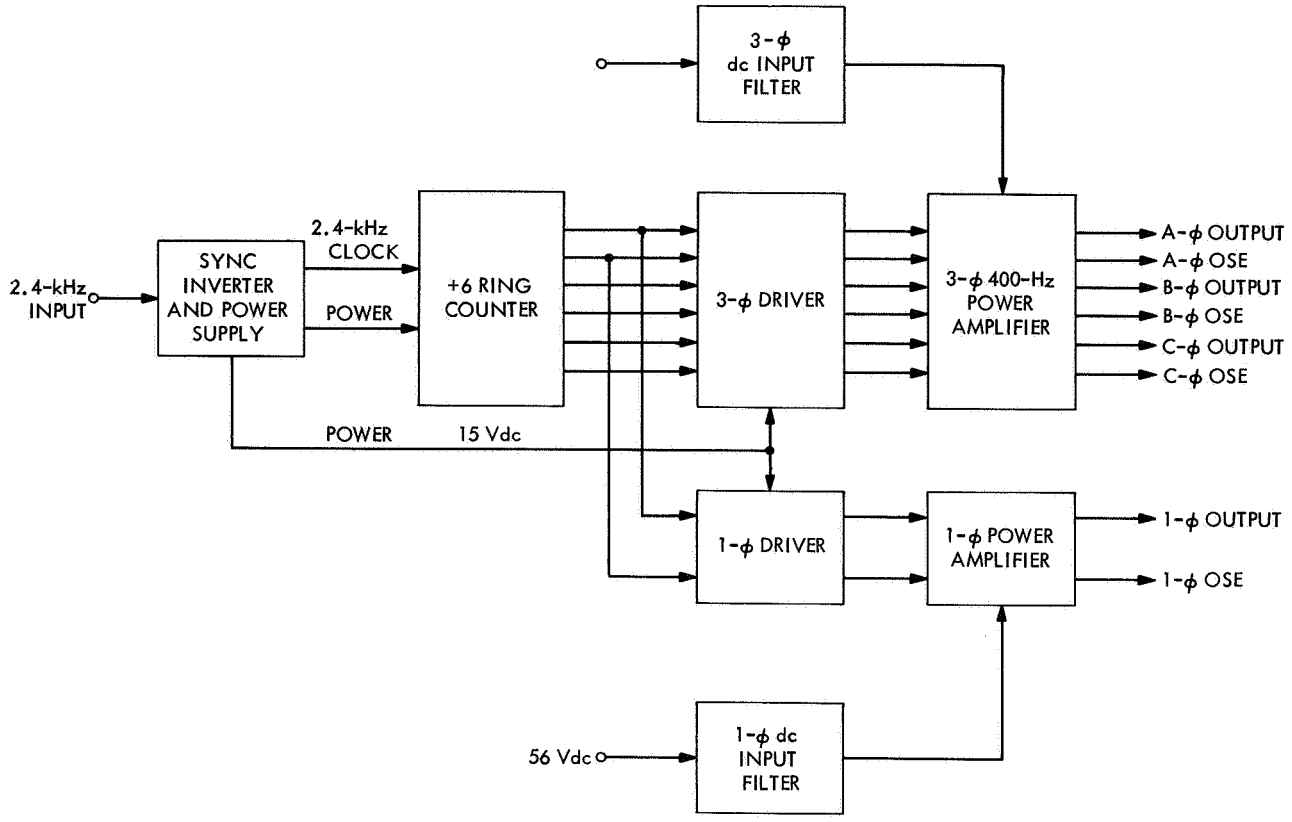

Fig. 45. Single-phase and three-phase 400-Hz inverters

power chain (main B/B regulator and main 2.4-kHz inverter). Should a failure be detected, the fail-sense circuit will activate a power control relay, and will switch operation to the standby power chain. The main power chain will be considered failed if the frequency and voltage are not within the limits of 2200–2600 Hz and 52.7–59.3 V, respectively.

10. Power distribution and switching module. The power distribution module is designed to provide the required switching and control functions for the effective management and distribution of power. This module accepts commands from other spacecraft subsystems and translates the commands into relay closures. The modules provide a central control of all power switching, as opposed to individual user switching.

To prevent random switching, considerable care must be taken in the design of the distribution electronics to make them insensitive to noise and transients. In addition, all inputs into the module from various spacecraft subsystems must be isolated to prevent interaction in a failure mode.

11. Transient response limitations. During turn-on or spacecraft system operation, the auxiliary power subsystem should not be subjected to transients that exceed 150% of the average power being switched, or 10 W for 10 ms, whichever is greater. In addition, current transients that occur each half-cycle of the 2.4-kHz waveforms and exceed 20% of the average input current, or that have time constants greater than 20 μs, will be undesirable.

12. Telemetry requirements. The number and type of telemetry channels required for the power subsystem are shown in Table 16.

C. Propulsion Power Conditioning Subsystem

The propulsion power conditioning subsystem is designed to be compatible with the spacecraft photovoltaic power system and to provide stable operation of the ion thrusters. Power condition designs very similar to those required for this study have been developed. Reference 10 goes into considerable detail regarding the design, characteristics, and operation of this component. Figure 46 is a block diagram of a thruster and power

Table 16. Power subsystem telemetry requirements

No. of measurements in category	Measurement category	Range	Resolution	Bit width	Sampling period			
					Launch, min	Emergency, min	Cruise, min	Encounter, min
4	Solar array output currents	0.90 A	3.0 A	5	1	1	60	4
2	Solar cell short circuit current	0–0.1 A	0.8 mA	7	↓	↓	↓	↓
1	Solar cell open circuit voltage	0–0.1 V	0.8 mV	7				
8	Panel temperature (2/panel)	−200 to +200°C	3° C	7		↓	↓	↓
24	Deployment Squibs (6/panel)	Binary	—	1		∞	∞	∞
4	Deployment verification indicators (limit switches)	Binary	—	1	↓	∞	∞	∞
4	Deployment motor voltage	0–60 V	1 V	6	0.5	∞	∞	∞
4	Deployment motor current	0–500 mA	4 mA	7	↓	∞	∞	∞
2	Deployment cable rate	0–1 ft/min	6%	4		∞	∞	∞
2	Deployment cable lengths	0–10 ft	2 in.	6	↓	∞	∞	∞
2	Battery voltage	18–33 V	0.5 V	5	1	1	1	4
1	Battery discharge current	0–10 A	0.08 A	7	↓	↓	↓	↓
2	Battery temperature	5–130°C	4°C	5				
1	Aux P/C input current	0–15 A	0.8 A	9				
1	2.4-kHz inverter temperature	5–130°C	4°C	5				
1	Battery charge current	0–5 A	80 mA	6				↓
5	IEPC[a] input current	80 A	1 A	7				∞
5	IEPC logic switch (4 PDS/switch)	4 states	—	2				∞
5	IEPC temperature	5–130°C	4°C	5				∞
1	2.4-kHz inverter output current	0–3 A	200 mA	4				4
1	400-Hz inverter input current	0–1 A	70 mA	4				4
1	Engine control voltage (set point)	0–5 V	0.4%	8				∞
1	Peak power point tracker enable	Binary	—	1				∞
1	Ion engine beam power	0–15 kW	0.8%	7				∞
1	Programmed thruster beam power	Digital	0.2%	9				∞
1	Max power point tracker logic input current	0–300 A	0.8%	7				∞
1	Max power point tracker logic input power	0–15 kW	0.8%	7				4
1	Combined solar panel output current	0–360 A	0.8%	7				↓
1	RF subsystem input current	0–3 A	0.3 A	7				
1	Power source logic voltage	25–100 V	2.2 V	7				
1	Main 2.4-kHz inverter voltage	40–60 V	1 V	7	↓	↓	↓	↓

[a]IEPC = ion engine power conditioner.

Table 17. Thruster power conditioning output nomenclature

Supply	Rated output			Nominal operating power for maximum output, W	Regulation		Controlled by
	Nominal voltage, V	Current, A	Power, W		Load, %	Line, %	
V_1 Electromagnet	10.3dc	1.3	14	30	—	5	—
V_2 Vaporizer	7 ac	2.0	14	6	—	—	I_{screen} (I_S)
V_3 Thruster cathode	5 ac	40.0	200	160	—	5	I_{arc} (I_A)
V_4 Arc	35 dc	12.0	420	300	1.5	—	—
V_5 Screen	2000 dc	1.05	2100	2000	5	—	—
V_6 Accelerator	2000 dc	0.1	200	20	10	—	—
V_7 Neutralizer cathode and vaporizer	12 ac	3.4	41	33	—	5	V_{keeper}
V_8 Neutralizer keeper	30 dc	0.1	3	2	100	5	—
Total power			2992	2511			

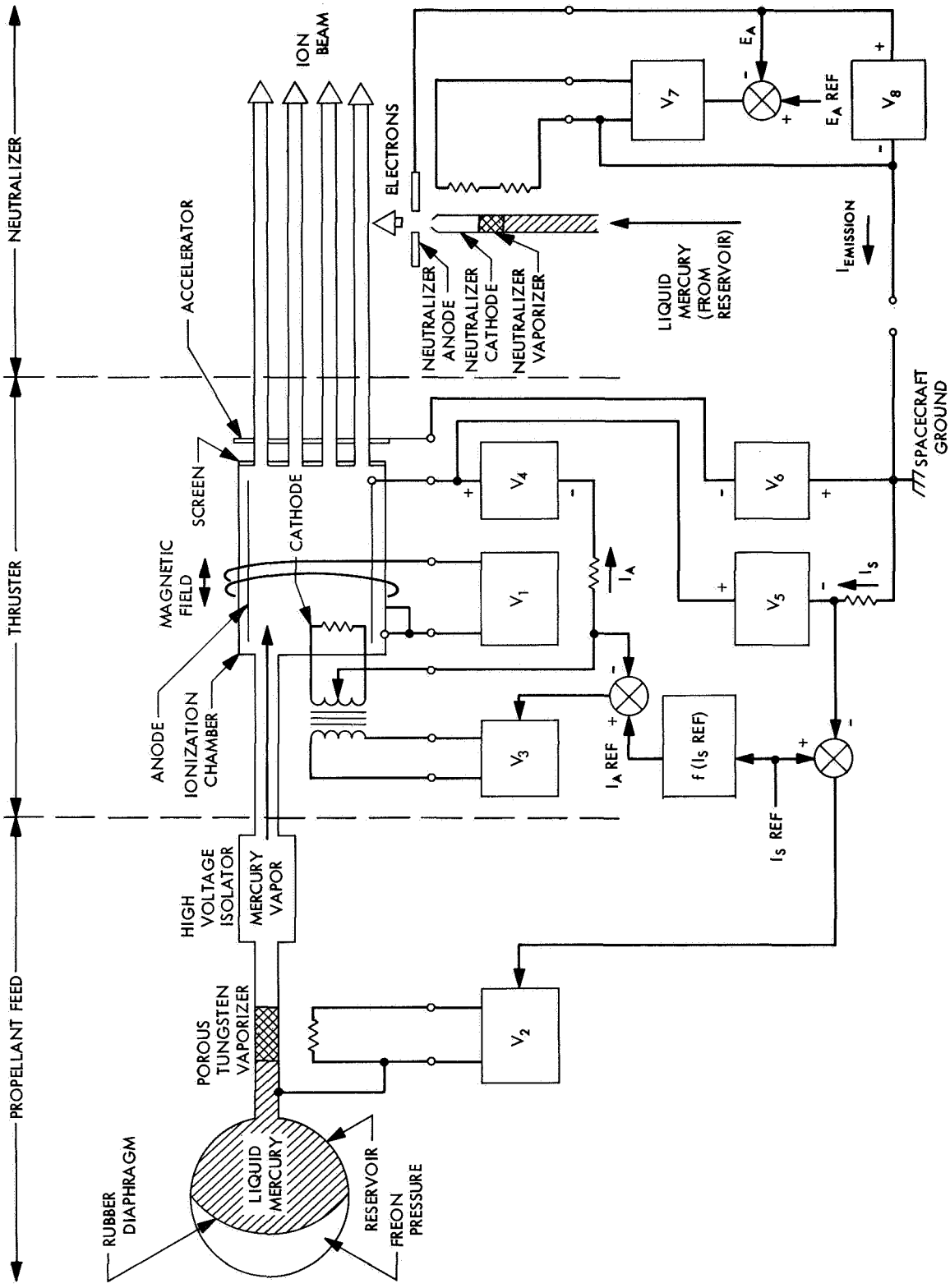

Fig. 46. Propulsion power conditioning and thruster block diagram

conditioner set. Also shown on the block diagram are the beam current set point (I_S) and the functionally related cathode emission set point (I_A). It is through these control loops that the CC&S matches the thruster power demand to the power program. Table 17 identifies the symbols used on the diagram and lists the outputs of the eight power supplies necessary to operate the thruster.

The power conditioning will be designed to be capable of 10,000 h of continuous space operation with a calculated reliability of 0.96. The equipment will have a total weight of 100 lb (25 lb per unit). The minimum electrical efficiency will be 93%.

The thruster power conditioners cover the surfaces of the spacecraft bus normal to the solar panel support mast. This location keeps all four conditioners in a relatively similar thermal environment. Each of the four units would be designed to radiate electrical losses from the 6.25-ft^2 surface normal to the mast centerline. The power conditioners will be 3-in. thick.

D. Engine Control Set-Point Determination and Load-Matching Subsystem

1. Programmed power profile. The problem of supplying electric power to an ion engine propulsion system when the maximum solar panel power available (at any time T) varies as a function of time is illustrated in Fig. 47. If the planned ion engine power consumption is at all times less than the maximum available solar panel power, then the engine power consumption profile may be programmed into the CC&S onboard the spacecraft, and a control system devised to operate the engine along this planned profile.

Such a system has been devised and is described below. The rationale for selecting a mode of operation which controls the power consumption of the engines at a predetermined rate is given in Section II-C-2. Figure 48 shows an ion engine running in a closed-loop condition.

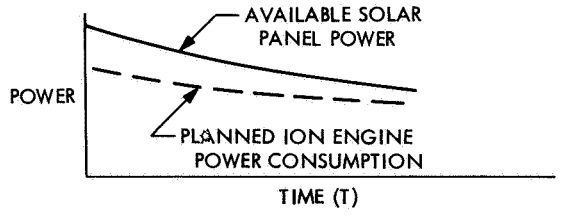

Fig. 47. Power profile

Control is effected via information feedback of the engine main beam power input to a differential network where this information is compared with the programmed power information stored in the CC&S subsystem. The programmed power information is stored in the CC&S subsystem in digital form and is converted to analog form using a 10-bit digital-to-analog (D/A) converter utilizing integrated circuitry. The programmed input from CC&S is then compared with the information feedback from the main beam power input for the engine, and the resultant difference (error signal ϵ) is fed through an integrating circuit as an input voltage signal (0–5 V) to the engine control unit. This latter unit adjusts the operating parameters of the ion engine in a manner proportional to the magnitude of the input signal (set-point).

The planned ion engine power consumption profile was chosen to be 18% below the estimated available solar panel power to allow for such contingencies as solar flare cell degradation and environmental uncertainties. Section III-A-1-a gives the rationale for the selection of this margin.

If the available solar panel power (with respect to time T) does not remain above the planned power consumption profile (i.e., because of excess environmental uncertainties, solar flare cell degradation, or panel misorientation), then the power profile may behave as shown in Fig. 49. At $T = t_1$, the engine is consuming power from the solar panel at the maximum power point. For $T > t_1$, the engine will drive the solar panel to a direct short-circuit condition (neglecting current limiting schemes).

2. Maximum power point tracker. The management control of power to the ion thrusters to minimize navigational problems, and also to eliminate the undesirable short-circuit condition (described above) is to utilize a solar panel maximum power point tracker system.

Of the several available maximum power point tracker schemes, the digital method is the most satisfactory, because of unlimited storage-time capability, immunity to noise, light weight, very low power consumption, and a high degree of reliability due to utilization of integrated circuitry.

The digital tracker monitors the solar panel output, determines at which side of the maximum power point the system is operating, and controls the engine load accordingly. If the programmed power profile exceeds the panel capability, then the system will drive itself to

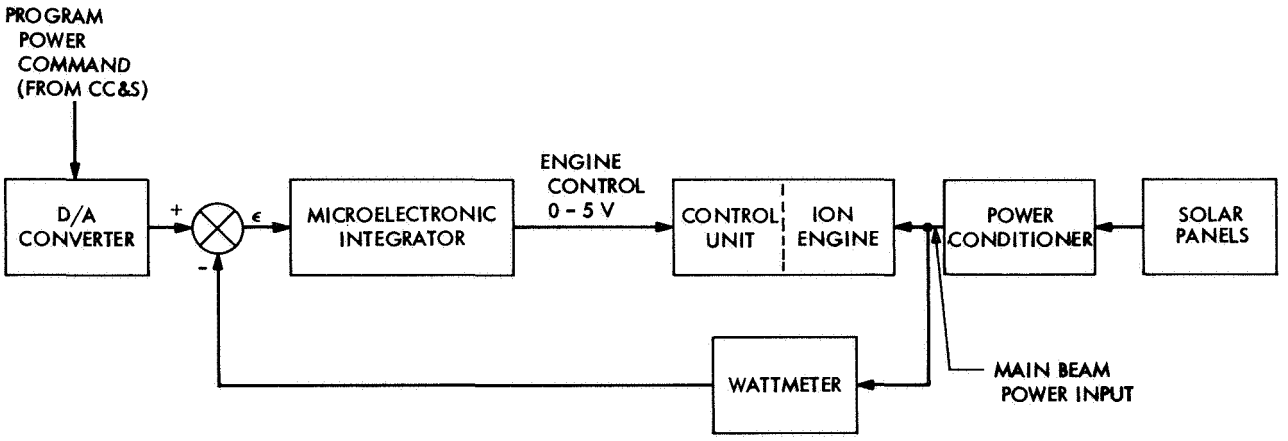

Fig. 48. Suggested ion engine control system

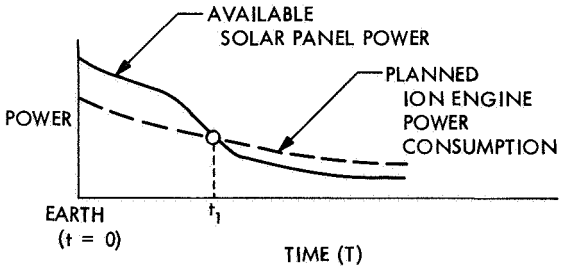

Fig. 49. Alternate power profile

operate on the short-circuit side of the maximum power point. When this event occurs, the tracker will decrease the power demand of the engine until the operating point reverts to the open-circuit side of the maximum power point. At this time, control is returned to the programmed power profile, and if its demand exceeds the supply, the system again returns to the short-circuit side of the maximum power point. The tracker, sensing this condition, again reduces engine demand. These oscillations in the engine demands effect a crude approximation of actually operating at the maximum power point at all times. Meanwhile, the CC&S subsystem can be reprogrammed with a revised engine power profile that is calculated to be always less than the maximum available solar panel power.

The engine is assumed to have a time constant of about 3 s. The microelectronic integrator provides a slow-rate-of-change low-level ramp voltage supplying 0–5 V to the engine input for controlling its output. If the relay shown in Fig. 50 should be in position 2, then the voltage previously applied to the engine control input will exponentially decay to 0 V via the microelectronic integrator and resistive feedback K_D. This action, in effect, will decrease the power demand of the engine.

Before discussing the operational mechanism of the digital ion engine control let us first review the solar panel profiles of power vs current, and current vs voltage for both the normal condition and excess power demand mode.

As shown in Fig. 51, the normal engine power demand is below the maximum solar panel maximum power capability; while in the mode shown by Fig. 52, the demand exceeds the capability. Since the engine is already operating under a fixed programmed load in a closed-loop configuration, any deviation from this value will result in an error correction signal being fed back to the engine input. If the engine load demand should become greater than that which the solar panel can supply (i.e., the engine operating point moves to the right and passes the maximum power point as in Fig. 52), the error signal will increase, and the engine load will drive the solar panel to near-direct short-circuit condition. To relieve this condition, the relay in Fig. 50 must transfer its contacts to position 2 (i.e., reduce the engine load).

The flow diagram in Fig. 50 shows the control functions of the digital ion engine and solar panel maximum power point trackers. The analog outputs from a wattmeter and ammeter (used to monitor power and line current, respectively, from the solar panels) are converted to digital outputs using analog-to-digital (A/D) converters. Digital shift registers, employed as storage devices, are commanded at certain specified times (by CC&S) to receive and store updated digital information.

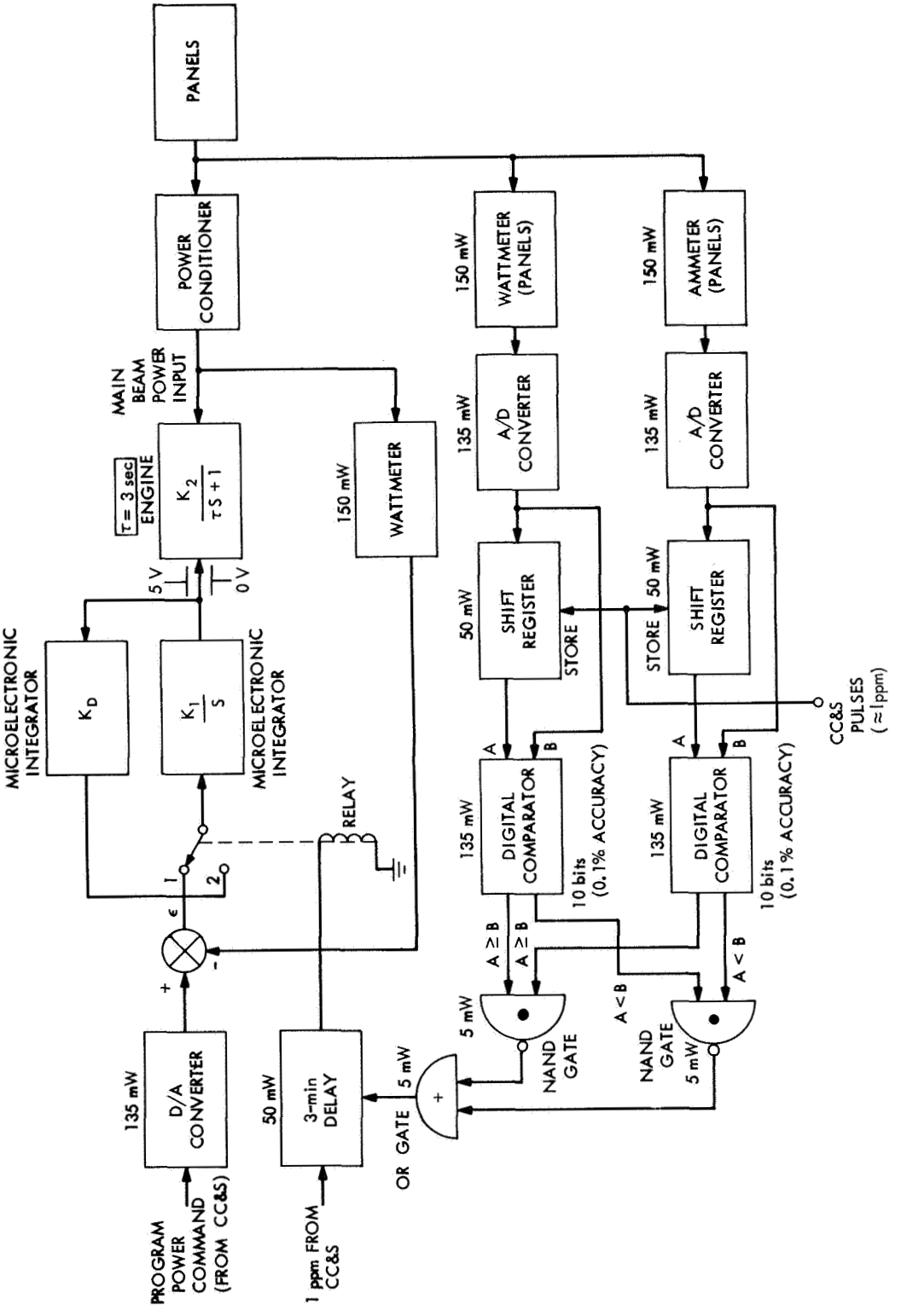

Fig. 50. Ion engine control system

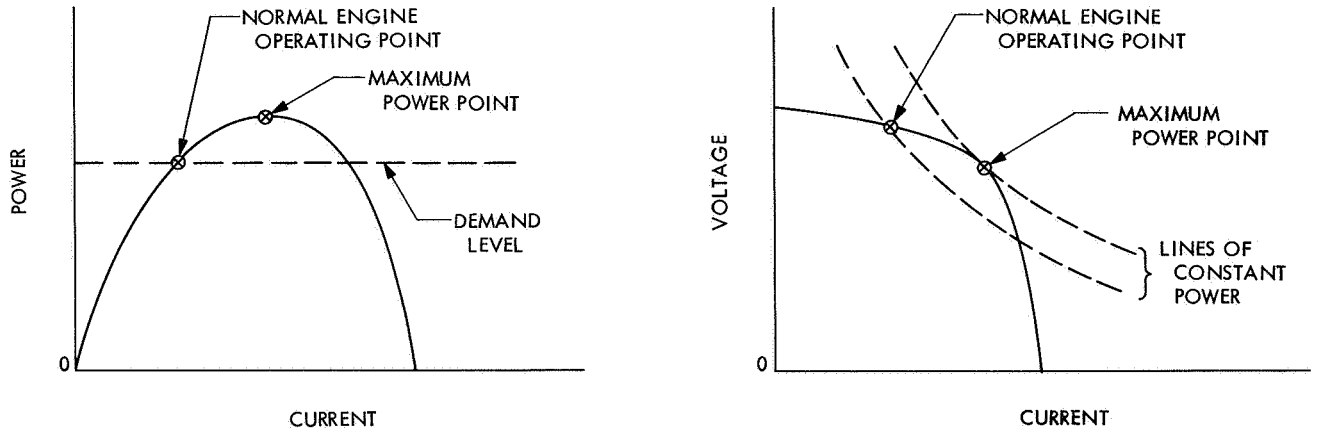

Fig. 51. Normal engine operating mode

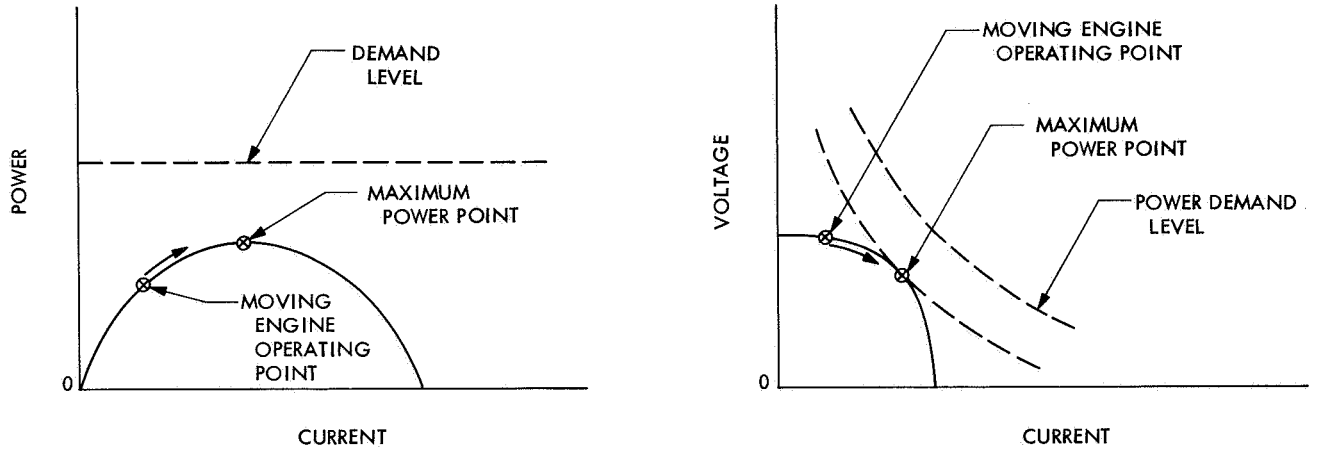

Fig. 52. Excess power demand mode

The minimum interval between pulses will be determined by the time response of the system and has not yet been fully evaluated. It may additionally vary with time.

The stored outputs of the digital shift registers are routed to digital comparators where they are compared with the outputs of their respective A/D converters. The outputs of the digital comparators produce output signals for: "*A* greater-than or equal to *B*" and "*A* less than *B*." Via logical schemes, these signals are routed to a pair of NAND gates and one OR gate. For a signal to exist at the OR gate output (signifying the fact that the normal engine operating power point does exist on the short-circuit side of the solar panel maximum power point), the following conditions (Fig. 51) must be met (as defined in Table 18):

(1) Increasing power = + slope.

(2) Decreasing power = − slope.

(3) Increasing current = + slope.

(4) Decreasing current = − slope.

Table 18. Solar panel properties[a]

Panel power	Panel current	Existence of output at OR gate	Relay constant position
+ slope	+ slope	No	1
− slope	− slope	No	1
+ slope	− slope	Yes	2
− slope	+ slope	Yes	2

[a]Refer to Fig. 50.

For an unstable combination of both panel power and current to exist, the condition of instability must exist for a prescribed period of time determined by the time response of the system for which the OR gate output signal is routed to a time-delay circuit (also programmed by CC&S). Otherwise, it will be considered as a temporary condition (due to noise) and no output command for relay transfer to position 2 will appear.

The majority of the devices thus described (Fig. 50) consist of integrated microcircuitry. The wattmeters, made up of integrated circuitry, are simple multipliers consisting of a current source, multiplier (differential amplifier), and amplifier. The voltage output of the wattmeter is the product of the two inputs and is linear. The A/D converters are monolithic MTOS integrated circuits containing 350 active components. They perform all the logic and analog switching functions for a 10-bit (0.1% accuracy) successive approximation analog-to-digital conversion. The shift registers also consist of integrated circuitry and are readily available. The digital comparators are constructed of basic building blocks comprising an exclusive-OR, a flip-flop, and a gate with enable-disable capability. The NAND and OR gates are integrated circuitry. The delay circuit is integrated microcircuitry comprising a clock, counter, and related decoding logic. The D/A converter is identical to the above described A/D converter except that a few simple wiring modifications are needed.

The weight and power consumption of the overall control system, including set-point determination and load matching, is extremely small. The entire unit will weigh less than 2 lb and consume about 1 W of electrical power.

IV. Conclusions

The coupling of a large-array solar panel with an electric propulsion system presents many unique design considerations heretofore not encountered.

Of major importance is the development of a solar array of lightweight construction. To achieve positive payloads for a Jupiter mission employing the *Atlas/Centaur* launch vehicle, a solar panel specific power in excess of 20 W/lb is a requirement. Development presently being undertaken by the Boeing Corporation under a JPL contract is aimed at achieving this goal. The use of thin silicon solar cells ($\cong$ 0.008-in. thick) and advanced, lightweight, substrate construction (beryllium frames and fiberglass backing) are the significant features of the design. Paramount in the implementation of a large-array solar panel are those problems associated with the stowage and deployment of the array. Preliminary techniques for accomplishing this array stowage and deployment have been devised and are presented within the text.

Throughout the duration of the Jupiter mission, the large-array panels will be subjected to the degrading effects of particulate radiation emanating from the sun and hypervelocity particles residing within interplanetary space. During encounter with the planet Jupiter, the power system will be further subjected to the irradiation effects of energetic electrons trapped in the magnetic field that surrounds the planet.

Estimates of the magnitude of the various effects have been made. The analysis conducted reveals a power reduction of less than 18% in the portion of the flight during which the electric propulsion system operates. At encounter, a worst-case model predicts nearly a 50% decrease in the power producing capabilities of the panels. Despite these losses, the mission can still be accomplished. However, since mission success depends upon accurate estimates of solar panel power degradation, experiments are required to substantiate the damage models, which have been assumed in the course of the various analyses. In particular, the irradiation of solar cells from the back side by both protons and hypervelocity particles is suggested because of the complete lack of data in the literature regarding this mode of damage.

Another major design consideration is the significant decrease in incident-solar light intensity during the course of the mission as a result of moving away from the sun, thus reducing the panel electrical power. The coupling of a variable output power source with an electric propulsion system necessitates a technique whereby the demands of the engine are controlled so that it corresponds to the available power. The approach that has been chosen is one in which the demands of the engines are varied in accordance with a stored engine power consumption profile. The programmed profile, which is stored in the on-board computer, is chosen to be 18% below the estimated available solar panel power profile to allow for such contingencies as radiation and particle damage and other environmental uncertainties.

In addition, a peak power point tracker has been added to the system to allow the engine demands to follow the maximum power point of the solar panels, should the

available power become less than the programmed power profile. Telemetry information will then allow an estimate of a new projected power profile for which another engine power consumption profile can be determined and programmed into the spacecraft computer. The development of prototype hardware to demonstrate proof of principle is desirable.

Associated with the decrease in solar panel power as the spacecraft moves away from the sun is an increase in panel output voltage, which results from lower temperatures. The resultant voltage variation affects the design of the power conditioning equipment. For instance, the thruster power conditioners must be designed to handle input voltages ranging from 40 to 73 V. Moreover, the power conditioning for the spacecraft loads must handle voltages between 25 and 92 V. The larger range is a result of the requirements for battery operation as well as the longer operational periods. The design of power conditioning systems that have low weight, high efficiency, and can handle the large input voltage variations has been accomplished on paper. The development of proof-of-principle prototype devices is an obvious requirement.

The final design consideration is for a method of supplying electrical power to the spacecraft loads during periods of solar power loss. Of particular concern is the solar occultation, which occurs for about 1 h during Jupiter encounter. The design of an energy storage system that is capable of operation after 900 days of flight time has been described within the text. In essence, it consists of a silver-zinc battery system that is maintained at very low temperatures ($\sim 0°F$) throughout most of the flight time and then activated (heated up to 70°F) shortly before encounter to assure a "fresh" battery supply. The low temperatures are essential to retard electrolyte reaction with the battery plates and separators, the normal cause of battery failure. A large-scale battery experimental program is presently under way at JPL to determine the effects of long-term storage on AgZn batteries under varying conditions. The results of this program will determine the practicability of this low-temperature storage technique.

References

1. Strack, W. C., and Zola, C. L., *Solar Electric Propulsion Probes for Exploring the Solar System,* TMX-52318. Lewis Research Center, Cleveland, Ohio, 1967.
2. Sandstrom, J. D., *A Method for Predicting Solar Cell Current-Voltage Curve Characteristics as a Function of Incident Solar Intensity and Cell Temperature,* Technical Report 32-1142. Jet Propulsion Laboratory, Pasadena, Calif., July 15, 1967.
3. Rosenzweig, W., "Radiation Damage Studies," paper presented at IEEE Photovoltaic Specialist Meeting, Washington, D.C., Apr. 10–11, 1963.
4. Martin, J. H., et al., "Radiation Damage to Thin Silicon Solar Cells," in *Advances in Energy Conversion Engineering,* proceedings of the 1967 Intersociety Energy Conversion Engineering Conference, held in Miami Beach, Fla., Aug. 13–17, 1967.
5. Linnenbom, V., *Range Energy Curves for Protons and Electrons in Quartz,* NRL Report 5828. Naval Research Laboratory, Washington, D.C., Sept. 1962.
6. Volkoff, J., *Protection Requirements for the Resistance of Meteoroid Penetration Damage of Interplanetary Spacecraft Systems,* Technical Report 32-140. Jet Propulsion Laboratory, Pasadena, Calif., July 1, 1964.

References (contd)

7. Cosby, W. A., and Lyle, R. J., *The Meteoroid Environment and its Effects on Materials and Equipment,* NASA SP-78. National Aeronautics and Space Administration, Washington, D.C., 1965.

8. Bjork, R. L., Kreyenhagen, K. N., and Wagner, M. H., *Analytical Study of the Impact Effects as Applied to the Meteoroid Hazard,* NASA CR-757. National Aeronautics and Space Administration, Washington, D.C., May 1967.

9. Vette, J. I., Lucero, A. B., and Wright, J. A., *Models of the Trapped Radiation Environment,* NASA SP-3024, Vols. II and III. National Aeronautics and Space Administration, Washington, D.C., 1966.

10. *Development and Test of an Ion Engine System Employing Modular Power Conditioning,* Final Report SSD 60374R. Hughes Aircraft Co., Culver City, Calif., Aug. 1966.